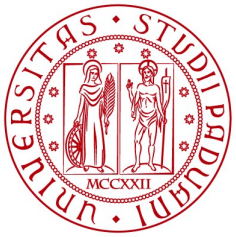

UNIVERSITÀ
DEGLI STUDI
DI PADOVA

Sede amministrativa: Università degli Studi di Padova

Dipartimento di *Ingegneria Industriale*

SCUOLA DI DOTTORATO DI RICERCA: Ingegneria Industriale

INDIRIZZO: Ingegneria dell'Energia

CICLO XXVII

Designing, Manufacturing and Test of a Nonimaging Optics particularly for Concentrated Photovoltaics. TwinFocus: a case study.

Direttore della Scuola: Ch.mo Prof. Paolo Colombo

Coordinatore d'indirizzo: Ch.mo Prof. Luisa Rossetto

Supervisore: Ch.mo Prof. Luisa Rossetto

Dottorando: Alessandro Saccà

The value of an idea lies in the using of it
[*Thomas A. Edison*]

Contents

List of acronyms

3J Triple-junction (solar cell) p. iv

ARC Anti-Reflection Coating p. 18

CAD Computer Aided Design p. 27

CAP Concentration-Acceptance Product (factor) p. 14

CMM Coordinate Measuring Machine p. 40

CNC Computer Numerical Control p. 3

CPV Concentrated Photovoltaics p. vii

CSOC Concentrator Standard Operating Conditions p. 64

CSTC Concentrator Standard Test Conditions p. 63

DLS Damped Least Squares p. 12

DNI Direct Normal Irradiance p. 72

DOE Design of Experiment p. 42

EQE External Quantum Efficiency p. 9

EROEI Energy Returned On Energy Invested p. 1

FF Fill Factor p. 36

I_{sc} Short-circuit current p. 31

LED Light Emitting Diode p. 3

MF Merit Function p. 12

MOCVD Metalorganic Chemical Vapor Deposition p. 9

NURBS Non-Uniform Rotational B-Spline p. 12

PC Polycarbonate p. 20

PMMA Polymethyl methacrylate p. 14

POE Primary Optical Element p. iii

PV Photovoltaics p. vii

PVD Physical Vapor Deposition p. 19

SMS Simultaneous Multiple Surface (design method) p. 17

SOE Secondary Optical Element p. iii

SSL Solid State Lighting p. 3

STF Spectral Transfer Function p. iv

TIR Total Internal Reflection p. 30

V_{oc} Open-circuit voltage p. 64

Abstract

The idea behind concentrating photovoltaics (CPV) is straightforward: concentrate the sunlight onto a small solar cell in order to shift largest part of the system cost from the semiconductor to the balance of system components. CPV systems designed for high concentration factors use solar cells with the highest achieved efficiency, which are the triple-junction (3J) ones. The rapid growth of flat panels PV market during last years attracted the world attention to photovoltaic technologies, particularly for the achievement of the *grid-parity* goal. In the meanwhile CPV technology attracted researchers and investors particularly for the introduction in the PV market of high efficiency triple-junction solar cells designed for terrestrial applications. An accurate design of CPV system, pushed by a growth of the CPV market, can make CPV technology competitive in the near future. This PhD work is integrated into this research and market scenarios.

The main goal of this work is to design a nonimaging optics for CPV technology. Starting from a constraint analysis of the problem some initial choices are made. This first step is also the most important one, because it needs a deep knowledge of the technologies involved, from the mechanical tolerances to the production costs. At this level a key choice is the main optical element, which in this work is a polycarbonate substrate that is then aluminized. This choice was made basically to take advantage of injection molding technology know-how, particularly for automotive lighting application. After these initial choices a workflow is adopted for the subsequent design of the optical scheme, the tolerance analysis and the manufacturing process, analyzing carefully in particular the realization of the primary optical element. For this purpose a dedicated experiment was performed in order to optimize its injection molding process. The work concludes with an outdoor test of the first prototype manufactured and with a comparison of its performances with the electrical distributed model developed.

All the activity presented were supported by Polo Fotovoltaico Veneto and Centro Studi e Ricerche E.Fermi of Rome. The outdoor measurements on the experimental installations were performed within the Laboratori Nazionali di Legnaro (LNL-INFN), while the experiment designed around the injection mold was performed within the company Unica Srl in Conegliano Veneto, Treviso.

Riassunto

L'idea alla base del fotovoltaico a concentrazione (CPV) è molto semplice: concentrare la radiazione solare su piccole celle fotovoltaiche allo scopo di ridurre il costo del semiconduttore impiegato verso gli altri componenti costituenti il sistema fotovoltaico. I sistemi CPV progettati per alte concentrazioni utilizzano celle solari che attualmente risultano le più efficienti mai realizzate, le celle fotovoltaiche a tripla giunzione (3J). La rapida crescita del mercato del fotovoltaico (PV) piano avvenuta negli ultimi anni ha destato l'attenzione di tutto il mondo nei confronti di questa tecnologia, in particolar modo grazie al raggiungimento della *grid-parity*. Nel frattempo la tecnologia CPV ha richiamato ricercatori ed investitori, attirati in particolare dall'introduzione sul mercato delle celle solari a tripla giunzione per applicazioni terrestri. Una progettazione accurata del sistema CPV, aiutata da una crescita del mercato del CPV, potrà portare questa tecnologia ad essere competitiva in un breve futuro. Questo lavoro di dottorato si integra in questo scenario accademico ed industriale.

Lo scopo principale del lavoro è consistito nel progettare un'ottica non-imaging per la tecnologia CPV. A partire dall'analisi dei vincoli progettuali sono state affrontate alcune scelte iniziali. Questo primo step è il più importante durante l'intera fase progettuale perché richiede un'approfondita conoscenza dei processi produttivi coinvolti, a partire dalle tolleranze meccaniche fino ai costi di realizzazione. In questa fase della progettazione un punto importante è stato la scelta dell'elemento ottico primario, un substrato in policarbonato successivamente alluminato. Questa scelta è stata fatta per trarre vantaggio dal *know-how* della tecnologia degli stampi ad iniezione, particolarmente usati nel mondo dell'illuminazione automotive. Successivamente a questa fase di progettazione delle superfici ottiche, si è passati all'analisi delle tolleranze e alla realizzazione dei componenti, ponendo particolare attenzione alla realizzazione dell'elemento ottico primario. A questo proposito è stato allestito un esperimento volto ad ottimizzare la procedura di stampo ad iniezione di tale elemento ottico. Il lavoro si conclude con un test outdoor del primo prototipo realizzato e con il confronto delle prestazioni elettriche di una cella 3J simulata grazie ad un modello dedicato.

Tutte le attività presentate sono state svolte grazie al supporto del Polo Fotovoltaico Veneto e del Centro Studi e Ricerche E.Fermi di Roma. Le misure sulle installazioni sperimentali sono state svolte presso i Laboratori Nazionali di Legnaro (LNL-INFN) mentre l'esperimento realizzato attorno allo stampo ad iniezione è stato svolto presso la ditta Unica Srl di Conegliano Veneto.

Chapter 1

Introduction

This chapter outlines the motivations of this PhD work. It starts with an overview of the technologies involved in the project and highlights the key-concepts to design a CPV product. It then focuses on CPV, particularly on the state-of-the-art of solar cells and nonimaging optics.

The design of any energy generation technology starts with the study of the *Energy Returned On Energy Invested* (EROEI) function

$$EROEI = \frac{Energy\ returned}{Energy\ invested} \tag{1.1}$$

where the *Energy returned* term indicates the energy produced by that technology during its lifetime, and the *Energy invested* term indicates the energetic cost to produce, install, maintain and recycle it. This equation includes all the terms that an energetic engineer should know, but it's not easy to handle and to calculate the EROEI factor of a particular technology. Different studies [1] [2] indicate that exists a huge variability in the expected value of the EROEI factor concerning Photovoltaic (PV) technologies, depending on the adopted model. A factor that greatly influences the EROEI factor of a technology is its market volume, so the trend of its so-called learning curve. From this point of view, no energy technology has historically changed more dramatically than PV, whose cost has declined by a factor of nearly 100 since the 1950s [3]. The growth of the PV market, and especially the growth of the market segment that uses trackers, has been an important contributor to the increased interest in CPV products. Figure 1.1 shows a comparison between PV and CPV yearly volume installations: the ratio between them is currently three orders of magnitude.
Over the years many studies highlighted the potential of CPV technology [4] [5] [6], some of which even before the introduction of the III-V multijunction solar cells in terrestrial market [7] [8].

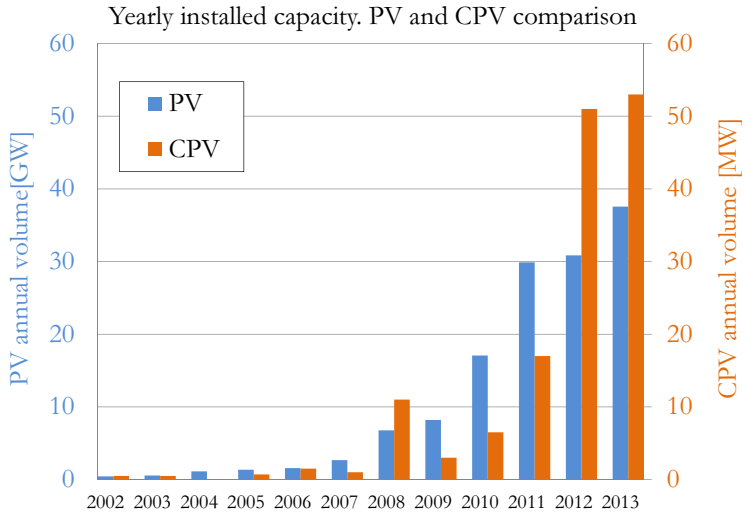

Figure 1.1: PV and CPV annual volume capacity. PV data ref. `www.bp.com`. CPV data ref. `www.ise.fraunhofer.de`.

During last years the biggest competitors in CPV market claimed new module efficiency world records higher than 35% using conventional triple-junction III-V solar cells [9] [10], and recently also using four-junction solar cells [11]. These results show the potential of this technology, but the real challenge for CPV is nowadays to find out a trade-off between the efficiency and the cost of the system, of course never forgetting the reliability aspect, in order to be competitive on the market of energy technologies.

1.1 Motivations

Various technological sectors can be helpful for CPV to realize a cost-effective and reliable module. Automotive lighting is in particular an interesting sector from which CPV can get many inputs. The basic idea behind this PhD dissertation is to realize a mirror-based off-axis nonimaging optics with low profile height for high concentration photovoltaics taking advantage of a mature and cost effective technology like injection molding for automotive lighting. Some mature technologies useful for CPV are reviewed.

1.1.1 Freeform optics

Freeform surfaces are defined as any non-rotationally symmetric surface or a symmetric surface that is rotated about any axis that is not its axis of symmetry. Historically the choice of surfaces available for the design of optical elements was limited to rotationally symmetric ones. In telescopes or

camera lenses spherical and conic surfaces are the common ones, but higher degrees of freedom in the surface shape can give many advantages. The main benefits are the reduction of wavefront aberrations and the reduction of the number of optical elements, so a higher compactness and a reduction of costs [12]. More details about freeform surfaces will be given in section 1.3. A mature technology largely used in automotive applications is the injection molding process for the production of plastic mirrors. Through the help of CNC machines optics designers can design optical surfaces completely freely so feeform designers get benefit from the constant improvement in CNC machines and their mechanical tolerances [13]. The achievement of functional specifications of a freeform optics largely depends on the experience of the optical designers and the CNC machine operators through a trial-and-error approach when new freeform optics design is used. More details about injection molding process will be given in chapter 3.

1.1.2 Computing speed

Ray tracing softwares are tools to simulate the light path of light rays taking into account their interaction with various media. Depending on the problem that an optical designer has to face, a ray tracing software can operate in sequential or in non-sequential mode. Lighting and concentrating applications require non-sequential approach, which means that the ray tracing software does not require the introduction of the optical elements (source, mirror, lens, target, ...) in a specific order. This is due to the fact that in non-sequential approach it is not defined *a priori* the order with which a ray emitted by a source will interact with the other objects. This approach requires the simulation of many rays in order to collect a large number of them on the target. According to figure 1.2 this is also the main difference between imaging and nonimaging optics: imaging links different source points to target points, while nonimaging links an incoming light flux to a target irradiance map, so in the latter case the simulated rays must fill the target. The incredible improvements in computing speed during last years, helped also by the commercialization of multi-thread processor, are extremely helpful in ray tracing simulations, particularly during optimization process. More details about computing speed and ray tracing simulation setup can be found in section 2.2.2 and in Appendix A.

1.1.3 Thermal management

In Solid State Lighting (SSL) applications thermal management is a critical aspect. Even though luminous efficacy[1] of a LED is about six times larger

[1]Luminous efficacy defines the light flux of a source respect to the invested electric power. Luminous efficacies of tungsten bulbs and LEDs are about 15 lm/W and 80 − 100 lm/W, respectively

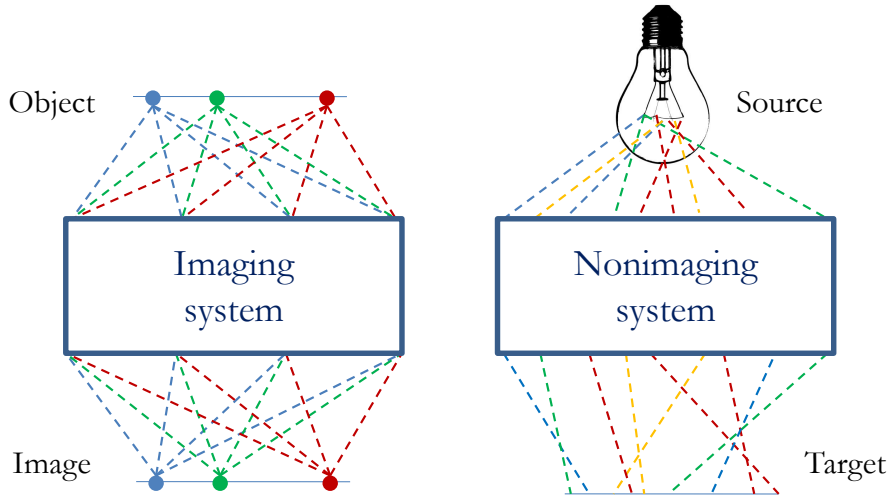

Figure 1.2: Comparison between an imaging and a nonimaging optical system: in the first case the goal is to fiund a geometrical correspondence between the source and the target while in the latter the goal is to efficiently transfer the radiation with a prescribed pattern.

than a tungsten bulb's efficacy, thermal management has a strong impact in the lifetime length and efficiency of a LED. For these reasons many efforts are invested in the study of efficient and cost effective heat management solutions. Thermal management knowledge in SSL applications can be easily transferred to CPV. In both cases the die (the solar cell or the LED) is supported by a substrate used to mechanically support and electrically connect the die. The substrate must have a high thermal conductivity and a high dielectric strength between the die and the cooling system. A common substrate is the Metal Core Printed Circuit Board (MCPCB), which has a heat spreading metal core. Common dielectric isolation layers are aluminum oxide (Al_2O_3) or the more expensive aluminum nitride (ALN). Once that the board and the die are connected, this package needs then to be mounted on an active or passive heat dissipating solution. The latter is often preferred because, compared to the first one, it has the advantages of simpler structure, easier fabrication and lower cost. Common passive solutions for microelectronic devices can be divided in two groups depending on the thermal load and cost. Heat sink is the cheaper solution and it is devoted to applications where the thermal load is not greater than 50W [14]. Higher thermal loads require the introduction of phase change recirculation, such as heat pipe. According to the lower cost compared to heat pipes, heat sinking is the mainstream approach for passively cooling [15].

1.1.4 Multijunction solar cells

The main reason for the increased interest in CPV field since last decade is the introduction of multijunction solar cells for terrestrial applications. Multijunction solar cells consist in photovoltaic (PV) devices composed by multiple p-n junctions. Each junction is made by several semiconductor materials and it is sensible to a specific electromagnetic wavelength range. Multiple junctions allow the PV system to collect a broader portion of the solar spectrum, so they are studied with the goal to create a more efficient PV device. Monolithic triple-junction (3J) solar cells represent the current state-of-the-art and are commercially available since years. More details on 3J solar cells are given in section 1.2.2.

1.2 CPV: history and state-of-the-art

The concentration of sunlight on photovoltaic devices has been explored since the beginning of PV industry [16] [17]. The idea behind concentrating sunlight is straightforward: increase cell efficiency and reduce the area and hence the cost of the solar cell. In this section a small introduction on CPV basic concepts is given, starting from a brief history of CPV technology.

1.2.1 Brief history of CPV

Research on Concentrated Photovoltaics began in the USA in 1975, boosted by federal funds after the oil crisis. The main players initially were Sandia National Laboratories and the US Department Of Energy (DOE, founded in 1977). Over time, many companies and universities tried to develop their own CPV systems. In that period the investments were mainly concentrated in areas with high direct solar irradiance such as Spain, Italy, Saudi Arabia, and US south-western regions. It was estimated that the total funds expended worldwide from 1975 through 1992 were probably over $40 millions [8], and some remarkable success resulted from these investments [18] [19]. First notable prototypes of CPV systems were realized in the late 1970s: Sandia National Laboratories realized a system using acrylic point-focus Fresnel lenses with active water cooling, while the Institute for Solar Energy of the Polytechnic University of Madrid (IES-UPM) developed the so-called Ramón Areces panel, a silicon-on-glass point-focus Fresnel lens with a passive cooling system (figure 1.3). Sandia's system was also adopted for the 350-kWp SOLERAS project, the world's first concentration plant. More info about past experiences in CPV research can be found in ref. [20]. All these mentioned CPV projects used silicon-based solar cells. A remarkable result obtained with this technology was the silicon point contact concentrator solar cell that achieved 27.5% with a concentration factor of 100× [21]. Huge boosts for the investments in CPV projects came from the introduc-

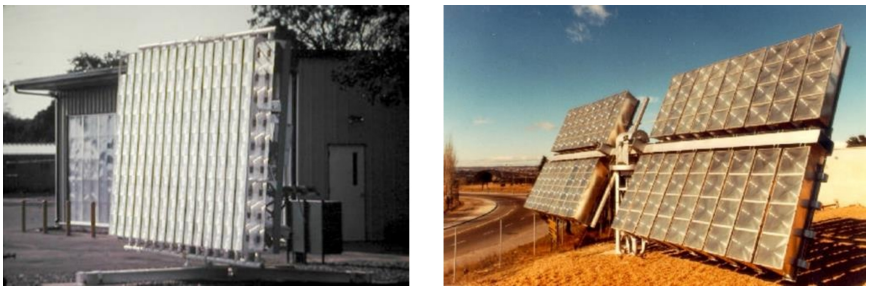

Figure 1.3: Left: the first Sandia array, made with 5-cm-diameter Si solar cells operating with acrylic Fresnel lenses at $32 suns$ and an active (water) cooling system. Right: the Ramón Areces panel, made with silicon-on-glass point-focus Fresnel lenses and a passive cooling system.

tion of multijunction (or tandem) solar cells such as dual-junction [22] [23] and triple-junction (3J) [24] [25] ones. The latter one represents the current state-of-the-art and 3J solar cells are nowadays implemented in almost any CPV system, but the market is progressively moving toward four- and five-junction solar cells [26] [27]. Figure 1.4 represents the timeline of the best research-cell efficiency.

1.2.2 Triple-junction solar cells

Stacking multiple p-n junctions is a way to convert into electricity a broader range of solar spectrum. According to Shockley-Queissier (SQ) [29] and subsequent studies, the efficiency of a multijunction solar cell depends on many factors: number of p-n junctions, reference spectrum, junction band gaps value, concentration factor, radiative and non-radiative losses. The theoretical maximum conversion efficiency for unconstrained solar cells (not series connected) and for various number of p-n junctions is shown in figure 1.5. Triple-junction is nowadays the mainstream technology due to the relatively low cost and the high achieved efficiency (in recent years commercial 3J solar cells reached 42% [30]). Over the years two technological approaches have been investigated in manufacturing 3J solar cells [31]: in mechanically stacked approach p-n junctions with different energy-gap are produced and then stacked together, while in monolithic approach the layers are grown on a substrate and the p-n junctions are connected in series with interband tunnel diodes. Although the current state-of-the-art technology for 3J solar cells is the monolithic approach, basically for their simpler cell processing and relatively lower cost, mechanically stacked solar cells can overcome some limits of monolithic approach such as current mismatching and lattice mismatching [32]. This section is devoted only to monolithic 3J solar cells due to the fact that these represent, in short terms, the only way to manufacture a cost effective CPV system. Monolithic 3J solar cells are grown through a

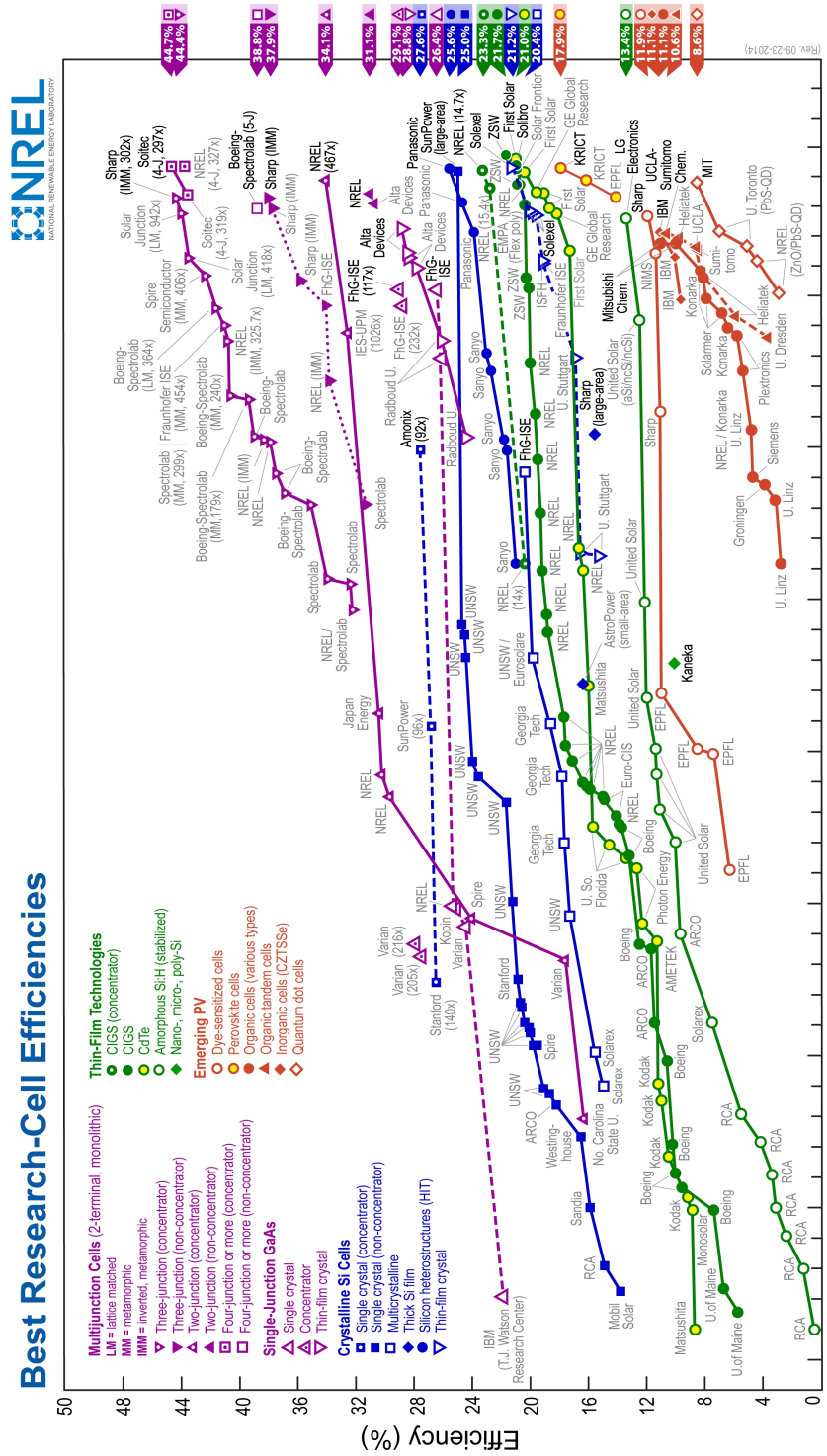

Figure 1.4: Best Research-Cell Efficiency timeline. Ref. `http://www.nrel.gov/ncpv/images/efficiency_chart.jpg`

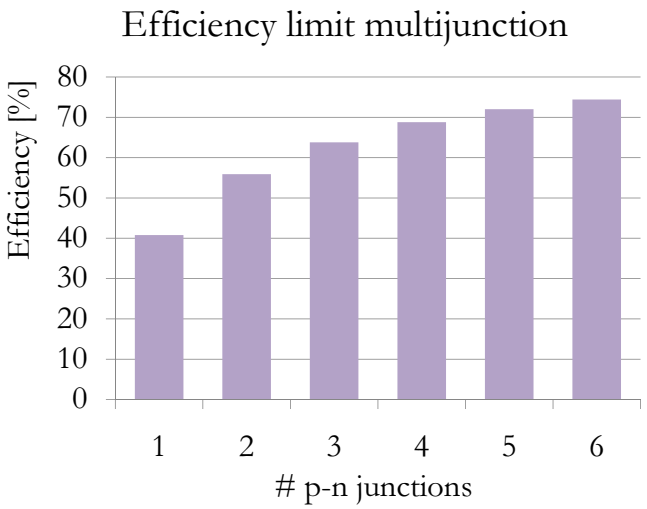

Figure 1.5: Detailed balance limit efficiency limits at full concentration for unconstrained solar cells (not series connected). Data taken from ref. [28]

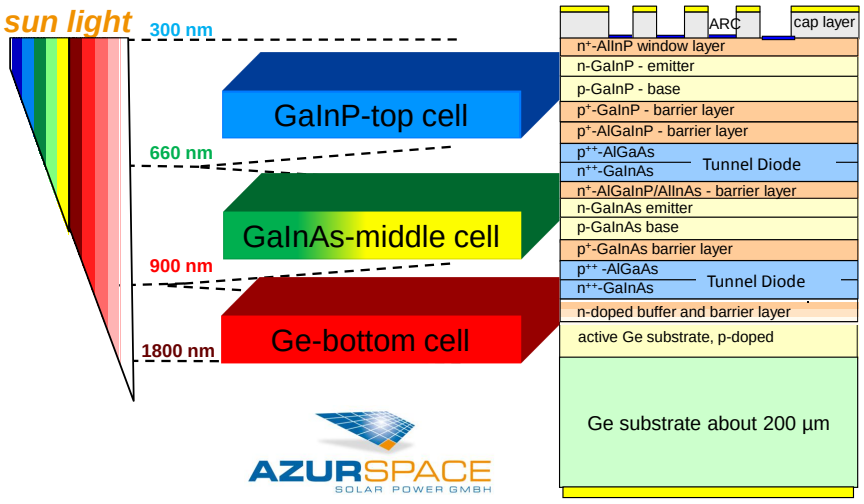

Figure 1.6: Monolithic 3J solar cell structure. Ref. `www.azurspace.com`

metalorganic chemical vapour deposition (MOCVD) process starting from a germanium substrate. Figure 1.6 shows the structure of a monolithic 3J solar cell. Commercial 3J solar cells, also called III-V multijunction, are composed by InGaP/InGaAs/Ge, and their particular structure makes them sensitive to a wavelength range from 350 to 1800 nm. The three sub-junctions are also known as top, middle, and bottom sub-cells, respectively, and they are separated through two interband tunnel diodes. In this configuration the 3J solar cell has a voltage that is the sum of the three p-n junction voltages and it generates a current that is the minimum of the three sub-currents. More details on the equivalent electric circuit of a 3J solar cell will be given in chapter 5. Current mismatch is a limit for a 3J solar cell, because the cell is always limited by the sub-junction that generates the lowest current. This problem concerns only the top and the middle sub-junctions, because the bottom junction always generates an excess of electron-hole pairs. Current mismatch between top and middle sub-junctions depends by some factors, that are their thickness, their lattice composition, and the incident spectrum. Over the years the topic concerning the choice of the appropriate reference spectrum for CPV has been deeply investigated [33] [34] and the $ASTMG173-03$[2] is now taken as the reference one. According to this choice, top and middle sub-junctions are nowadays designed in order to generate the same amount of current under this spectral condition. In this PhD dissertation a specific 3J solar cell has been used in outdoor tests, that is the Lattice Matched (LM) Spectrolab C3MJ. With this generation of 3J solar cell Spectrolab claimed a 41.6% world record efficiency [35] and 3J having a typical 39.3% efficiency is currently available on market [36]. The integral irrandiance of the $ASTMG173-03$ curve is $900\mathrm{W/m^2}$ and according to this choice some authors [37] define

$$1sun = 0.09\mathrm{W/cm^2} \tag{1.2}$$

Figure 1.7 represents the superimposition of the reference spectrum and the number of electron-hole pairs generated by a Spectrolab C3MJ solar cell. The colored curves have been obtained multiplying the reference spectrum with the External Quantum Efficiency (EQE) of the solar cell. Calculating the integrals under the colored curves, the minimum short-circuit density current is $12.2\mathrm{mA/cm^2}$ and is generated by the TOP p-n junction. According to this value, an equivalent definition of *sun* is[3]

$$1sun = 12.2\mathrm{mA/cm^2} \tag{1.3}$$

[2]American Standard Testing and Materials reference solar spectrum, AirMass 1.5 Direct+circumsolar. More details can be found in ref. `http://rredc.nrel.gov/solar/spectra/am1.5/`

[3]Over the years the definition of *sun* has repeatedly been under discussion and nowadays some authors define $1sun$ as $1000\mathrm{W}/m^2$, or equivalently $13.6\mathrm{mA/cm^2}$ [38].

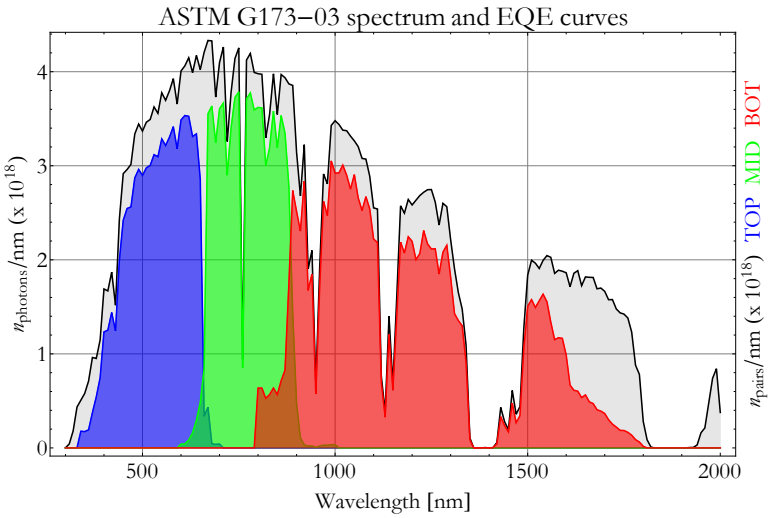

Figure 1.7: Black line: $ASTMG173-03$ standard solar spectrum expressed in $n_{photons}$/nm. Red, green and blue lines: 3J External Quantum Efficiency weighted with the $ASTMG173-03$ spectrum. The colored areas represent the electron-hole pairs generated by the three p-n junctions under the standard spectrum. Data taken form `www.nrel.gov` and `www.spectrolab.com`

1.3 Nonimaging optics design basics, particularly for CPV application

Nonimaging optics is a branch of optics which goal is to study the radiation transfer from a source to a target. According to figure 1.2, during the radiation transfer process no care is taken for the conservation of the source's spatial information because image formation is not required. Table 1.1 highlights some differences between imaging and nonimaging optics.

1.3.1 Optics design workflow

During the process of designing new optics an optical designer have to deal with some key steps that are now summarized. The approach that is now described is valid for imaging as well as nonimaging optical problems.

- **Statement of the problem and constraints analysis**. At the very first step the optics design process is faced through a research about prior art concerning the problem. The research must also be extended to technological processes and materials that could be used for prototyping and producing. This is a key step in the workflow because

Imaging	Nonimaging
- sequential ray-tracing	- non-sequential ray-tracing
- conic surfaces (spherical and aspherical)	- freeform surfaces
- target parameters: field-of-view, focal length, aberrations ...	- target parameters: illumination profile, power, maximum irradiance ...
- optimization and tolerance analysis are already implemented in the softwares and there's a strong know-now	- optimization and tolerance analysis are dependent by the problem involved
- high-level surface accuracy and finishing ($\lambda/4$ at least)	- surface accuracy and finishing are application dependent

Table 1.1: Comparison between imaging and nonimaging optics.

the state-of-the-art of the chosen technologies fixes some of the tolerances involved. Constraints could be of various type (technological, mechanical, physical, economical) and these fix the boundaries within which the optics can be designed. Constraints are highly dependent on the problem involved, so more details on the particular case study described in this thesis will be given in section 2.1.

- **Design method**. The design of an optics can be faced with a direct or an inverse approach. In the first case the image (for imaging), or illumination profile (for nonimaging), quality is a function of the system parameters, so direct problems are faced looking for analytic solutions. In the second case the target is to obtain at least a fixed image, or illumination profile, quality, so inverse approach looks for an optimized solution that lies within the required specifications. Numerical optimization is the core of the latter approach so it is helped by high computing speed. Inverse approach is the design method adopted for the nonimaging optics study presented in this thesis.

- **Surfaces parametrization**. This is often an easy step for an imaging optical designer, because the surfaces adopted in imaging problems are conics since ever. Moreover there's a strong knowledge about the properties of conic surfaces in imaging applications. Nonimaging problems are instead faced using freeform surfaces, particularly since last decade due to the progress in manufacturing optical components with Computer Numerical Control (CNC) machines. Moreover nonimaging optics also require a limited number of optical components in order to design a cost effective optics and to maximize the ratio between the input and the output radiative power. For these reasons freeform

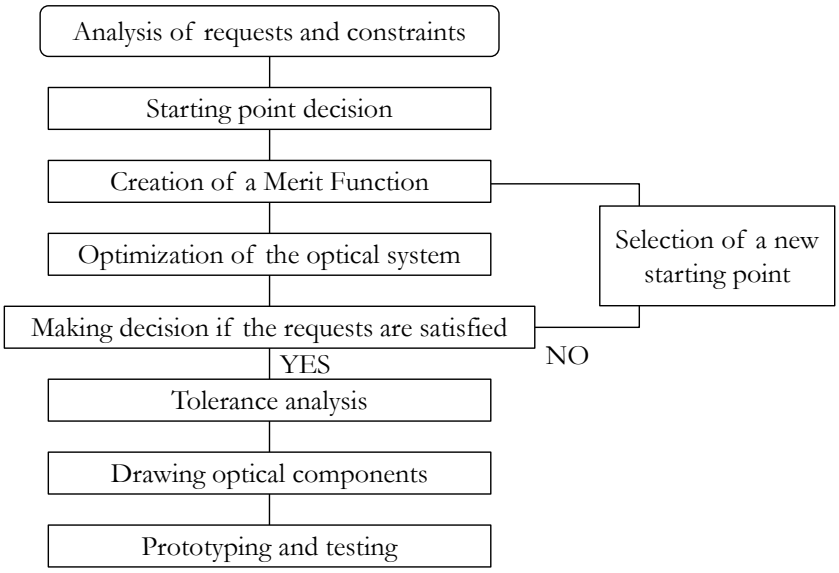

Figure 1.8: Stages of the optical design procedures. Taken from ref. [41]

surfaces are widely adopted in nonimaging applications. It is still under discussion in the community of optical designer which is the most appropriate way to parametrize a freeform surface. Nowadays XY polynomial, Zernike polynomial, and NURBS are some of the most common choices [39] [40]. The first and the third are in particular adopted in nonimaging systems.

- **Choice of target parameters and optimization method**. An inverse problem is faced applying the same method with imaging as well as nonimaging optics. The goal is to get a good starting point for the subsequent optimization process. The research of a good starting point begins with the choice of the appropriate variables and the definition of target parameters. The link between variables and target is a function called Merit Function (MF or sometimes Objective Function or Error Function), which is the object that the optimization software tries to minimize in order to get a satisfactory optical system. Optimization routines are usually already implemented in ray tracing softwares and nowadays these softwares use variants of the so-called Damped Least Square (DLS) method, which goal is to find a local minimum of the Merit Function starting from the specified starting point. By the way, there are situation in which the MF space has a large number of dimensions (i.e. the MF has many variables), so DLS method gives almost ever a minimum that is not the global one. Global

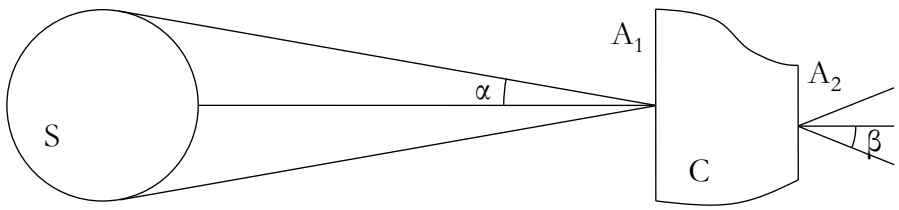

Figure 1.9: Concept scheme of a solar concentrator. A source S emits radiation that is collected by concentrator C having an entrance and an exit aperture A_1 and A_2, respectively. Light rays hit A_1 with a maximum incident angle α, while on A_2 rays arrive with a maximum incident angle β.

optimization methods are under discussion since decades [42] [43], but it's only during last years that they have been implemented in ray tracing softwares, benefitting from the increase in computing speed. More details on the topic of optimization methods can be found in ref. [44].

- **Tolerance analysis**. According to [45] tolerance analysis of nonimaging systems is in its infancy. There are nowadays lacks in software tools so that an optical designer has to manually set up the scheme to determine the sensitivity of the tolerance parameters. This process is time consuming and also dependent on the experience of the designer. Once that the error scheme is complete, a Monte Carlo simulation generates the distributions of the tolerance parameters. The type of errors introduced in a nonimaging optics that are taken into account into this work are system and process errors. System errors refer to incorrect position and misalignment of an optical component respect to the others, while process errors occur during fabrication process, so they refer to incorrect shape of the optical components (for example a wrong injection molding process). A complete tolerance analysis needs the knowledge of all the tolerances (i.e. the distribution of each parameter) involved during the production an optics. This data can be obtained form literature, previous experience, and also from measures of prototypes, and they must be confirmed once that the production line is in operation.

1.3.2 Solar concentrator design basics

Collecting sunlight requires an optics with an entrance and an exit aperture, A_1 and A_2 respectively, as shown in figure 1.9. The ratio between these two areas is defined as the geometrical concentration factor

$$C_g = \frac{A_1}{A_2} \tag{1.4}$$

Using thermodynamical and geometrical considerations [46] [47] it is possible to demonstrate that the maximum achievable concentration factor for a 3D concentrator is

$$C_{max} = \left(\frac{n}{\sin\alpha}\right)^2 \tag{1.5}$$

where n is the refractive index in which A_2 is immersed and α is the incident angle on A_1. Equation (1.5) supposes that incident angles distribution on A_2 ranges from null to $\pi/2$, but this condition is almost always impossible or inefficient. More often the maximum incident angle on A_2 is β, less than $\pi/2$. According to ref. [46] the geometrical concentration factor C_g cannot exceed the limit

$$C_g \leq \left(\frac{n\sin\beta}{\sin\alpha}\right)^2 \tag{1.6}$$

so, during the design of a concentrator a trade-off between geometrical concentration factor and optical efficiency must be studied. Equation (1.5) is also usually written in the following way

$$CAP = \sqrt{C_g}\sin\alpha \geq n \tag{1.7}$$

This equation defines the Concentration-Acceptance Product (CAP) factor [48] and it describes how close the concentrator system is to the maximum thermodynamic limit. When equation (1.7) is applied to a concentrator optics, α is the acceptance angle of the system, which is defined as the misalignment angle within the system performance is at least 90% of its maximum. As a rule of thumb, the higher the desired concentration factor, the lower the achievable acceptance angle.

1.3.3 Optical schemes for CPV

A typical optics for CPV is composed by several components

- front cover, for example glass or PMMA
- Primary Optical Element (POE), that can be reflective or refractive
- Secondary Optical Element (SOE), that is a reflective or refractive light guide close to the solar cell
- target, that is the solar cell

Depending on the choices made at the beginning of the project some of the previous elements could be unnecessary or a single element could perform

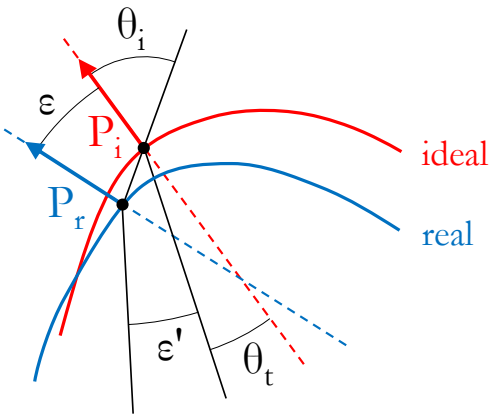

Figure 1.10: The figure represents the different light paths after a refractive interface due to surface differences. The red and the blue lines are, respectively, the ideal and the real refractive surfaces, which are hit by a light ray in the points P_{ideal} and P_{real}. The angles θ_i and θ_t are the incident and transmitted angles, while ϵ is the angle between the normal vectors in n_{ideal} and n_{real}

multiple functions. The fundamental optical element into a concentrator is the POE because it defines the geometrical concentration factor. Nonimaging optics for CPV can be divided in two groups, depending by POE. If a refractive optical element is used then the system has some advantages such as potentially high optical efficiency and easy thermal management, but is affected by chromatic aberration, particularly at high concentration factor. If instead a reflective element is chosen then the system takes advantage form the absence of chromatic aberration, but it is more challenging to obtain high optical efficiency because an additional front glass (or plastic) cover is needed.
According to figure 1.10, let's consider an optical surface and a ray that impinges on it. The expected incidence point is P_i, but due to manufacturing errors and/or misalignment the real incidence point is P_r. The most important difference for optical purposes between these two points is that they identify two different normal vectors. It can be shown [49] that a small slope error ϵ produces a deviation ϵ' with respect to the expected exiting ray

$$\epsilon' = a\epsilon \tag{1.8}$$

with

$$a = \begin{cases} 2 & \text{mirror} \\ 1 - \frac{\tan\theta_t}{\tan\theta_i} & \text{lens} \end{cases} \tag{1.9}$$

Classification	Geometrical conc. factor	Tracking system
Low	$1 \leq C \leq 10$	None or single-axis
Medium	$10 \leq C \leq 100$	Single- or dual-axis
High	$100 \leq C \leq 1000$	Dual-axis

Table 1.2: Classification of CPV systems.

where θ_i and θ_t are, respectively, the incident and the exit (reflected or refracted) rays calculated respect to the theoretical surface. Equation (1.9) states that an additional advantage of refractive optics is that they are less sensitive to contour errors respect to mirrors, so care must be taken in manufacturing mirrors. Within this project a mirror-based CPV optics had been chosen for several reasons

- at high concentration factors the chromatic aberration generates unacceptable power losses
- yellowing of plastic Fresnel lenses is also a challenge question [50] [51]
- plastic injection molding process for lighting reflectors is nowadays a mature, precise and affordable technology

A typical way to classify the variety of existing CPV systems is their geometrical concentration factor. According to ref. [52] and table 1.2, Low-Concentration Photovoltaics (LCPV) refers to systems with a concentration factor below 10× and enhance conventional silicon-based solar cells, while High-Concentration Photovoltaics (HCPV) refers to systems with a concentration factor over 100× and enhance high-efficiency multijunction solar cells. Medium-Concentation photovoltaics (MCPV) is instead an unexplored class since many years because this kind of systems do not allow a convenient trade-off between cost and efficiency.

Chapter 2

Nonimaging optics design workflow

This chapter begins with an introduction on how to face the problem of designing a nonimaging optics and some design techniques are listed. The case study of the TwinFocus® optics is then faced starting from a detailed analysis of the constraints and a design method is subsequently presented. The solution is then optimized and in conclusion the resulted optics is analyzed. Deeper analysis of optics performances and tolerances are treated in the next chapters.

The design of optical surfaces is possible using two different approaches: direct design methods and numerical optimization.

Direct design methods concerns analytic approaches, because the image quality is a function of the constructional parameters of the system. This formulation is also known as direct problem: given a well known input (usually described through ray bundles or wavefronts), these approaches are mathematical procedures to design optical surfaces that transfer such input to a prescribed target distribution. There are basically two different direct design methods.

- Coupling incoming with outgoing wavefront(s). Over the years this problem was faced many times and in its simplest formulation it involves spherical incoming and outgoing wavefronts. The solution to this problem is the well known *cartesian oval*. A general solution that involves a single non-spherical wavefront was presented at the beginning of 1900 [53]. More recently a method that can handle multiple wavefronts in three dimensional space was presented [54] and it is currently known as Simultaneous Multiple Surface (SMS) method. This

method has been effectively applied to handle up to three wavefronts with two freeform surfaces [55].

- Coupling prescribed input and output intensity patterns. Once that the problem is formulated in this form it involves second order partial differential equations, also known as Monge-Ampere equation [56], so a numerical solution of such equations is required [57].

Optimization methods try to solve an inverse problem: the goal is to design an optics that satisfies some minimum requirements such as field of view, effective focal length, RMS spot size, and much more for imaging, or such as power collected, acceptance angle, profile uniformity and much more for nonimaging. These methods are based on the minimization of a Merit Function (MF) that describes the optical properties as a function of some appropriate parameters. An inverse problem can be faced in various way due to the MF arbitrariness, but it is interesting to notice that a common approach uses the so-called *supporting ellipsoid* method that has been applied in various variants [58] [59] [60].

For this project an optimization approach has been chosen, so an appropriate parametrization of the optical surfaces and the choice of a suitable MF are very important. Before these steps it is fundamental the study of the problem constraints.

2.1 Constraints analysis and starting decisions

Designing a new optics starts from the statement of an optical problem, a conceptual solution and some choices made after a constraints analysis. Conceptual solution is shown in figure 2.1: a light source, that here is approximated with a planar wavefront, emits light that passes through a front cover glass, is then reflected from a Primary Optical Element (POE), then refracted from a Secondary Optical Element (SOE) and at the end collected by a 3J solar cell. The combination of POE and SOE is defined *doublet*: for this reason this the CPV system that uses this optical scheme is called TwinFocus®. This optical scheme includes also a layer of optical glue between SOE and 3J solar cell. Moreover 3J cell has an Anti-Reflection Coating (ARC) that matches the refractive indexes of glue and 3J front window. TwinFocus® layout has been chosen to conciliate a small system volume with small angles of incidence on the SOE and on the 3J solar cell, so to reduce Fresnel losses.

2.1.1 Technological constraints

As already explained in section 1.3.3, a mirror-based optical schemes has been chosen for several reasons. Basically it is to avoid chromatic aberra-

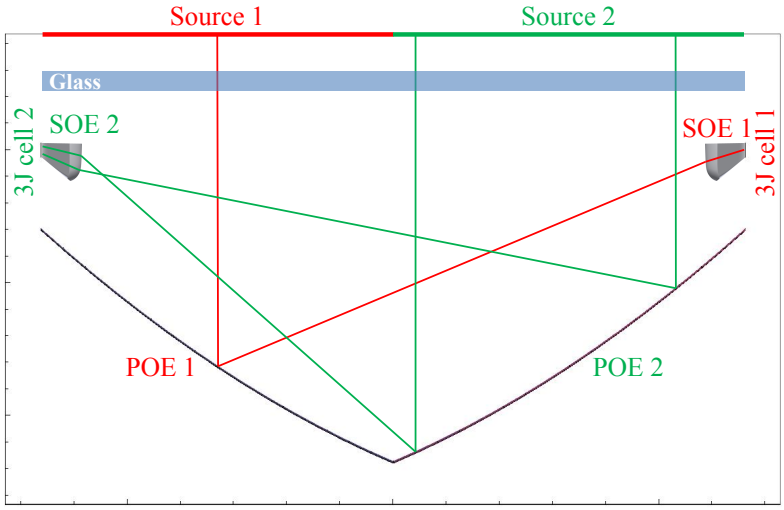

Figure 2.1: TwinFocus® system optical scheme. A light source, that here is simplified with a planar wavefront, passes through a front cover glass, is then reflected by a Primary Optical Element (POE), then refracted by a Secondary Optical Element (SOE), and finally collected by a 3J solar cell. The combination of two of these optical schemes is shown in figure, so the CPV system that uses it is called TwinFocus®.

tions introduced by lenses with small aspect-ratio and also to use a mature and cost effective technology like plastic injection molding. Technological constraints deal with materials and production processes. Table 2.1 shows the materials and the production choices. The front cover is a low-iron glass. Its selection has been a trade off between optical efficiency, particularly in the UV spectral region, and cost. POE is a polycarbonate substrate made through an injection molding process that is aluminazed and protected using a Physical Vapor Deposition (PVD) process, while the SOE is a SiO_2 light-guide made through a SiVARA™Sol-Gel process. The optical glue is a standard product in the optical components industry, it resists to high light fluxes and it has a refractive index close to the SOE one. Finally the 3J solar cell is a standard component in CPV market: it has a dedicated ARC and its EQE is also well known.

2.1.2 Mechanical constraints

Mechanical constraints define the volume of the optical components and their relative position. The most important mechanical constraint involves the geometrical concentration factor C_g: once that a 3J commercial cell has been chosen, C_g is fixed by the POE surface dimension. 3J solar cell efficiency is a function of light irradiance (so it is a function of C_g) and it

Component	Material	Production process - Note
Front cover	Low-iron glass	Small losses in UV spectral region
POE	PC with Al coating	Injection molding, PVD
SOE	SiO_2	SiVARA Sol-Gel
Optical glue	—	Refractive index matches SOE
3J cell	III-V semiconductors	MOCVD, monolithic

Table 2.1: Materials and production processes

usually is maximal between $200suns$ and $700suns$. A geometrical concentration factor of about $800\times$ has been chosen and an actual irradiance of $500suns$ is expected after the optical losses. Once that the optics design has been completed C_g has been correctly calculated including shadows due to some mechanical components. This is the resulting value

$$C_g = \frac{\text{Effective POE area}}{\text{Effective 3J area}} = \frac{237\text{cm}^2}{(0.55 \times 0.55)\text{cm}^2} = 783\times \tag{2.1}$$

3J solar cell position and orientation are also fixed. Its orientation has been chosen in order to reduce shadows on the POE, and its distance from the mirror is enough to avoid a critical system failure in the case in which the optics is not correctly aligned and the concentrated light doesn't hit the solar cell but the POE. A minimum distance from POE and 3J of approximately $30mm$ has been fixed. SOE has no restrictions for mechanical reasons, but a limit on its volume is discussed in section 3.3.

2.1.3 Physical constraints

Fresnel equations describe what happens when light moves from a medium of refractive index n_1 to a medium of refractive index n_2. A fraction of the light is refracted and another fraction is reflected. The higher the difference between the refractive indexes, the higher the reflected fraction. Moreover, if the light is unpolarized, the higher the incidence angle, the higher the reflected fraction. This phenomenon is described by the equation

$$R = \frac{1}{2}\left[\left(\frac{n_1\cos(\theta_i) - n_2\cos(\theta_t)}{n_1\cos(\theta_i) + n_2\cos(\theta_t)}\right)^2 + \left(\frac{n_1\cos(\theta_t) - n_2\cos(\theta_i)}{n_1\cos(\theta_t) + n_2\cos(\theta_i)}\right)^2\right] \tag{2.2}$$

where n_1 and n_2 are the refractive indexes of the media, θ_i and θ_t are the incidence and the transmitted angles. Equation 2.2 says that to achieve an efficient optics the incidence angles must be small, as well as the difference between the refractive indexes. TwinFocus® optical scheme has been studied to have small incidence angles on the SOE and on the 3J. SOE has a

refractive index in the visible range of about 1.46, so air-SOE interface produce an optical loss of 3.5%. This loss is approximately constant for angles of incidence below 50°, so this value has been kept as a physical constraint. 3J cell is instead even more tolerant to high angles of incidence due to its Anti-Reflection Coating (ARC): it is mandatory to deposit on any kind of solar cell, even on Si-based modules, an ARC to fit the solar cell refractive index with its surround (for example air or a glass optical element). This coating makes the 3J cell less sensitive to incidence angle, and Fresnel losses become heavy only over 75°, so this is a second physical constraint.

2.1.4 Economical constraints

While a mass-production is planned for this system, the cost of the tools (such as the mold or the assembling line) must be considered with an appropriate low weight in the calculation of the projected system cost. Injection molding of PC is a cost effective solution, so POE has no other constraints. SiVARA Sol-Gel process is also an affordable solution during mass production, but a restriction on the SOE volume of about 1.5cm^3 has been fixed in order to limit its cost. The small layer of optical glue has no impact on the final cost, so it has no constraints. Finally, the front cover is a low-iron glass and not, for example, a more efficient quartz window: this choice is a trade-off between optical efficiency and system cost. More details about cost analysis can be found in section 3.3.

2.2 Generation of reflective and refractive surfaces

Once that initial constraints have been chosen it is possible to face the inverse problem of designing the optical surfaces. First of all an algorithm must be developed in order to link the source (the Sun) and the target (the 3J solar cell) through some reflective/refractive surfaces. Then a starting decision, according to the constraint analysis, must be done. This choice is then the starting point of the subsequent optimization process, which is performed using an appropriate Merit Function (MF). Finally, if the solution satisfies the target requirements a tolerance analysis can be performed, otherwise a different initial point must be chosen.

2.2.1 Algorithm: mapping the source into the target

Once that the source and the target have been defined, a map between them is required. This map is based on the flux conservation principle, so it can be found using an equi-flux grid method [60]. If $S(x, y)$ and $T(y', z')$ are, respectively, the source and the target irradiance distribution then

$$\int\int S(x, y)\ dx\, dy = \int\int T\left(y', z'\right)\ dy'\, dz' \tag{2.3}$$

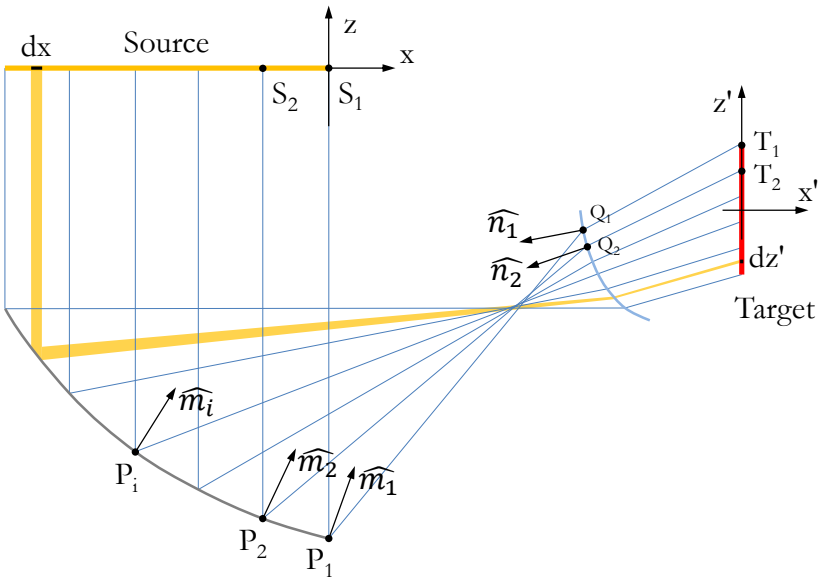

Figure 2.2: Bi-dimensional TwinFocus® optics. A light ray starts from S_1, passes through the *seed points* P_1 and Q_1, and is finally collected in T_1. The resulting normal vectors $\widehat{m_1}$ and $\widehat{n_1}$ are then used to iteratively calculate all the P_i and Q_i points.

where x, y, y', z' could be angular or spatial variable. According to figure 2.3, TwinFocus® optical problem involves only spatial variables. When the system has rotational or translational symmetry, the optical design process is a bi-dimensional problem: if an uni-dimensional map between source and target is found, then the full optical surface can be obtained by sweeping the curve around its axis of symmetry. In this simple case, equation (2.3) involves uni-dimensional integrals and the map between source and target can be analitically found.
Figure 2.2 shows a simplified problem concerning a bi-dimensional TwinFocus® optics: a source (a planar wavefront) is reflected, then refracted and finally collected by a target. Both the source and the target are divided into bins, and each bin is associated to a specific irradiance value. The equi-grid flux equation states

$$\int S(x)\, dx = \int T\left(z'\right)\, dz' \tag{2.4}$$

A requirement of TwinFocus® optics is that the target irradiance must be uniform, as well as source irradiace, so both $S(x)$ and $T(z')$ are constant functions

$$S(x) = C_S \qquad \text{and} \qquad T\left(z'\right) = C_T \tag{2.5}$$

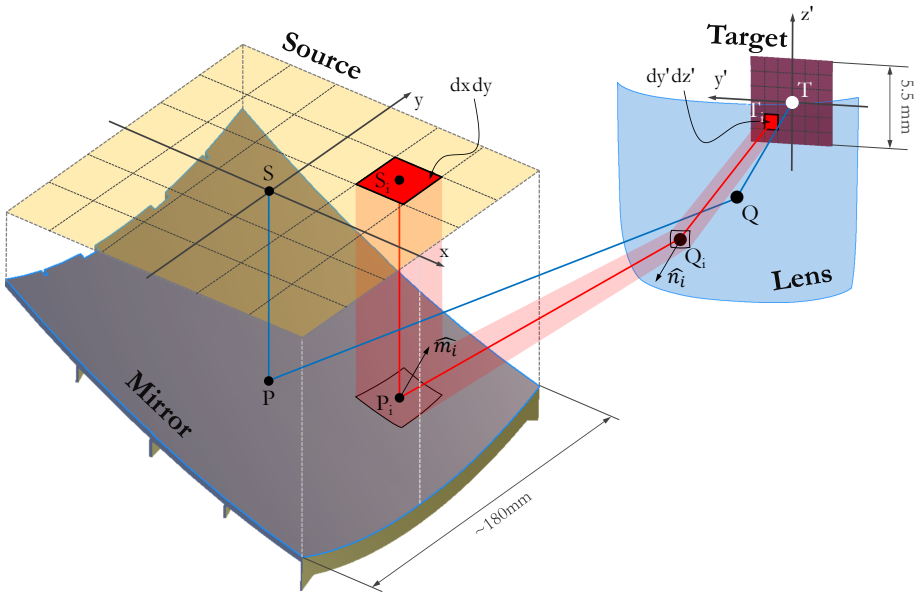

Figure 2.3: Three-dimensional TwinFocus® optics. The map between the source and the target is a relationship between two grids, so each element $dx\,dy$ is transferred through a mirror and a lens in the element $dy'\,dz'$

so the map between source and target is simply

$$z' = \frac{C_S}{C_T} x \tag{2.6}$$

At this point, once that the map is known, is it possible to iteratively draw the optical surfaces. As shown in figure 2.2, let's suppose that a ray starting from the point S_1 must be collected in the point T_1. To calculate the complete optical path a point P_1 on the reflective surface and a point Q_1 on the refractive surface must be chosen. P_1 and Q_1 are also known as *seed points* (or *starting points*). The resulting normal vectors $\widehat{m_1}$ and $\widehat{n_1}$, which have been calculated according to the Snell's laws, are then used to move on to the next points P_2 and Q_2. The new normal vectors $\widehat{m_2}$ and $\widehat{n_2}$ can then be computed, an so on until the entire curves are completed. Once that the point clouds P_i and Q_i are known, they are fitted using a polynomial equation and the optical problem is solved. The method shown in figure 2.2 is closer to the ideal solution the more populated are the point clouds. A way to calculate a smaller number of points, so to speed-up the process, and to obtain more accurate surfaces was developed by Elmer [61] and effectively used in recent works [62].

Without rotational or translational symmetry, the design problem is three-

dimensional and equation (2.3) involves a Monge-Ampere type differential equation [63], which solution is used to be unstable with standard numerical integration techniques. As a result, there is no general way to find a map between source and target unless some symmetry exists, in which case we can separate the integration variables and solve two simpler differential equations.
The general 3D problem involved in TwinFocus® optics is presented in figure 2.3. According to the flux-conservation principle expressed in the equation (2.3), a map between the source and the target must be found: every source element $dx\,dy$ must be linked to a target element $dy'\,dz'$ with a bijective relation. Mapping a source into a target is always possible and an infinite number of maps exist, but a generic map does not ensure that the generated point clouds can be fitted with continuous surfaces. Finding a map is therefore not sufficient: we need to find a map that ensures surface continuity. Only a map that fulfills the integrability condition generates a smooth optical surface [64]. With reference to figure 2.3 let's suppose that a chosen map generates the point clouds P_i and Q_i. All these P_i and Q_i points lye, respectively, on the reflective and on the refractive surface and each pair (P_i, Q_i) is associated to the elements $(dx\,dy)$ $(dy'\,dz')$ and to the vectors $(\widehat{m_i}\,\widehat{n_i})$. Once that all this data has been obtained, the surface continuity must be checked. This means that integrating the surface normal vectors along any closed path a closed curve must be obtained. Continuity constraint can therefore be stated with a contour integral

$$\oint_C \hat{m}\,d\vec{l} = 0 \tag{2.7}$$

where C is an arbitrary closed contour over the surface, $\hat{m}$ (or $\hat{n}$) is the field of normal vectors and $d\vec{l}$ is an infinitesimal displacement along the source grid. This topic has been largely investigated in recent years [60], but always studying only a reflective surface and not a reflective-refractive doublet. At this point of the optical design process is acknowledged that looking for a TwinFocus® optics through this way is challenging and time consuming. Moreover a concentrator optics requires to consider different incoming wavefronts in order to take into account system misalignments. This approach has been proficiently developed with the so called SMS proprietary method [54] [65].
Acknowledging these considerations, the choices that are now presented are made without involving any continuity constraint. According to figure 2.4 a first choice is to divide the POE into four reflectors in order to make the target distribution less sensitive to the reflector shape. In this new configuration each POE's sector concentrates the sunlight with an uniform illumination profile on the 3J cell, so that small local variations in the POE shape have a small impact on the target distribution. In this way the risk that the

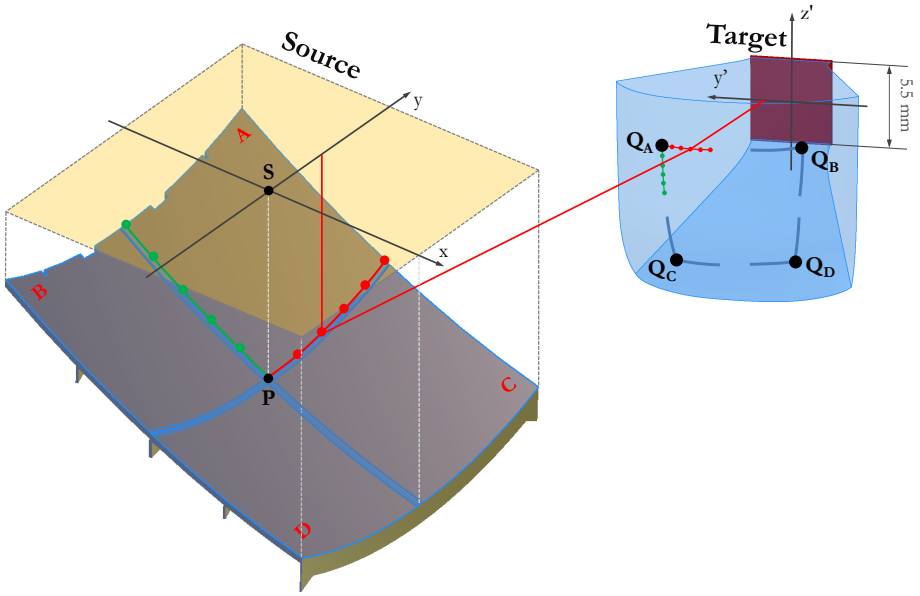

Figure 2.4: Representation of the source-target relationship: the axes x and y lying on the source surface are mapped respectively on the axes z' and y' lying on the target surface through an iterative method.

target receives locally a high irradiance has been limited. A number of four sectors has been chosen because this is a trade-off between the risk of local high irradiance and optical efficiency: each mirror sector has a border and during the cooling step of the injection molding process each discontinuity creates local warpages, so the larger the number of mirror facets the lower the optical efficiency. The number of 4 sectors has been chosen matching the research group experience in designing plastic optical mirrors and that of the mold manufacturer.
A simple map between the source and the target has been initially chosen: a separation of variables was made. A according to equation (2.4), two independent relations between the source and the target were studied

$$\int_0^{L_x} S(x)\, dx = \int_0^{L_{z'}} T(z')\, dz' \quad \text{and} \quad \int_0^{L_y} S(y)\, dy = \int_0^{L_{y'}} T(y')\, dy' \tag{2.8}$$

where L_x and L_y are the source's lengths along x and y axes, while $L_{z'}$ and $L_{y'}$ are the target's lengths along z' and y' axes. The axes are defined in figure 2.4. Because a constant illumination profile on the 3J cell is required and because the source has a constant irradiance, then

$$S(x) = S(y) = C_S \quad \text{and} \quad T(z') = T(y') = C_T \tag{2.9}$$

where C_S and C_T are respectively the source and the target irradiance. The solution of equation (2.8) is simply

$$\frac{L_x}{L'_z} = \frac{L_y}{L'_y} = \frac{C_T}{C_S} \tag{2.10}$$

where the ratios L_x/L'_z and L_y/L'_y define respectively the geometrical concentration factors along two different axes. According to the *Sun* quantity defined in equation (1.2) and according also to the geometrical concentration factor defined in equation (2.1)

$$C_g = \frac{L_x}{L'_z}\,\frac{L_y}{L'_y} = \frac{{C_T}^2}{{C_S}^2} = \frac{{C_T}^2}{1\,Sun} \tag{2.11}$$

so the expected irradiance on the target, considering only ideal surfaces (i.e. unitary reflectance of POE and unitary transmittance of front cover glass, POE, and optical glue), is

$${C_T}^2 = 1\,Sun \cdot C_g = 0.09\frac{\mathrm{W}}{\mathrm{cm}^2} \cdot 783\times = 70.5\frac{\mathrm{W}}{\mathrm{cm}^2} \tag{2.12}$$

Because of the linearity of equation (2.10), a map between the source and the target along x and y axes has been found with the relation

$$\Delta x\, C_S = \Delta z'\, C_T \qquad \text{and} \qquad \Delta y\, C_S = \Delta y'\, C_T \tag{2.13}$$

where Δx and Δy are small steps lying on the source surface while $\Delta z'$ and $\Delta y'$ are the corresponding steps lying on the target surface. The iterative method presented in figure 2.2 has then be applied along the two axes in order to create several point clouds. This designing step requires the definition of some starting points, such that represented in figure 2.4 named P, Q_A, Q_B, Q_C, Q_C. It is quite natural to choose P at the center of the POE because it is shared by all the reflective sectors. It is a bit harder to choose the starting points Q_i $(i = A, B, C, D)$ SOE because this choice requires to know the final volume and the entrance aperture area of the SOE: the first one is directly related to the price of the optical element, and the second one is related to the acceptance angle. The choice of these four Q_i starting points is then a tradeoff between the cost and the tolerance of the system. In particular, as already discussed in section 2.1.4, the requirement for the SOE is to have a minimum volume (about $1.5\mathrm{cm}^3$) able to increase the acceptance angle at least to $\pm 1^\circ$ for both x and y axes. The last requirement concerning the SOE involves the size of the exit aperture, which is the surface in contact with the solar cell. In order to increase the tolerances, and in particular to avoid losses of light, the SOE's exit aperture has an area smaller than the solar cell. For this reason a $5.5x5.5mm^2$ solar cell was chosen, and a SOE's exit aperture of $5.3x5.3mm^2$ allows tolerances of $\pm 0.1mm$ in the relative positioning of the SOE and the cell. After the construction

of the point clouds using the iterative Elmer's method, a polynomial fit of each points group was calculated. The points on the POE along x and y axes were fitted using fourth order polynomial functions

$$z = z_0 + a_x(x - x_0) + a_{x^2}(x - x_0)^2 + a_{x^4}(x - x_0)^2 \tag{2.14a}$$

$$z = z_0 + a_y(y - y_0) + a_{y^2}(y - y_0)^2 + a_{y^4}(y - y_0)^2 \tag{2.14b}$$

where (x_0, y_0, z_0) are the coordinates of P. Starting from SOE's point cloud, a freeform surface that defines the whole SOE entrance aperture was obtained through a CAD software. The coefficients of POE's polynomial fitting curves were then used to define a 4^{th} order polynomial equation for each reflective surface (A, B, C, D in figure 2.4). The polynomial coefficients were then used as the starting point of the subsequent optimization process.

2.2.2 Optimization process

In this section an optimization workflow is presented. At this step of the design process no information about the spectral characteristics of any optical interface was introduced, due to the fact that during the designing process not all the spectral data were known. Once that the optimization process was concluded a ray tracing simulation was performed again including the spectral data. More details about the spectral performances of the optics can be found in section 2.3.
Starting from the 4^{th} order polynomial equation discussed at the end of the previous section that is now defined

$$\begin{aligned} z =& z_0 + a_x(x - x_0) + a_y(y - y_0) + \\ &+ a_{x^2}(x - x_0)^2 + a_{xy}(x - x_0)(y - y_0) + a_{y^2}(y - y_0)^2 + \\ &+ a_{x^3}(x - x_0)^3 + a_{x^2y}(x - x_0)^2(y - y_0) + a_{xy^2}(x - x_0)(y - y_0)^2 + a_{y^3}(y - y_0)^3 + \\ &+ a_{x^4}(x - x_0)^4 + a_{y^4}(y - y_0)^4 \end{aligned} \tag{2.15}$$

a Merit Function (MF) is now introduced. The coefficients (x_0, y_0, z_0) represent the coordinates of the starting point P. After several optimization approaches, a 4^{th} order equation of the kind described in (2.15) was chosen: a 3^{rd} order equation hasn't enough degrees of freedom to create the desired illumination profile, while an equation that involves also the 4^{th} order mixed terms has too much parameters and generates a difficult convergence during the optimization. Equation (2.15) involves 11 coefficients, so the MF of each reflective sector lives into a 11-dimensional space. The choice of a polynomial surface for the description of the POE was made according to the ray tracing software used: the software offers the possibility to define n^{th} order

polynomial equations, but not more general surfaces such as Non-Uniform Rotational B-Spline (NURBS), so the optimization can be performed only with polynomial surfaces. The final target illumination profile is governed by the POE shape, so it was chosen not to include variations on the SOE entrance surface during the optimization process.
The requirement of uniformity of the target illumination profile was translated into a requirement of irradiance constancy over the 3J. The target was divided into 5×5 subcells, as shown in figure 2.4, and it was required that each subcell collected the same number of rays. Moreover it was required that all the rays generated by the source, said N_{rays}, were collected by the target. The MF was then defined as follows

$$\mathrm{MF} = \sum_{i=1}^{25} (n_i - n)^2 \tag{2.16}$$

where $n = N/25$ is the expected number of rays collected by a generic i^{th}subcell and n_i is the actual number of rays collected. Such equation has been chosen because its minimization generates two effects: a maximization of the rays collected by the target and a maximization of the illumination profile uniformity. According to appendix A, a number of 5×5 subcells is the limit to achieve 1% statistical error on n_i of each subcell with $250,000$ traced rays. The higher the number of subcells the higher the number simulated rays (i.e. the computing time) required to contain statistical errors on the illumination profile. A discretization of 5×5 and a limit error of 1% has been chosen as an acceptable trade off.

A short dissertation concerning how a ray tracing software works and which instrument has been used during this optical design is now developed. All the ray tracing simulations have been performed using an Intel® Core™ i7-2600 CPU (3.40GHz). The ray tracing software allows parallel computation so advantage from this feature has been taken during the simulations. Computing speed depends by some factors like CPU speed, number of CPU cores and optical design complexity. Another important factor is the data volume carried by a ray during a simulation. It's important to notice tat each ray is defined by coordinates (x, y, z), cosine directors (n_x, n_y, x_z), wavelenght, and power. During a ray tracing simulation is it possible to forget the spectral properties of the optical surfaces defining them as ideal (i.e. mirrors with unitary reflectance and lenses with unitary transmittance). In this situation all the power carried by a ray is reflected, or transmitted. This is the software setup used during the design and the optimization processes. After that the spectral and angular properties of the optical interfaces were measured, these data were then included in the ray tracing software. In this configuration mirrors and lenses are not ideal anymore, so a process called *ray splitting* is involved: when a ray hits a surface it is partially reflected,

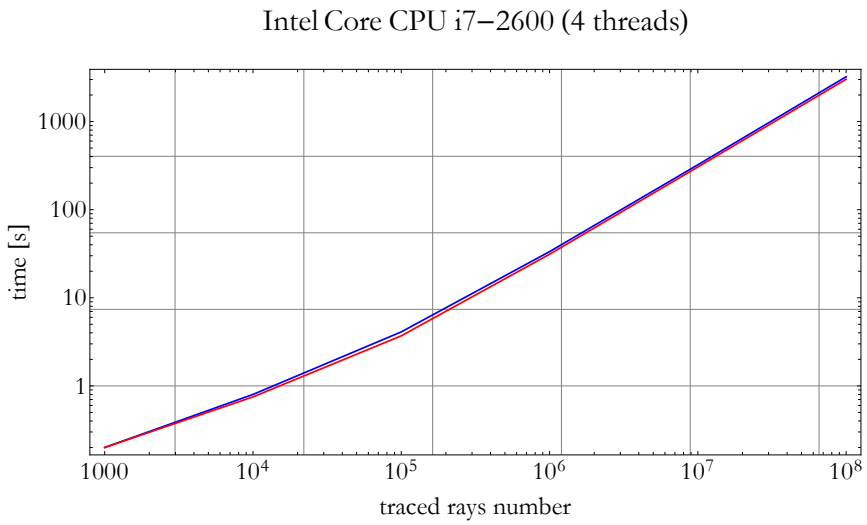

Figure 2.5: A comparison between an ideal ray tracing simulation (red line) and one in which surface's optical (spectral and angular) properties are considered (blue line). The time required in the two different configuration is almost the same. In both the situations the rate of simulated rays is approximately $32krays/s$.

partially transmitted and partially absorbed, so each ray generates two rays at every optical surface. This second configuration is definitely a better description of reality, but it is slower than the first one. If the optical surfaces are accurately defined is it possible to slow down the simulation by only a small factor. Figure 2.5 represents a comparison between an ideal ray tracing simulation and one in which surface's optical (spectral and angular) properties are considered. The time required in the two different configuration is almost the same.

The MF defined in the equation (2.16) has 25 targets and, as already discussed, it involves 11 parameters for each POE sector. A total of 22 parameters are then involved for the definition of the problem (according to figure 2.4 the sectors A-B and C-D are symmetrical). The "wildness" of the MF generates some problems during the optimization, because it is easy to fall into a local minimum. For this reason a Global Optimization method was used. This feature of the ray tracing software is not well documented because it uses a proprietary routine, but it's known that beginning form the starting point (i.e. 22 coefficients) the software looks for a global solution changing randomly the initial parameters and then optimizing them through a standard orthogonal descent algorithm.
At the end of the optimization process the solution can be accepted or rejected. The reasons of rejection are

Parameter	surface A	surface B	surface C	surface D
x_0	-65.80	-65.80	-65.80	-65.80
y_0	0.00	0.00	0.00	0.00
z_0	-90.00	-90.00	-90.00	-90.00
a_x	-0.6292	-0.6292	-0.6483	-0.6483
a_y	-0.0159	0.0159	-0.0164	0.0164
a_{x^2}	$1.765 \cdot 10^{-3}$	$1.765 \cdot 10^{-3}$	$1.820 \cdot 10^{-3}$	$1.820 \cdot 10^{-3}$
a_{xy}	0	0	0	0
a_{y^2}	$1.750 \cdot 10^{-3}$	$1.750 \cdot 10^{-3}$	$1.730 \cdot 10^{-3}$	$1.730 \cdot 10^{-3}$
a_{x^3}	$-5.0 \cdot 10^{-9}$	$-5.0 \cdot 10^{-9}$	$-3.0 \cdot 10^{-7}$	$-3.0 \cdot 10^{-7}$
a_{x^2y}	0	0	$-1.0 \cdot 10^{-7}$	$1.0 \cdot 10^{-7}$
a_{xy^2}	$5.0 \cdot 10^{-8}$	$5.0 \cdot 10^{-8}$	$1.0 \cdot 10^{-7}$	$1.0 \cdot 10^{-7}$
a_{y^3}	$2.0 \cdot 10^{-8}$	$-2.0 \cdot 10^{-8}$	$-5.0 \cdot 10^{-8}$	$5.0 \cdot 10^{-8}$
a_{x^4}	$2.5 \cdot 10^{-9}$	$2.5 \cdot 10^{-9}$	$-1.0 \cdot 10^{-9}$	$-1.0 \cdot 10^{-9}$
a_{y^4}	$2.0 \cdot 10^{-10}$	$2.0 \cdot 10^{-10}$	$1.0 \cdot 10^{-9}$	$1.0 \cdot 10^{-9}$

Table 2.2: Mathematical description of the POE's sectors.

- the number of collected rays is low. This means that not all the rays have been collected

- the target illumination profile has a low uniformity. This could happen because the starting point was not chosen accurately and the optimization didn't converged

- the incidence angles on the SOE or on the 3J cell are higher than the acceptable values

If these situations occur after an optimization process it is necessary to change the starting points. This means that different P, Q_1, Q_2, Q_3, Q_4 points must be defined and that the method represented in figure 2.2 must be applied again.

After several iterations the four POE's sectors reach a definitive description, that is reported in table 2.2, as well as the SOE entrance aperture. The latter optical element has a completely free form shape, so it's description is possible only through a CAD model. An iterative procedure was also adopted for the design of the inside walls of the SOE. These interfaces have a fundamental role in a real situation because they redirect the light rays on the target if the optical system has some manufacturing or alignment imperfections. The shape of the SOE's inside walls have been designed in order redirect the light rays on the target through a Total Internal Reflection (TIR) in any reasonable real situation. More details on the CAD models of the POE and the SOE can be found in chapter 3.

2.3 Spectral Transfer Function

A radiometric simulation of the optical system is necessary in order to link the optical performances to real physical quantities. An important radiometric quantity for the balance of the system is the power collected by the 3J solar cell. This value is important because it is directly related to the short-circuit current (I_{sc}) generated by the 3J solar cell. In a first approximation I_{sc} value is directly related to the electrical power generated by the 3J solar cell. This topic will be discussed in chapter 5. The knowledge of the power collected by the 3J cell is also mandatory because this value is related to the thermal budget the the cooling system has to handle.
In order to perform a complete radiometric analysis it is necessary to introduce in the ray tracing software the spectral properties of the source and of the optical elements. This is the list of the optical elements:

- front cover glass: Element Extralight 3.2 mm - Sangalli Vetro - solarglass;
- POE: polycarbonate aluminized and protected with SiO_2;
- SOE: fused silica;
- optical glue: Dow Corning® 3145 rtv mil-a-46146 adhesive/sealant;
- ARC: SiO_2 and TiO_2.

The front cover glass transmittance and the POE reflectivity were measured using the Ocean Optics NIRQuest512 ($900 - 1700$nm) spectrometers, while the Anti-Reflection Coating (ARC) transmittance was measured with a Varian Cary 5000 spectrophotometer. Glass and ARC transmittance were obtained at normal incidence while, according to figure 2.7, the POE reflectivity was measured at an incident angle of 30^o because this value is close to the average one. The SOE and the glue optical properties were instead obtained from their nominal refractive indexes. Fused silica properties were used for the SOE and, according to ref. [66], the same choice was made for the optical glue. More exactly the refractive index description of these optical elements is

$$n(\lambda) = 1.4441 + \frac{4479}{\lambda^2} \tag{2.17}$$

where λ is the wavelength expressed in nanometers. The product of all the reflectance and transmittance curves gave the Spectral Transfer Function (STF). This curve describes the spectral optical efficiency of the system.

2.4 Final result: illumination profile analysis

The result discussed at the end of section 2.2.2 is now analyzed including in the ray tracing simulation the spectral properties of each optical ele-

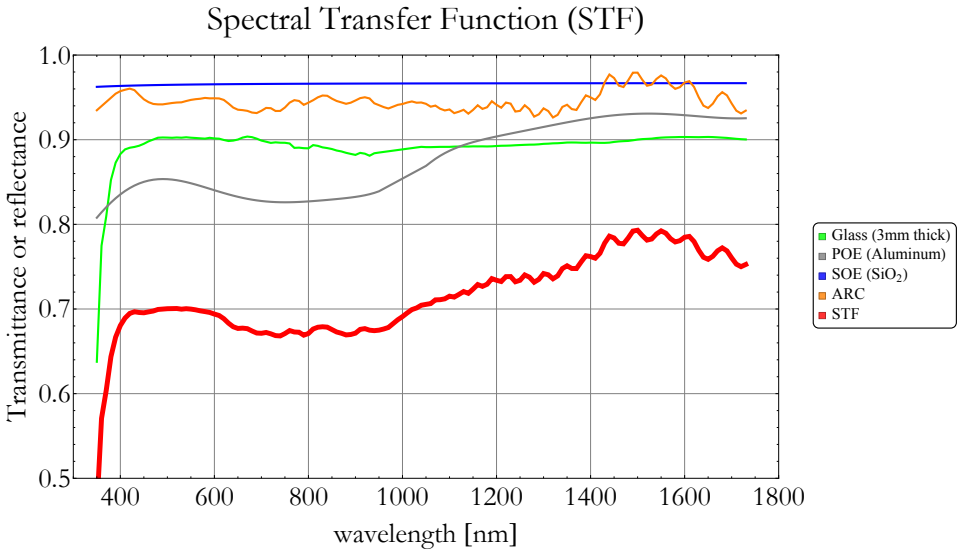

Figure 2.6: Spectral properties of TwinFocus® optical interfaces. The red line is the product of the other curves and represents the Spectral Transfer Function. The data concerning the front cover glass, the SOE and the ARC describe the situation of normal incidence, while the data concerning the POE refers to an incident angle of 30°.

ment. Several target parameters can be considered in order to evaluate the optimized result. Incidence angle distributions, power collected by the 3J cell, and irradiance uniformity on the target are the parameters that have been used to accept or reject the optimized solution. For what concerns the incidence angle distribution, according to Fresnel losses described in the equation (2.2), a maximum incidence of 50° on the SOE was allowed. ARC on the 3J cell allows higher incidence angles, up to 75°. These values are referred to Fresnel losses almost equal to a situation of normal incidence, while higher incidence angles cause unacceptable optical losses. The figures 2.7, 2.8, 2.9 represent the incidence angles distributions projected on the front cover glass. In this analysis were considered only light rays with a normal incidence on the glass. The angles distribution on the mirror ranges from a minimum of 23° to a maximum of 42°, and for this reason the reflectance curve reported in figure 2.6 was measured using an incidence angle of 30°. The angles distributions on the SOE and 3J cell are very important for the optical efficiency of the final optics. These data are represented, like the POE's map, projecting the angle values on the front cover glass. The data are also represented with two histograms in figure 2.10. As required by the physical constraint, all the incidence angles on the SOE and on the 3J cell are below, respectively, 50° and 75°.

After that the distributions of the incidence angles were studied a choice

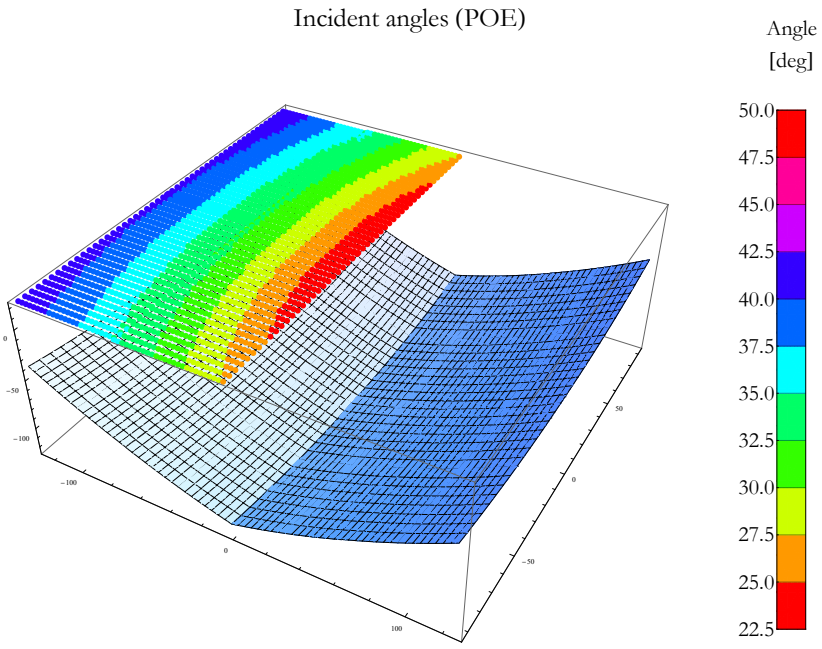

Figure 2.7: Map of the incidence angle on the POE, with a mean of 33°. The angles are projected on the front cover glass.

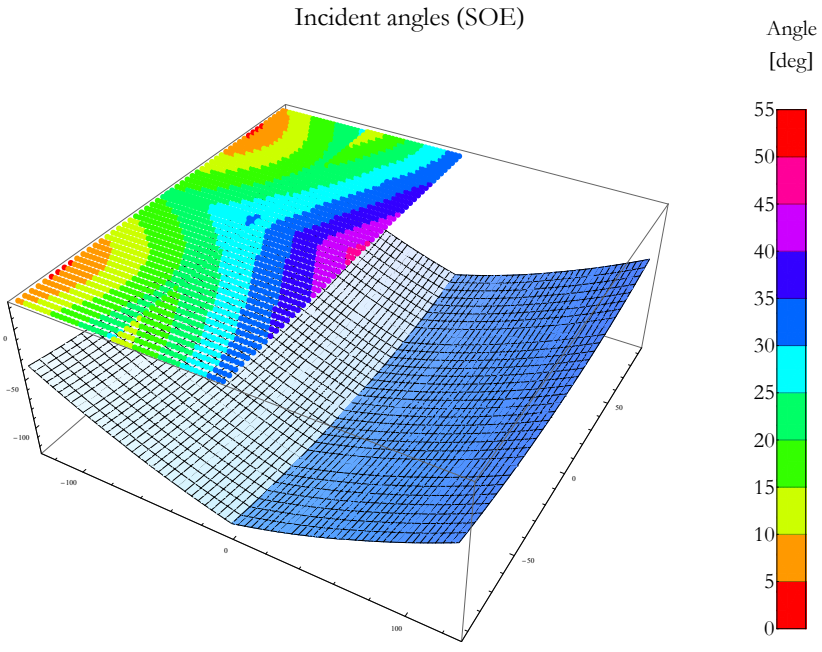

Figure 2.8: Map of the incidence angle on the SOE. The angles are projected on the front cover glass.

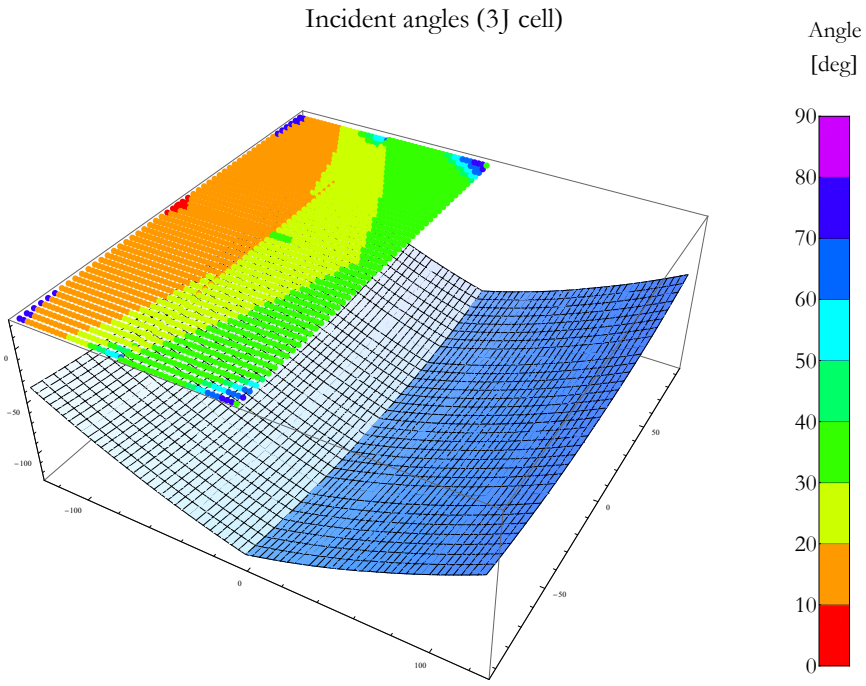

Figure 2.9: Map of the incidence angle on the 3J solar cell. The angles are projected on the front cover glass.

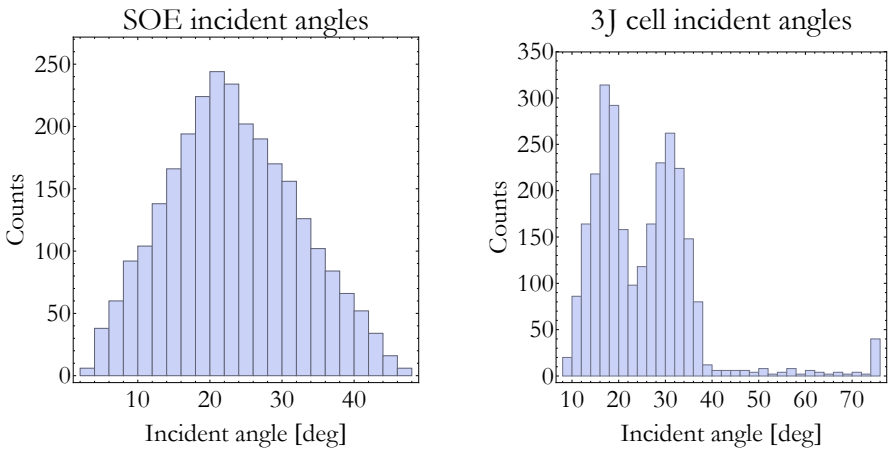

Figure 2.10: Histograms of the incident angles on the SOE (left) and on the 3J solar cell. In the first case the angles ranges from a minimum of 4° to a maximum of 47°, while in the latter the angles ranges from a minimum of 9° to a maximum of 75° The maximum values are within the physical constraints.

concerning the target binning was made. Discretization of the target has no effect on the total collected power (or equivalently the number of rays) but it can produce a loss of information of the irradiance profile shape. A low discretization level generates a smooth irradiance profile so it's not possible to identify local target areas having a high irradiance level. At the same time a high discretization level requires a large number of simulated rays in order to control the statistical noise on the target bins. More details on this topic can be found in the Appendix A. Several binning were chosen and for each choice a ray tracing simulation that produces a 1% statistical error on each pixel was performed. As a rule of thumb, a practical choice for the measure of the irradiance uniformity level is the peak-mean-ratio [67], that is the ratio between the highest and the mean irradiance values. It is intuitive that a high binning level corresponds to a more realistic evaluation of the peak-mean-ratio parameter. In figure 2.11 is reported the result of this analysis and a number of 55×55 bins (or pixels) was chosen to produce the final ray tracing reported in figure 2.12. This binning level was chosen basically for two reasons. First of all this value is high enough to produce a good evaluation of the uniformity parameter. Moreover the optical design workflow described in section 2.2 uses as a $5.3 \times 5.3\text{mm}^2$ target surface, while the actual 3J cell surface is $5.5 \times 5.5\text{mm}^2$, so the pixels on the 3J edges should be dark and the risk of underestimation of the irradiance level close to the edges of the cell is in this way limited. This binning level requires approximately a number of 30Mrays in order to have a 1% statistical noise on the number of collected rays by each pixel and, according to figure 2.5, a ray tracing simulation requires approximately $15'$.

Figure 2.12 shows the expected illumination profile over the 3J solar cell: the total incident power is 14.740W (so the mean irradiance is 48.6W/cm^2) and the peak irradiance is 66.3W/cm^2, so the peak-mean-ratio is 1.36. This result was obtained including in the ray tracing simulation all the spectral data: the source had a the standard spectral irradiance presented in figure 1.7 and the whole system had the STF presented in figure 2.6. Moreover the ray tracing included also the the angular divergence of the Sun rays: while the Sun has angular extension of $\pm 0.265^{\circ}$ the rays could hit the front cover glass with an incidence angle within this range. The mean incident irradiance can be used to calculate the real concentration ratio over the 3J cell, that is

$$C_{real} = \frac{48.6\text{W/cm}^2}{1 \text{ Sun}} = \frac{48.6\text{W/cm}^2}{0.09\text{W/cm}^2} = 540\times \tag{2.18}$$

where 1 Sun is the irradiance over the front cover glass. This result can be compared with the geometrical concentration factor defined in the equation (2.1) in order to calculate the integral optical efficiency

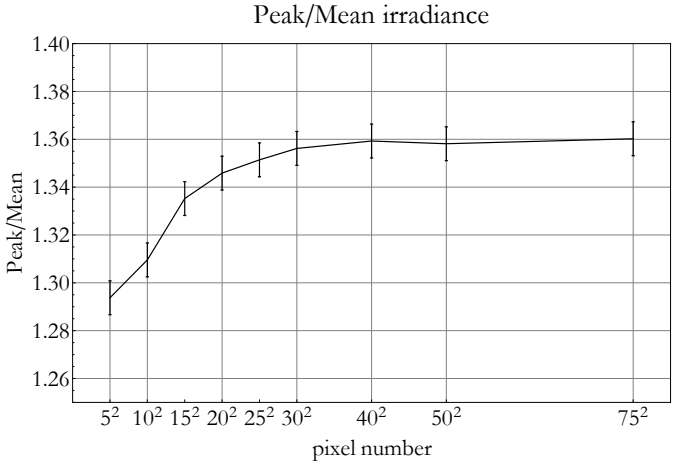

Figure 2.11: Comparison between the discretization level of the 3J solar cell with the estimation of the peak-mean-ratio parameter. In each ray tracing simulation the number of simulates rays produces a statistical error of 1% on the number of rays collected by each pixel.

$$\eta_{optics} = \frac{540\times}{783\times} = 69\% \tag{2.19}$$

which describes the percentage of the power that is transferred from the source to the target. This value is in some way related to the electrical current generated by the 3J solar cell, but its correct interpretation is valid only from an optical point of view: it's important to note that the 3J cell works on 3 different spectral ranges (as explained in figure 1.6) and that the current generated by the 3J cell is the lowest between the current generated by the three sub-junctions. To correctly translate the optical efficiency into electrical performance of the system it is necessary to consider the External Quantum Efficiency (EQE) curves. The topic of the electrical performance of the CPV system is largely developed in chapter 5. For what concerns the irradiance uniformity, in literature there are several papers that discuss how different irradiance profiles affect the solar cell electrical performance, and according to ref. [67] a peak-mean-ratio of 1.36 decrease the Fill Factor (FF) by less than 1% respect to a uniform profile. More details about the performance of TwinFocus® optics under various conditions are discussed in the chapter devoted to the tolerance analysis.

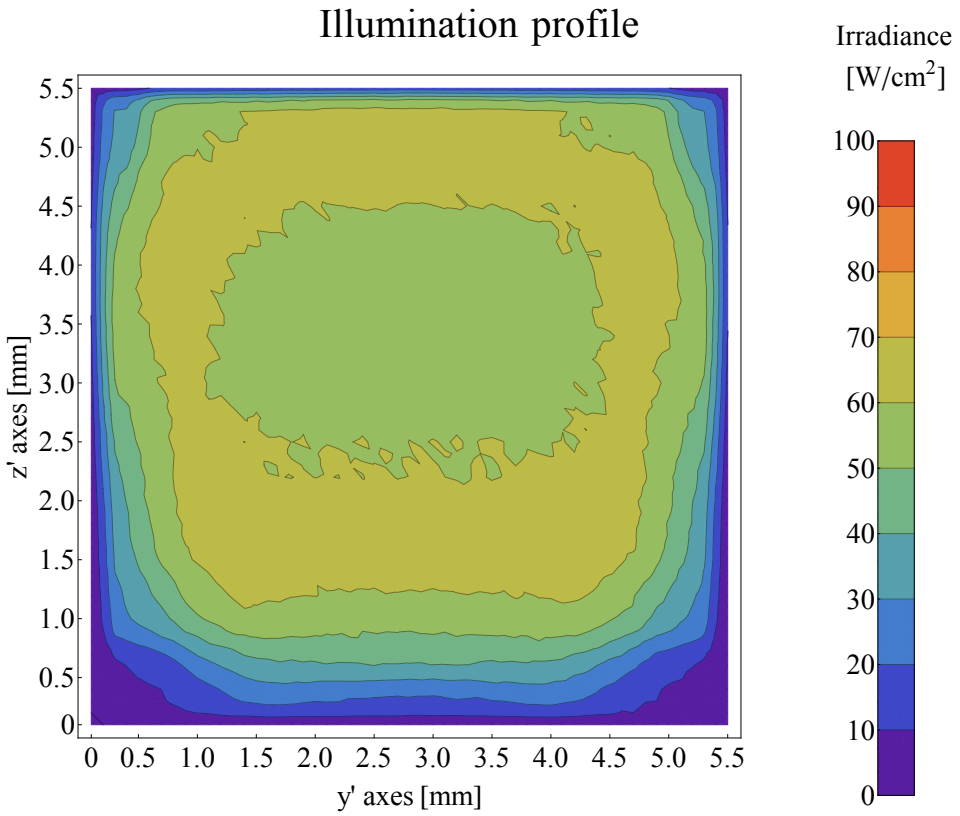

Figure 2.12: Distribution of the irradiance over the 3J solar cell. The power incident on the 3J cell is 14.740W and the peak irradiance is 66.3W/cm^2, so the peak-mean-ratio is 1.36. This map has been obtained with a detector made by 55×55 pixel that collects $2.5 \cdot 10^7$ rays so, according to Appendix A, the error on the irradiance of each pixel is 1%.

Chapter 3

Manufacturing the optical elements

In this chapter the manufacturing processes of the Primary Optical Element (POE) and the Secondary Optical Element (SOE) are described. Much effort was spent in the realization of the POE because it greatly influences the performance of the optical system. For this purpose a screening experiment was performed in order to identify the most important parameters of the injection molding process.

Manufacturing a prototype is a fundamental step during the design of a new product. This step requires a previous know-how concerning the production processes, but its importance comes from the new knowledge that can be learnt during prototyping. The interaction with manufacturers is fundamental in order to effectively understand strengths and limits of the technologies involved. POE and SOE depend both on an injection molding process, but the optical element that strongly affects the optical efficiency is the first one. For this reason great attention was given particularly for the production of the POE.

3.1 Manufacturing the POE

POE is a polycarbonate (PC) substrate made through an injection molding process that is then aluminized with a Physical Vapor Deposition (PVD). During the PVD process the POE is also protected with a SiO_2 coating. Nowadays this is the mainstream technology particularly for the production of automotive headlamps and street lamps. There are basically two important aspects during the realization of the POE: the molding process and the PVD process. In this thesis great care was given particularly to the first aspect.

Parameter	Optimal value
Melt temperature, $\mathbf{T_{melt}}$	280-300 °C
Mold temperature, $\mathbf{T_{mold}}$, $\mathbf{T_{core}}$	60-110 °C
Injection speed, $\mathbf{v_{fill}}$	moderate-fast
Hold pressure, $\mathbf{P_{hold}}$	70-110 bar
Hold time, $\mathbf{t_{hold}}$	depends by the process

Table 3.1: Optimal parameters for the injection molding of polycarbonate Makrolon 2407

3.1.1 Injection molding process

The idea behind injection molding technology is really simple, but the process itself involves a large number of parameters and requires a good experience. For these reasons it is not easy to produce a satisfactory product. Figure 3.1 represents a molding process scheme. A hopper collects the "feed" of the process (i.e. the plastic granules, for example polycarbonate) and then the granules are grinded with a screw. Meanwhile some resistive heaters heat up the plastic until it is melted. The screw then forces the melted plastic into a nozzle and injects it into the mold. The mold is usually a steel tool composed by two (or more) parts: as shown in figure 3.1 the two main components are the the mold cavity and the mold core. The sequence of events during the injection mold of a plastic part is called the injection molding cycle. The cycle begins when the mold closes, followed by the injection of the polymer into the mold cavity. Once the cavity is filled, a holding pressure is maintained to compensate for material shrinkage. In the next step, the screw turns, feeding the next shot to the front screw. This causes the screw to retract as the next shot is prepared. Once the part is sufficiently cool, the mold opens and the part is ejected [68]. Figure 3.2 shows the mold used for the production of the POEs.
According to the experience of the mold manufacturer a specific type of polycarbonate was chosen. More exactly the *Makrolon 2407* is the polycarbonate chosen because of its mechanical and finishing properties. The table 3.1 summarizes the most appropriate parameters for *Makrolon 2407* suggested by the PC vendor and by the mold manufacturer. These parameters can influence the shape of the POE (i.e. the optical efficiency) so a screening experiment is mandatory in order to understand and to handle the injection molding process. Before that the screening experiment is faced it is necessary to develop a strategy to measure and reconstruct the POE.

3.1.2 Measure and reconstruction of the POE

A Coordinate Measuring Machine (CMM) was used to measure the POE surfaces. It is shown in operation in figure 3.3. The output of such instru-

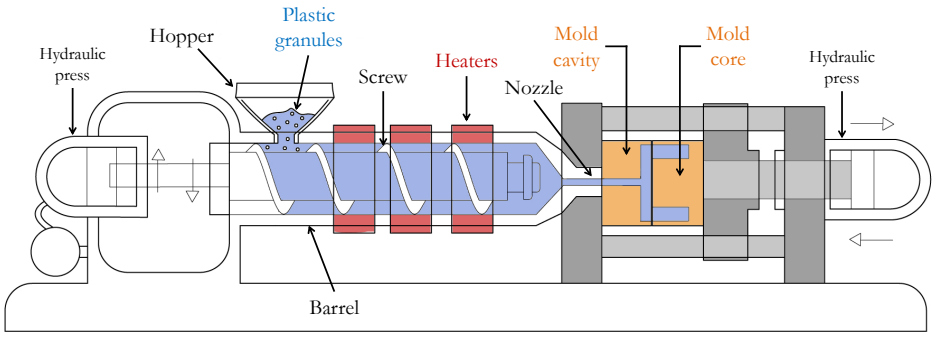

Figure 3.1: Scheme of the injection molding process. After that the plastic granules are grinded and melted, the polymer is injected into a steel cavity and then solidifies into a shape that has conformed to the contour of the mold.

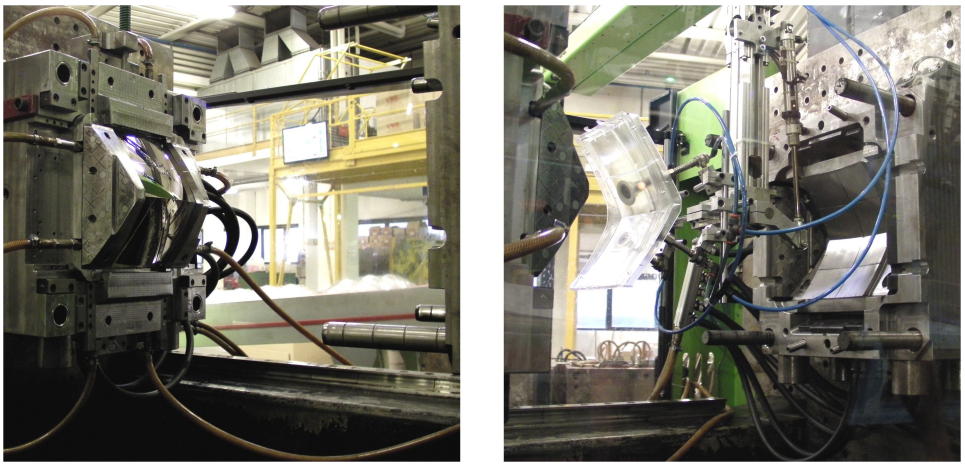

Figure 3.2: Picture of the mold used for the production of the POEs. On the left is shown the mold core while on the right is shown the mold cavity. On the right is it also possible to see the POE immediately after a production cycle.

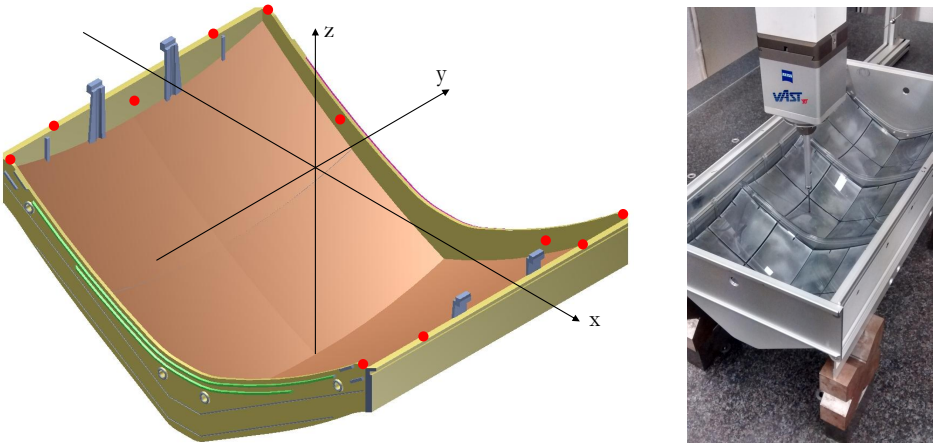

Figure 3.3: Left: a POE is shown. The red dots represent the reference points that the CMM used for the alignment process. Right: CMM in operation.

ment is a point cloud composed by approximately 24500 points for each POE representing the actual coordinates of the POE surfaces. These coordinates were then compared to the ideal ones. Figure 3.4 shows the error along the z axis between the actual and the ideal surfaces. After that the point cloud was collected, a 3^{rd} order polynomial fit was used to interpolate each one of the eight POE surfaces, so a single concentrator was reconstructed through eight 3^{rd} order polynomial equations. These equations were then imported in the ray tracing software and the actual POE was reconstructed. The subsequent ray tracing simulation gave the expected irradiance profiles on the two 3J solar cells. Figure 3.5 shows the CMM data and the ray tracing results of a POE that was made with these molding parameters: T_{melt} = 290 °C, $T_{mold} = T_{core}$ = 90 °C, v_{fill} = 25mm/s, P_{hold} = 110 bar, t_{hold} = 20s, t_{cycle} = 65s. The simulation result is that the power collected by the two solar cells is 13.74W, so a lack of 7% respect to the ideal 14.74W is expected. The power collected by the 3J cell is in some way related to the electrical power generated by the 3J cell itself, so a lack between the electrical power generated by the ideal and the tested optics is expected. This topic will be discussed in chapter 5.

3.1.3 Screening experiment of the injection molding process

A better comprehension of the injection molding process was mandatory after the results shown in figures 3.4 and 3.5. According to ref. [69] a statistical approach in Designing an Experiment (DOE) was used. Before that the experiment was performed the most appropriate parameters must be chosen. In this step the manufacturer's experience played a fundamental

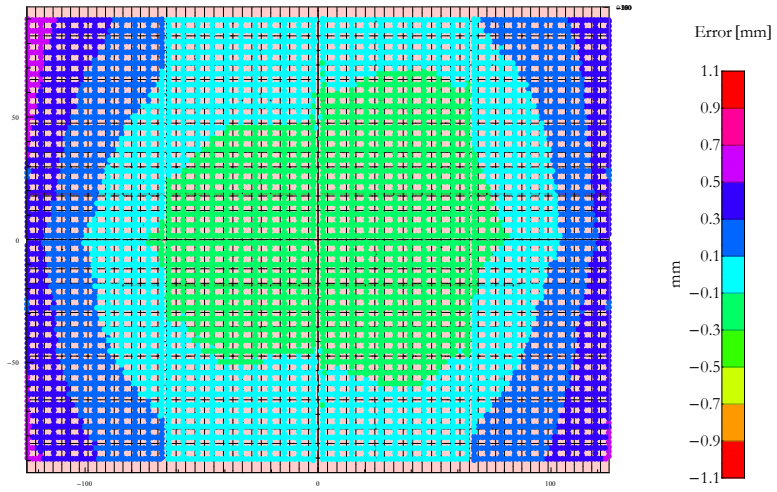

Figure 3.4: Top view of a POE measured with a CMM. The points represent the difference between the ideal and the actual POE surfaces along the z axis (perpendicular to this sheet).

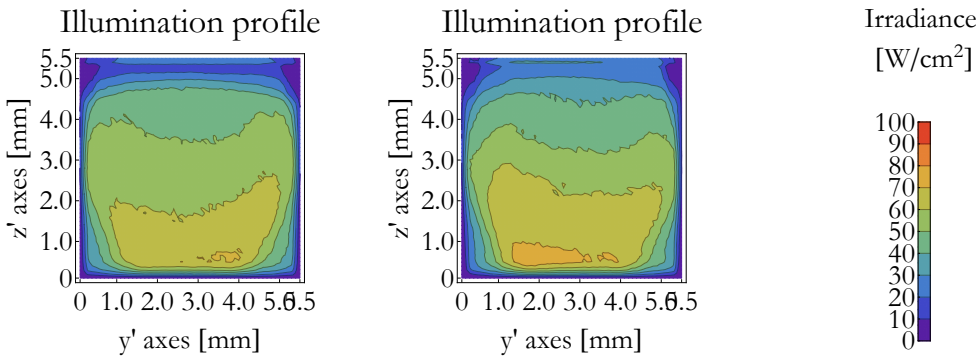

Figure 3.5: Irradiance profiles expected on the 3J solar cells of the concentrator represented in figure 3.4. In both cases the expected collected power is 13.74W. The most important injection molding parameters used in this case are $T_{melt} = 290℃$, $T_{mold} = T_{core} = 90℃$, $v_{fill} = 25mm/s$, $P_{hold} = 110bar$, $t_{hold} = 20s$. The cycle time is 65s.

role in order to reduce the number of guesses and the trial and error tests, so to focus the attention to the most important parameters. The following list is the scheme adopted for the screening experiment described in this section

- Statement of the problem: a discrepancy between the expected and the real POE exists;
- Selection of the response variables: the power collected by the 3J solar cell after the reconstruction of the POE surfaces;
- Choice of the factors and ranges: factors listed in table 3.1;
- Choice of experimental design: screening experiment;
- Statistical analysis and conclusions.

The factors listed in table 3.1 are six, that are too many to perform a complete 2^6 screening experiment. Moreover the mold and the cavity temperatures are factors that require a long time to be changed due to the high thermal capacity and low thermal conductivity of the steel mold. This means that if these parameters are introduced in the screening experiment a long time is required to properly set them and to perform the whole experiment. For these reasons a short pre-screening experiment was performed in order to understand if the mold temperature could affect the POE shape. According to table 3.1 a typical mold temperature is in the range $60-110$℃, so several POEs were manufactured at different mold temperatures. As already described in section 3.1.2, these POEs were then measured with a CMM and the optical surfaces reconstructed. The results of the ray tracing simulation are summarized in the next table

	110℃	70℃	60℃	50℃
Power 3J	14.24W	14.01W	14.11W	14.08W

Table 3.2: Power collected by the 3J cell for different mold temperatures. $P = (14.11 \pm 0.10)$ W. In the ray tracing simulation the number of simulated rays is $40 \cdot 10^6$ with a 2×2 source, so the statistical error of the power value is $4 \cdot 10^{-3}$W. More details can be found in Appendix A.

The power collected by the 3J cell is P = (14.11 ± 0.10) W, so the percentage variation is less than 1%. During this experiment all the other parameters were maintained to constant values: T_{melt} = 290 °C, T_{core} = 90 °C, v_{fill} = 25mm/s, P_{hold} = 80 bar, t_{hold} = 20s, t_{cycle} = 65s. In order to test if the mold temperature has a significant effect on the power collected by the 3J cell a statistical test was performed. The null hypothesis H_0 says that all the power presented in table 3.2 belong to the same normal distribution. More formally

$$\begin{aligned} &H_0 : \mu_i = \mu \\ &H_1 : \text{at least one } \mu_i \text{ is different to } \mu \end{aligned} \tag{3.1}$$

where μ_i are the power values presented in table 3.2 and μ is the average power of the normal distribution. H_1 is called alternative hypothesis. The hypothesis were tested through a χ^2 test and the result is $\chi^2_3 = 2.8 \cdot 10^5$, which means that the null hypothesis is rejected with a significance level lower than 0.001. In other words, the mold temperature has an effect on the POE shape but, because the percentage variation of the power collected is less than 1%, this effect is small so it is better to investigate it after the identification of parameters with larger effects. According to this result, the mold temperature chosen for the subsequent screening experiment was the most typical value for the polycarbonate in use, that is 90 ℃.

After that this pre-screening investigation was concluded, three molding parameters where identified as the most appropriate to perform a complete 2^3 screening experiment. The information of the experimental planning are summarized in the cause-and-effect (or fishbone) diagram is shown in figure 3.6. The chosen parameters are the hold pressure, the hold time, and the fill speed, while the constant factors during the molding process are the melt temperature (290 ℃), the core and mold temperature (both 90 ℃), the polycarbonate (Makrolon 2407) and the operator. Cycle time was not modified because it is directly related to the production cost and 65s was chosen as an acceptable value.

	A	B	C
level	P_{hold}[bar]	t_{hold} [s]	v_{fill} [mm/s]
High (+)	90	30	35
Low (-)	70	10	15

Table 3.3: Parameters and levels of the screening experiment.

The eight samples were randomized and table 3.4 shows in which order they were realized. The reconstruction of the eight POEs gave the values reported in figure 3.7. A regression model with two factors interaction was then applied

$$\begin{aligned} y =& \beta_0 + \beta_A x_A + \beta_B x_B + \beta_C x_C + \\ &+ \beta_{AB} x_{AB} + \beta_{AC} x_{AC} + \beta_{BC} x_{BC} + \epsilon \end{aligned} \tag{3.2}$$

where β_0 is the average of all the observations, β_i ($i = A, B, C, AB, AC, BC$) are the parameters of the regression model, x_i represents the level of each

parameter (its value could be +1, high, or −1, low), and ϵ is a random error term also called residual term. Variables x_{AB}, x_{AC}, x_{BC} represent the interaction between the three factors. The effect of a factor is defined as the change in response produced by a change in the level of the factor. The levels are called "high" and "low" and they are associated to a "+" and a "−" sign, respectively. The main effect of factor A is, for example, the difference between the average response at the high level and the average response at the low level of A. The effect of factor A and the corresponding regression coefficient are then

$$\begin{aligned} A &= \left(\frac{13.89 + 13.84 + 13.79 + 13.77}{4}\right) + \\ &+ \left(\frac{14.52 + 14.49 + 14.47 + 14.49}{4}\right) = -0.67 \\ \text{and} \qquad \beta_A &= \frac{A}{2} = \frac{-0.67}{2} \end{aligned} \tag{3.3}$$

In the same way is it possible to calculate all the factor effects and the regression coefficients and the results are summarized in table 3.5. This result required an analysis particularly through a hypothesis testing. The analysis of the data presented in figure 3.7 consisted in testing the influence of the factors A, B, C, AB, AC, CB on the power collected by the 3J cell. More formally the null and the alternative hypothesis are

$$\begin{aligned} &H_0 : \beta_A = \beta_B = \beta_C = \beta_{AB} = \beta_{AB} = \beta_{BC} = 0 \\ &H_1 : \text{at least one } \beta_i \neq 0 \end{aligned} \tag{3.4}$$

At this point is was necessary to choose a level at which the null hypothesis is rejected or not. The $\alpha-$value, or level of significance, was set to 0.05

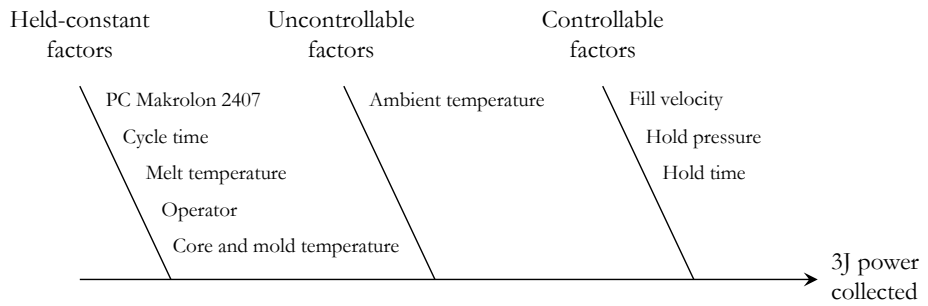

Figure 3.6: Cause-and-effect, or fishbone, diagram of the 2^3 screening experiment. This diagram represents which factors modify the the power collected by the 3J solar cell.

num	A	B	C
1	-	-	+
2	+	+	-
3	+	-	-
4	-	+	+
5	+	-	+
6	-	+	-
7	+	+	+
8	-	-	-

Table 3.4: Parameters and levels of the screening experiment listed in the chronological order as each test was performed.

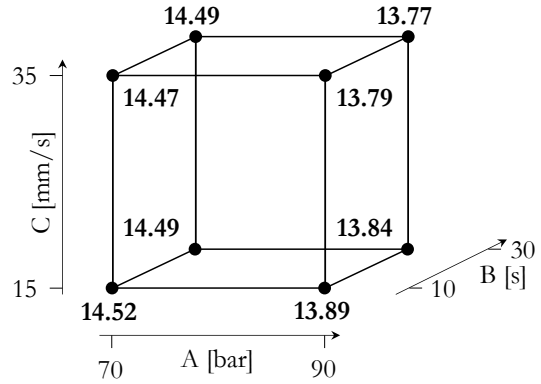

Figure 3.7: Power collected by the 3J solar cell in the eight situations of the 2^3 screening experiment.

and a P-value approach was adopted. The P-value is the smallest level of significance that would lead to rejection of the null hypothesis H_0. More details on its definition can be found in ref. [69]. The result of the analysis is shown in figure 3.8 and in table 3.6: the only factor that is significantly different form zero at a confidence level of 95.0% is the hold pressure. More exactly the A value reported in table 3.5 is negative so the lower the hold pressure the higher the power collected by the 3J cell. Neglecting all the terms that are statistically zero, the model presented in equation (3.2) can be simply rewritten

$$y = 14.1575 - \frac{0.67}{2} x_A + \epsilon \tag{3.5}$$

so the regression model is linear respect to the hold pressure factor. In the P-value approach adopted it was made the assumption that the eight samples were randomized and that they came from independent populations that could be described with a normal distribution. This assumption was checked using the normal probability plot represented in figure 3.9. It is important to note that the y axis was arranged so that if the hypothesized distribution adequately describes the data, the plotted points fall approximately along a straight line.

The conclusion of this experiment is that the lower the hold pressure the higher the power collected by the 3J solar cell. This is unfortunately in contrast with the optimal hold pressure for polycarbonate: PC requires indeed a high hold pressure in order to guarantee optimal mechanical properties. In this situation the choices are different: accept the optical losses (only if the optics is still cost effective) or modify the mold in order to correct the POE wrong shape. This second option could be faced in two different ways:

model term	effect estimate
average, β_0	14.1575
A	-0.67
B	-0.020
C	-0.055
AB	-0.015
AC	-0.030
BC	0.020

Table 3.5: Estimated effects on the power collected by the 3J cell. Each effect is also related to the corresponding coefficient of the regression model.

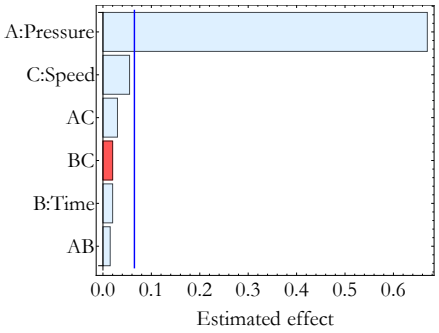

Figure 3.8: Effect of each factor. The blue line represents the 0.05 significance level: the only factor that has a probability greater than 5% to influence the power collected by the 3J is A.

Source	sum of squares	dof	P-value
A:P_{hold}	0.8978	1	0.0048
B:t_{hold}	0.0008	1	0.1560
C:v_{fill}	0.00605	1	0.0577
AB	0.00045	1	0.2048
AC	0.0018	1	0.1051
BC	0.0008	1	0.1560
Total error	0.90775	7	

Table 3.6: Analysis of variance for power. Only the source A has a P-value that is less than 0.05, indicating that it is significantly different from zero at the 95.0% confidence level.

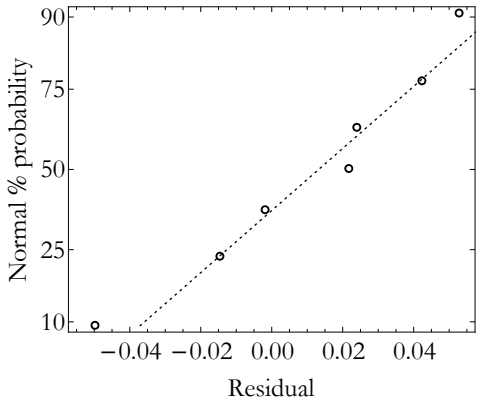

Figure 3.9: Normal probability plot of the residuals. Arranging the y axis the points fall approximately along a straight line, so the independence assumption had been checked.

modifying the POE optical surfaces or modifying the POE frame (i.e. the back side of the POE) in order to change its mechanical properties. The best choice seems the last one, but as things stand at the conclusion of this PhD work, a solution was not been yet found.

3.2 Manufacturing the SOE

In section 2.1 the technological and mechanical constraints concerning the SOE were described. These constraints are both related to the process adopted to manufacture this optical element. In the next section the production process of the SOE is described and in particular the constraints introduced are highlighted.

3.2.1 SiVARA™Sol-Gel process

Unlike the POE, the SOE shape doesn't heavily affect the optical efficiency of the system, particularly when the optics is perfectly aligned. This statement is due to a couple of considerations. First of all equation (1.9) states that slope errors of a refractive surface are less critical with respect to slope errors of a reflective surface. Moreover the optical path length between the POE and the SOE cell is about twenty times larger than the optical path length between the SOE's entrance aperture and the 3J cell. These two considerations make the SOE entrance surface more tolerant to geometrical imperfections respect to the POE reflective surfaces. This is the reason why the injection molding process of the SOE has not been deeply studied as

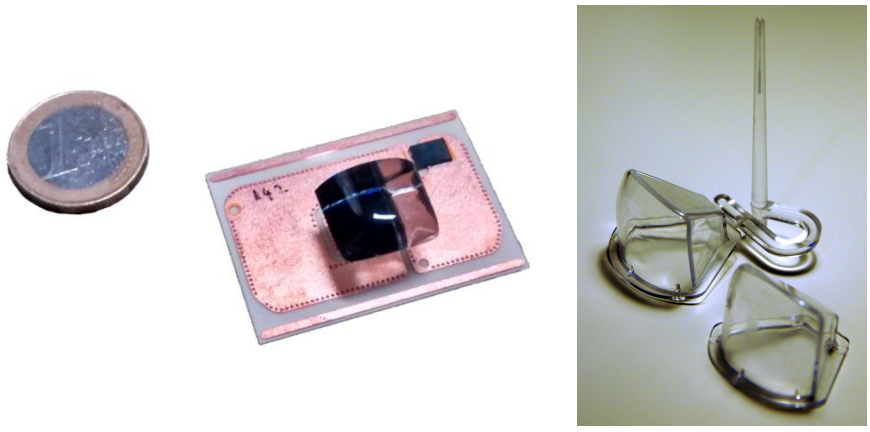

Figure 3.10: Left: complete receiver including the 3J solar cell and the SOE glued on it. Right: picture of the PC vessel that is used for the manufacture of the SOE. The inner volume of the PC vessel is eight times the volume of the fused silica SOE.

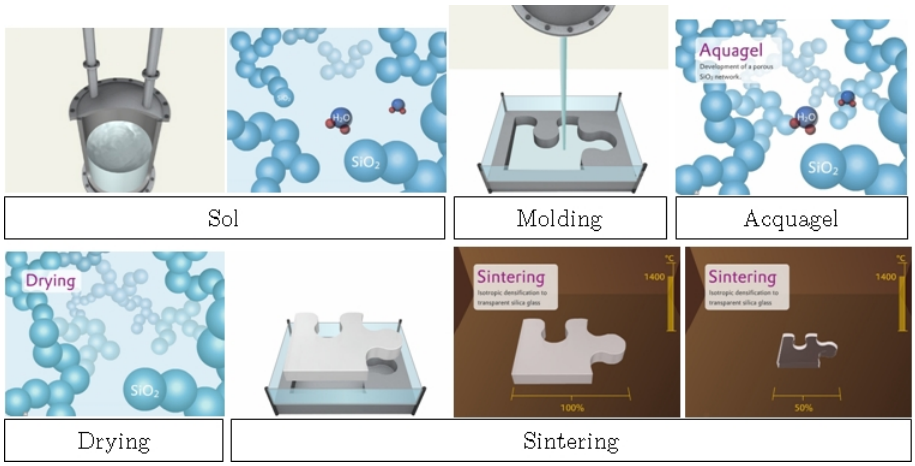

Figure 3.11: Key steps during the production process of the SOE. More details can be found at `www.savosil.com`

indeed was made for the POE. As for the POE, the production of the SOE begins with the injection molding of a PC component. This component in shown in figure 3.10 and it's inner volume is exactly eight (2^3) times the volume of the desired SOE. The name of the subsequent process is called SiVARA ™Sol-Gel and this is a proprietary process which owner is the company Evonik. The glass resulting from the process is called SAVOSIL ™. The first step consists in realize the *sol*, a mix of water, DYNASYLAN® (SiH_4) and AEROSIL®. The latter component is in particular the most important in the whole process because it is composed by SiO_2 nanoparticles suspended into a solvent. This chemical compound is thixotropic, which means that it becomes viscous in static conditions. The *sol* is then poured in the polycarbonate vessel and it dries releasing the water molecules in the air. During this process the compound becomes a gel (more exactly ACQUAGEL®) made by an amorphous structure of silicon bi-oxide. The resulting object is then extracted from the polycarbonate vessel and maintained into heating chamber at 1400 ℃. During this process the gel compound becomes SiO_2 glass (SiO_2 has a glass transition at 1150 ℃) and it shrinks its length along each direction by 50%. The final optical element is 99.99% made by SiO_2, the accuracy along each direction is less than 1/1000 the object length and its roughness is in the range $15 - 50$nm. The great potential of this technology in nonimaging (as well as imaging) optics is the freedom in the design and production of freeform surfaces. The producer of SAVOSIL ™does not declare a maximum volume for the optical components: the volume has an impact only in the time required for the drying process. Even if with SiVARA ™Sol-Gel process it is possible to create freeform surfaces, it introduces a mechanical constraint that consists in the ability of the optical component to be extracted from the vessel in which the *sol* has been poured.

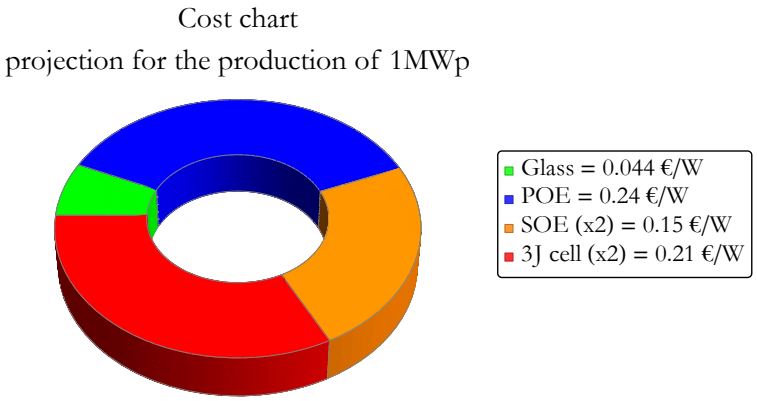

Figure 3.12: Chart representing the impact of each optical component to the final cost. Optical glue is not included because it has a negligible weight. The optical components, including the 3J cell, have an impact on TwinFocus® system cost of about 0.64€/W.

More details on the shape of the SOE can be found in Appendix B.

3.3 Cost analysis

A detailed cost analysis is here not discussed, but some data are given. In chapter 5 will be discussed the expected electrical power generated by a TwinFocus® concentrator, that is approximately $10.5W$ in standard operating conditions (which means that the system is operating under reference solar spectrum ASTM G173-03 and with the 3J cell at 40 °C above air temperature). A short-term projection of TwinFocus® optics cost, including glass cover, POE with metallization and protection, two SOEs, optical glue, and two 3J cells is 6.76€/concentrator. This projection has been made in the hypothesis of producing 1MWp, considering current market prices and without including the effect of any learning curve. In this calculation no additional equipping or manufacturing costs are included. In conclusion the optical components, including the 3J solar cells, have an impact on TwinFocus® system cost of about 0.64€/W. Considering the current PV market status, as of today a complete CPV system does have to get the goal of 2€/W in order to be cost-effective [70].

Chapter 4

Tolerance analysis of TwinFocus optics

A good understanding of the tolerances of an optical system is essential before its realization, even though nonimaging optics are more tolerant than imaging ones. In this chapter a tolerance analysis of TwinFocus® optics presented in the previous chapters is performed from several points of view. The goal is to estimate the power collected by the 3J cell in various conditions and to identify criticalities.

Tolerance analysis requires on-field experience about the processes and the technology involved during manufacturing. The nonimaging optics previously described uses customized solution: knowledge about tolerances cannot be found in literature so experience concerning TwinFocus® optical scheme must be built. According to [45] the errors that can occur in nonimaging optical systems are:

- **System**: this kind of errors vary from one optics to another, such as relative position and tilting angles between the optical components. These errors are tipically described through a normal distribution.
- **Gross**: these errors are due to fabrication blunders. They introduce errors such as systematic shifts or misalignments.
- **Process**: these errors occur during the production process. For example during an injection molding process the errors that can occur are warping, sinking, and rippling. These errors can be limited setting the appropriate process parameters.
- **Roughness**: arise from the inability to perfectly polish an optical surface.

The analysis concerning TwinFocus® optics was conducted considering various real conditions such as misalignment of the whole system, assembling imperfections, and deformation of the POE due to temperature changes. System and process errors were in particular investigated.

4.1 Angular acceptance

The first tolerance investigated was the situation in which all the optical components are properly manufactured and assembled, while the whole system is misaligned with respect to the incoming sunlight. This is a pure system error. For this purpose a quantity called *acceptance angle* is commonly used in nonimaging optics literature. This parameter is defined as the tilting angle at which the optical system performance is 90% of the maximum. According to ref. [71] a method to classify the quality of the concentrator optics is the Concentration-Acceptance Product (CAP) factor, which is defined as follows

$$CAP = sin\theta\sqrt{C_g} \leq n_{glue} \tag{4.1}$$

where θ is the acceptance angle, C_g is the geometrical concentration factor defined in equation (2.1), and n_{glue} is the refractive index of the medium in which the 3J cell is immersed. This equation states that for TwinFocus® optics the maximum achievable CAP factor is n_{glue} (that is approximately 1.46 at a wavelength of 500 nm). Acceptance angle was used at the beginning of the design process as a target constraint: a requirement for TwinFocus® optics was to guarantee an acceptance angle of $\pm 1^{o}$ for misalignment around x and y axes. According to equation (4.1) this value is a typical choice for nonimaging optics with concentration factor close to $1000\times$.
Because of its asymmetric shape TwinFocus® optics must be studied tilting the whole system around both x and y axes. Figure 4.1 represents the result of this study: the ray tracing simulations of the whole system in various tilted positions indicate that TwinFocus® optics has an acceptance angle that ranges from $\pm 0.85^{o}$ around x axis to $+1.05^{o}/-1.35^{o}$ around y axis. As a result the CAP factor is

$$0.41 \leq CAP \leq 0.65 \tag{4.2}$$

that is a competitive result respect to the state-of-the-art high concentration nonimaging optics for CPV [72] which have CAP factors in the range $0.6 - 0.8$. Figure 4.2 shows more details about TwinFocus® optics behavior in different tilted conditions. More details about the electrical power generated by the 3J solar cell under non-uniform irradiance profile can be found in chapter 5.

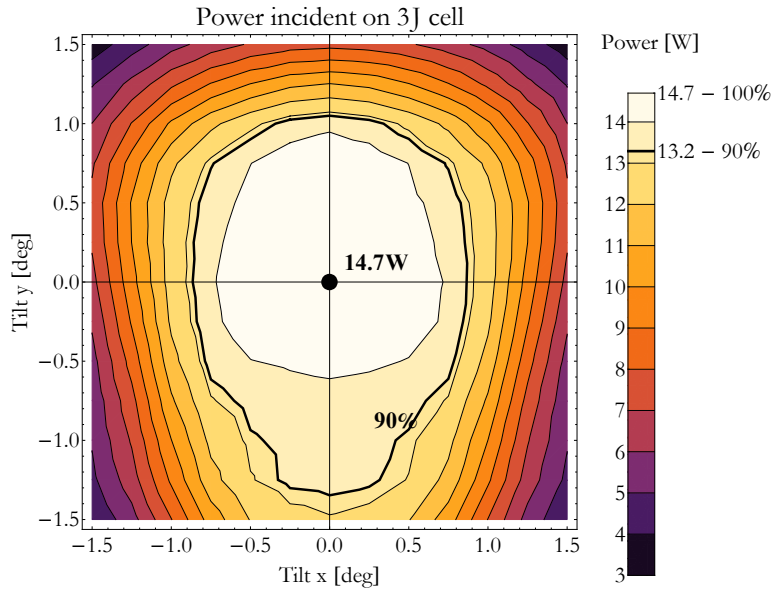

Figure 4.1: Power collected by the 3J cell tilting all the system around x and y axes. Orientation of the axes is defined figure 4.3. The acceptance angles range from a minimum of $\pm 0.85^{o}$ for x axes to a maximum of $+1.35^{o}/-1.05^{o}$ for y axes.

4.2 Optical elements assembling errors

During the assembling of a TwinFocus® module the optical components could be not in their nominal positions. Uncertainties concerning their relative positions introduce variability in the power collected by the 3J solar cell (i.e. in the expected system short circuit current and electrical power). The next sections give an overview on the mechanical connections between the optical components followed by a Monte Carlo tolerance analysis.

4.2.1 Details on the mechanics of the optics

As shown in figure 4.3 TwinFocus® system is made by several components. For the subsequent analysis the most important are: a POE connected to an aluminum heat sink, a receiver connected to the POE and to the heat sink, a 3J solar cell that is soldered on the receiver, and a SOE that is glued on the 3J cell. Two reference systems were introduced: the first one (x, y, z) has the xy plane parallel to the front cover glass and the origin in the middle of the POE, while the second (x', y', z') has the same axes orientation but the origin in the center of the 3J solar cell. The analysis started from the measure of the position error of each optical component. In a first stage a limited number of POEs and SOEs were built and their tolerance analysis

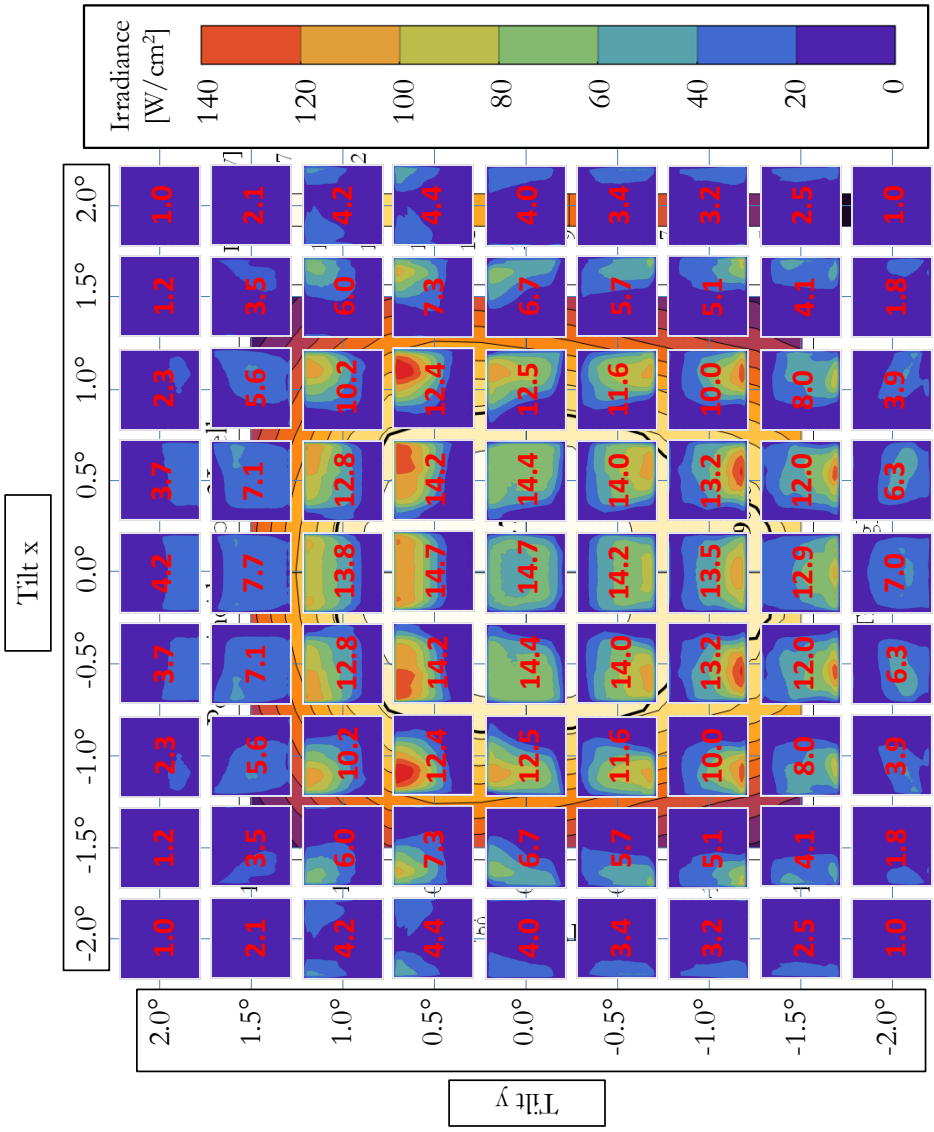

Figure 4.2: In the background is it possible to see the power map presented in figure 4.1. Over this map the irradiance profiles at various system tilting angles are shown. The red number over each irradiance profile indicates the power collected by the 3J solar cell in that tilted condition.

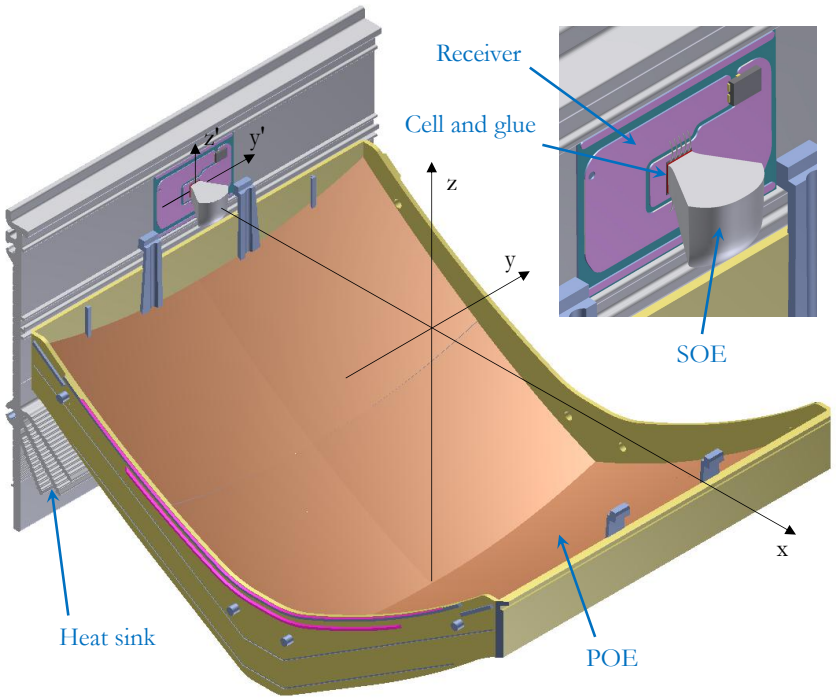

Figure 4.3: The figure represents an overview of the TwinFocus® optics with a small zoom in the upper right concerning the receiver. The average sunrays direction is along z axis. Front cover glass is not shown.

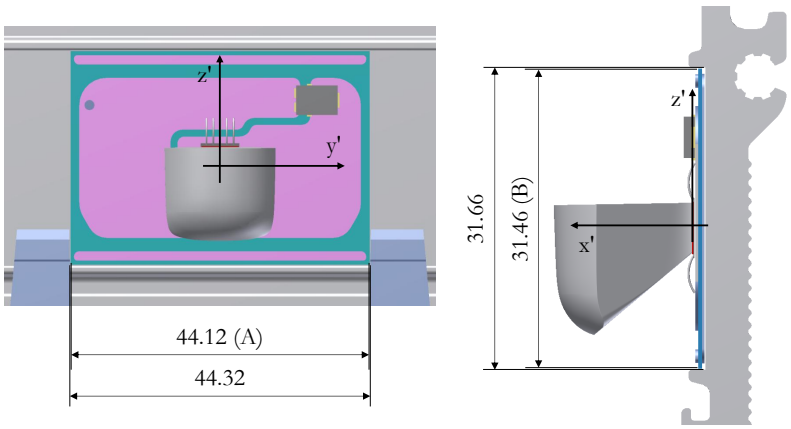

Figure 4.4: The figure represents receiver in its lodge: its position along x' and z' axes is guaranteed by the aluminum heat sink while the position along y' axes is guaranteed by the POE. The 3J solar cell is soldered on the receiver and the SOE is glued on the 3J cell.

Component	Parameter	Measure
receiver	Length (A)	(44.150 ± 0.030) mm
	Width (B)	(31.504 ± 0.027) mm
	y' position	-0.10 mm or $+0.10$ mm
	z' position	-0.10 mm
3J cell	$\delta y'_{3Jcell}$	(-0.063 ± 0.041) mm
	$\delta z'_{3Jcell}$	$(+0.024 \pm 0.033)$ mm
	θ_{3Jcell}	$(-0.04 \pm 0.29)^{\circ}$
SOE	$\delta y'_{SOE}$	(-0.057 ± 0.031) mm
	$\delta z'_{SOE}$	$(+0.002 \pm 0.042)$ mm
	θ_{SOE}	$(-0.025^{\circ} \pm 0.246^{\circ})$
POE	θ_x^{POE}	$(-0.001^{\circ} \pm 0.022^{\circ})$
	θ_y^{POE}	$(+0.016^{\circ} \pm 0.026^{\circ})$

Table 4.1: Tolerance distributions obtained from the measurement of 50 complete receivers and 2 complete TwinFocus® modules. The definition of the reference system is shown in figures 4.3 and 4.4.

provided a little database on which the subsequent tolerance study was performed.
As shown in figure 4.4 the receiver has an area ($44.12 \times 31.46\text{mm}^2$) that is smaller than the area in which it is lodged ($44.32 \times 31.66\text{mm}^2$). It was measured that during the assembling process the receiver has always one side in contact with the heat sink and another side in contact with the POE. More exactly the receiver has always an offset of -0.01mm along z' axes and could have along y' axes an offset of -0.01mm or $+0.01$mm with the same probability. Table 4.1 summarizes the tolerance measures concerning the optical components. Excluding the receiver position, which has already been discussed, the other measures are described using an average and a standard deviation value. It was chosen that these values describe various normal distributions.

4.2.2 Monte Carlo tolerance analysis

The data included in table 4.1 were included in the ray tracing software through a macro written in the ray tracing software programming language and a Monte Carlo analysis was performed. Each ray tracing simulation was made shooting 1'000'000 rays and using a 2×2 source so, according to Appendix A, the statistic error of each simulation is 0.026W [1]. In the hypothesis that the errors introduced during the ray tracing and the Monte Carlo simulations are both gaussian, their statistics combine in this way

[1] According to figure 2.12 and to Appendix A the average power collected in ideal conditions is $14.740\text{W} \pm 0.18\% = (14.740 \pm 0.026)$ W.

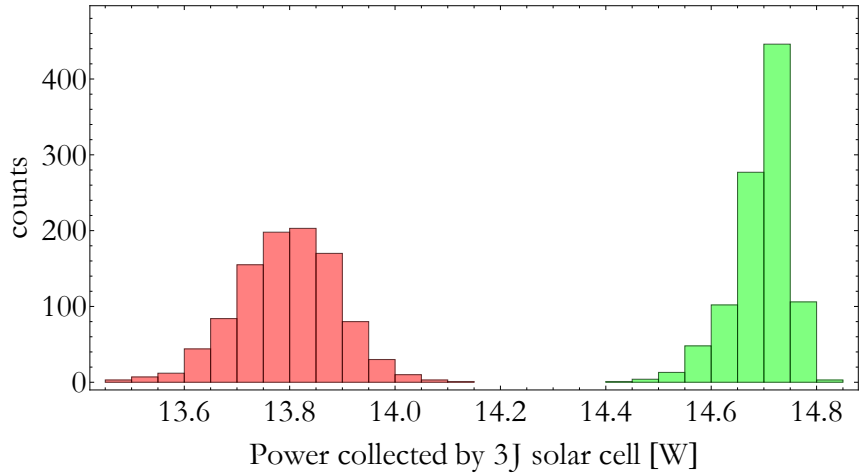

Figure 4.5: Histograms that result from the Monte Carlo simulation. In both cases the whole system is perfectly aligned respect to the sunrays. Green: the POE and SOE optical elements are both ideal. Red: the POE considered is the optical element reconstructed after the CMM measurement presented in figure 3.4. The mean values of the histograms are $(14.696 \pm 0.053)W$ and (13.795 ± 0.095)W, respectively. The standard deviations include the Monte Carlo standard deviations as well as the uncertainty introduced by the ray tracing simulation.

$$\sigma_{\text{histogram}} = \sqrt{\sigma_{\text{stat}}^2 + \sigma_{\text{MC}}^2} \tag{4.3}$$

where $\sigma_{\text{histogram}}$ is the standard deviation of the histograms shown in figure 4.5 (0.053W and 0.095W for the ideal and the real POE, respectively), $\sigma_{\text{stat}} = 0.026W$ is the statistical error calculated in Appendix A and σ_{MC} is the standard deviation due to the Monte Carlo simulation. It follows that the uncertainties introduced by the Monte Carlo simulation are

$$\begin{aligned} \sigma_{\text{MC}} &= \sqrt{\sigma_{\text{histogram}}^2 - \sigma_{\text{stat}}^2} \\ \sigma_{\text{MC}}^{ideal} &= \sqrt{0.053^2 - 0.026^2} = 0.046W \\ \sigma_{\text{MC}}^{real} &= \sqrt{0.095^2 - 0.026^2} = 0.091W \end{aligned} \tag{4.4}$$

This result means that if the TwinFocus® system is perfectly aligned, each optical element is perfectly manufactured and only the assembling errors are taken into account, then the average power collected by the 3J cell is $(14.696 \pm 0.046)W$. If instead a real POE is considered, and more exactly the one presented in figures 3.4 and 3.5, then the average power expected is (13.795 ± 0.091)W. The first result is in good agreement with the nominal one

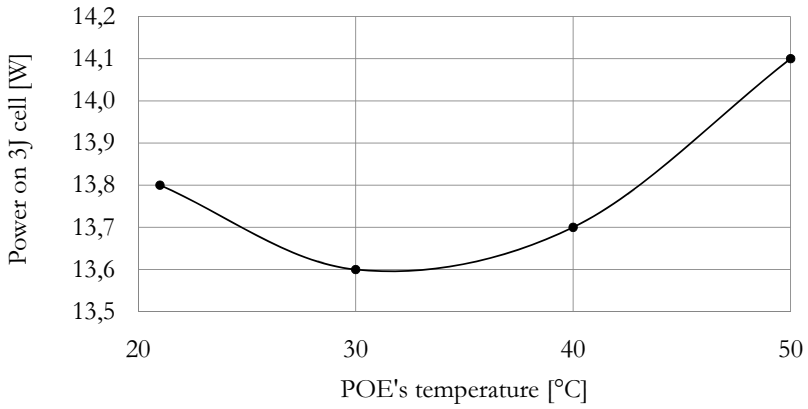

Figure 4.6: Power collected by the 3J cell for different POE's temperatures. In the ray tracing simulation the number of simulated rays is $4 \cdot 10^7$ with a 2×2 source, so the statistical error of the power value is $4 \cdot 10^{-3}$W. More details can be found in Appendix A.

(14.74W, ref. figure 2.12) and the width of the distribution is only 0.046W, so this means that the assembling process does not introduce a significant variability in the power collected by the 3J solar cell. The latter result has a small dispersion too, which is only 0.091W, and the power collected by the 3J cell is slightly larger than the expected one (13.74W, ref. figure 3.5). This is due to the receiver's offset along z' axis, which helps the imperfect POE to collect a higher light power.

4.3 Effect of the temperature on POE performance

The last tolerance analysis investigated concerns once more the POE because this optical element could affect the optical efficiency also with small shaping imperfections. In this section is described how the POE's temperature is related to the power collected by the 3J solar cell. Only the POE's temperature effect is investigated while all the other parameters are left constant to their nominal values. As already described in section 3.1.2, the measure of the POE's surfaces was performed through a CMM. After the point cloud measurement the POE was then reconstructed and imported in the ray tracing software. The measure was repeated at four different POE's temperatures using two tungsten lamps as heaters: the lamps were placed close to the back side of the POE and they were controlled by a thermocouple connected to a closed-loop circuit and in contact with the back side of the POE. During all the measures the air temperature was 21°C. The result of the POE reconstruction and the subsequent ray tracing simulation is shown in figure 4.6. The graph shows that the power collected by the

3J solar cell has a minimum when the POE's temperature is about 30℃. Thank to thermal simulations and on-field measures it was estimated the POE's temperature under operating conditions (i.e. when the TwinFocus® system is placed outdoor). This value depends on several factors such as the Sun irradiance level, the position of the POE into the module and the wind speed. For this reason POE's temperature cannot be estimated with high accuracy and it is about 15℃ above the air temperature. In the hypothesis that during a sunny day the air temperature is $30 - 35$℃, then the POE's temperature should be close to 50℃. The graph in figure 4.6 shows that close to this temperature, for example in the range $45 - 50$℃, there is a variability in the power collected by the 3J solar cell (i.e. in the short-circuit current generated) of about 2%. This result will be discussed again the next chapter when the estimated electrical power generated by a TwinFocus® module will be compared with a measure in operating conditions.

Chapter 5

Electrical characterization of TwinFocus optics

This chapter begins with the estimation of the short-circuit current and the electrical PV power generated by a TwinFocus® semi-concentrator starting from the Spectral Transfer Function (STF) measured in the previous chapters. After that a simple model of the triple junction (3J) solar cell is introduced, which is then used to link the ray tracing radiometric results with the expected electrical performances. The results are compared with outdoor measures and a novel current-voltage meter for the measurement of the CPV module current-voltage curve is also presented.

After that the design, the tolerance study, the manufacturing process and the indoor test of TwinFocus® optics were concluded an outdoor test of the whole system was necessary. For this purpose the prototypes analyzed in the previous chapter were used to assemble some TwinFocus® modules. Their outdoor performances were measured and compared with the expected peak power. The first two sections of this chapter are devoted to the estimation of the of the power generated by a TwinFocus® module in operating conditions. The approaches adopted in these first two sections are different: in the first one the TwinFocus® performance is estimated basically from the Spectral Transfer Function and from the 3J cell datasheet, while the second section refine the first estimation including a simple electric model of the 3J solar cell.
Before facing the power estimation problem, the definition of standard measuring conditions are given. These have been extensively discussed over the years, and a standard definition nowadays largely adopted is [73] [74]:

- CSTC (Concentrator Standard Test Conditions): 900W/m^2 direct-normal irradiance, 25℃ cell temperature, ASTM G173-03 Direct reference spectrum. (laboratoty conditions)

Spectrolab C3MJ+ datasheet	
V_{oc}	3.21 V
I_{sc}	7.19 A/cm^2
dV_{oc}/dT	-4.3mV/℃
dJ_{sc}/dT	$+4.7$mA/℃ $\cdot$ cm^2
$d\eta/d$T	$-0.04\%_{(abs)}$/℃
area	5.5×5.5mm^2
fingers	length 5.5mm, section $5 \times 10\mu$m^2

Table 5.1: Electrical performances of Spectrolab C3MJ+ solar cell [75] at 25℃ and under ASTM G173-03 spectrum with 50W/cm^2 irradiance.

- CSOC (Concentrator Standard Operating Conditions): 900W/m^2 direct-normal irradiance, 20℃ ambient temperature, 2m/s wind speed, ASTM G173-03 Direct reference spectrum. (ourdoor conditions)

More details about the ASTM G173-03 solar spectrum can be found in section 1.2.2. In the following sections only the CSOC are considered. Until this chapter the definition of efficiency was used to describe only the optical performances of the TwinFocus® system (equation (2.19)). The description of the whole TwinFocus® system performances is then given through the electrical efficiency, which is defined as

$$\eta_{\text{electrical}} = \frac{P_{max}^{\text{electrical}}}{P_{in}} \tag{5.1}$$

where $P_{max}^{\text{electrical}}$ is the power generated by the 3J solar cell and P_{in} (21.33W in CSOC) is the electromagnetic power that hits the front cover glass.

5.1 STF and expected electrical power

The market of multi-junction solar cells offers nowadays almost only one product for CPV application, that is the lattice-matched 3J solar cell, largely discussed in section 1.2.2. Each 3J solar cell vendor has, anyway, it's own product with small differences respect to the competitors. In this chapter only the Spectrolab C3MJ+ solar cell is considered. According to it's datasheet [75], the electrical performances of such 3J solar cell are reported in table 5.1.
The Spectral Transfer Function (STF) calculated in section 2.3 was used to estimate the short-circuit current (I_{sc}) generated by the 3J cell in CSTC. The STF used for this estimation does not include the ARC transmittance because this spectral information is already included in the External Quantum Efficiency (EQE) curves. Figure 5.1 shows then the I_{sc} generated by each $p-n$ junction. Considering that the sub-junctions are connected in

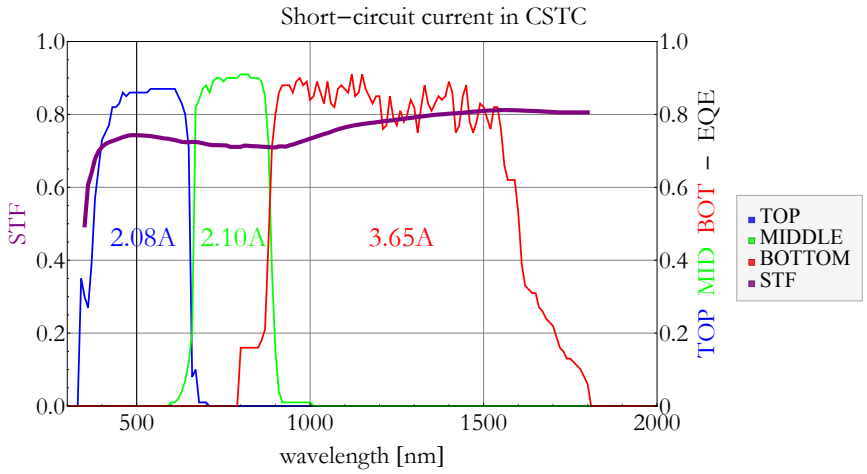

Figure 5.1: I_{sc} generated by each $p-n$ sub-junction. The expected short-circuit current in CSTC is then 2.08A.

series, the I_{sc} expected from the 3J cell in CSTC is the minimum one, which is 2.08A (TOP sub-junction). 3J cell temperature in CSOC was then introduced through a thermal simulation, whose value is

$$\mathrm{T}_{\mathrm{cell}}^{\mathrm{CSOC}} = 25℃ + \frac{{V_{oc}}^{\mathrm{CSOC}} - {V_{oc}}^{\mathrm{CSTC}}}{dV_{oc}/dT} = 25℃ + \frac{3.04\mathrm{V} - 3.21\mathrm{V}}{-4.3\mathrm{mV}/℃} = 65℃ \quad (5.2)$$

where 3.21V and 3.04V are the V_{oc} values of the 3J cell in CSTC and CSOC, respectively. This result means that in operating conditions the TwinFocus® cooling system keeps the 3J cell at 40℃ over the air temperature. The summary of the electrical performance analysis is reported in table 5.2 and the main result in CSOC is an expected electrical power generated by a 3J cell of 5.33W, with an electrical efficiency of the whole semi-concentrator of 25.0%. In conclusion it is important to underline that all these results were obtained considering a 3J cell with an uniform irradiance profile. The next section will overcome this assumption with a 3J cell model that includes local variation of the irradiance profile.

5.2 Triple junction solar cell distributed model

Traditionally a solar cell model considers one or two diodes for the recombination, one series resistance, one shunt resistance and one current source. According to figure 5.2 the current density generated by single-diode solar cell that flows through a load is

$$J = J_{ph} - J_0 \left[e^{\frac{V+JAR_s}{nk_bT/q}} - 1 \right] - \frac{V + JAR_s}{R_{sh}} \quad (5.3)$$

	3J cell at 25°C (CSTC)	3J cell at 65°C (CSOC)
V_{oc}	3.21 V	3.04 V
I_{sc}	2.08 A	2.14 A
FF	84.9%	81.9%
P_{max}	5.67 W	5.33 W
$\eta_{\text{electrical}}$	26.6%	25.0%

Table 5.2: Electrical performances of a TwinFocus® semi-concentrator in CSTC and in CSOC calculated from the STF. The 3J cell temperature was estimated from thermal simulations and outdoor measurement of V_{oc}.

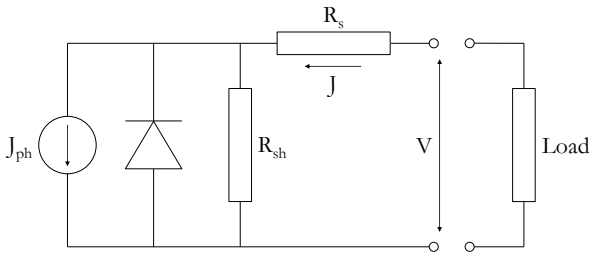

Figure 5.2: Solar cell single-diode equivalent circuit. Equation (5.3) describes its electrical properties.

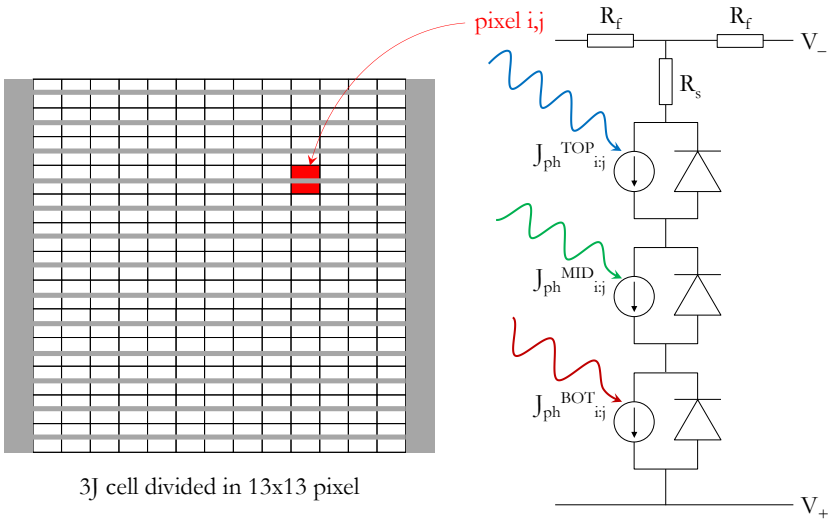

Figure 5.3: Electrical scheme of the 3J cell distributed model. On the left is shown a 3J cell with its own front metal grid (fingers). The cell is divided into 13×13 pixels, which one has the electrical scheme shown in the right figure. Each (i, j) pixel is associated to a proper irradiance level according to the irradiance profile that results from the ray tracing simulation.

where J_{ph} is the photovoltaic current density, J_0 is the reverse saturation current density, V is the load voltage, A is the solar cell area, R_s is the parasitic series resistance, n is the diode ideality factor, k_b is the Boltzmann constant, T is the cell temperature, q is the elementary charge, and R_{sh} is the parasitic shunt resistance. Because the irradiance profile over the 3J cell could be non-uniform, a three-dimensional or at least a distributed model is mandatory in order to properly describe the solar cell current-voltage (I-V) characteristic curve. Over the years many models have been introduced for single junction [76] [77] as well as multi-junction [78] [79] solar cells. In an ideal case R_{sh} and R_s are, respectively, infinite and zero. Their value influence the Fill Factor (FF), so the solar cell electrical efficiency. As shunt resistance decreases, the difference between the current density generated by the solar cell and the current density J increases, and this difference is proportional to the solar cell voltage. As series resistance increases, the difference between the junction voltage and the terminal voltage becomes greater, and this difference is proportional to the current density J. For this reason the most limiting parameter of a solar cell for its proper operation at high irradiance values is its series resistance.
A triple-junction single-diode model that takes into account only a parasitic series resistance was considered in order to study the effect of irradiance non-uniformity due to TwinFocus® optics. The model adopted considers a 3J cell divided into several pixels, each one made by the series connection of three sub-cells represented in figure 5.3. In this model the series resistance takes into account only the emitter sheet resistance (R_s) and the front metal grid (R_f, also known as fingers) because these are the most critical particularly at high current density. As shown in figure 5.3 the latter resistance connects each pixel together along the direction of the grid. The emitter resistance is

$$R_s = R_{sheet} \cdot ratio = 100\frac{\Omega}{\square} \cdot 1 \cdot \frac{1}{6} = 16.7\Omega \tag{5.4}$$

where R_{sheet} is the sheet resistance [80] [81], the $ratio$ factor is the aspect ratio of a pixel (a square has an aspect ratio of 1), and 1/6 is a factor discussed in section C.2. The finger resistance is

$$R_f = \rho_{Al}\frac{l_f}{S_f}\frac{n_p}{n_f \cdot n_p} = 2.65 \cdot 10^{-8}\Omega\text{m}\frac{5.5 \cdot 10^{-3}\text{m}}{50 \cdot 10^{-12}\text{m}^2}\frac{1}{6} = 0.01567\Omega \tag{5.5}$$

where ρ_{Al} is the aluminum resistivity, l_f and S_f are respectively the fingers length and cross section, n_p is the number of pixels along a cell side, and n_f is the number of fingers. The factor 1/6 is discussed in section C.2. For what concerns the choice of n_p, as a rule of thumb the larger it is the more accurate is the distributed electrical model. Anyway, the larger the number of 3J cell pixels the slower are both the ray tracing and the electrical

	3J cell at 25℃ (CSTC)	3J cell at 65℃ (CSOC)
V_{oc}	3.21V	3.04V
I_{sc}	2.09A	2.14A
FF	84.4%	82.4%
P_{max}	5.65W	5.37W
$\eta_{\text{electrical}}$	26.5%	25.2%

Table 5.3: Electrical performances of a TwinFocus® semi-concentrator in CSTC and in CSOC simulated through the distributed model.

distributed model simulations, but the smaller the number of 3J cell pixels the larger is the peak/mean ratio error. According to figure 2.11 the number of 13 pixel for each cell side was chosen as a trade-off between these factors.

The setup of the simulation is deeper discussed in Appendix C, particularly for what concerns the dependencies of the model parameters respect to the cell temperature and the concentration factor. The distributed model was used to simulate the 3J cell in CSOC using the prescribed TwinFocus® optics presented in chapter 2. This means that the 3J cell simulated temperature is 65℃. The system was simulated in various tilting conditions in order to compare the electrical results with the tolerance analysis presented in section 4.1. Through the electrical distributed model just presented is it possible to simulate the I-V curve of a solar cell, as the one presented in figure 5.4. From this simulation some characteristic values, such as I_{sc}, V_{oc}, FF, P_{max} and electrical efficiency $\eta_{\text{electrical}}$, are obtained. The power that hits the front cover glass is 21.33W, so the electrical efficiency was calculated using equation (5.1) respect to this input power. Table 5.3 summarizes the main results of the distributed model simulation: the model predicts an electrical efficiency of 26.5% and 25.2% in CSTC and in CSOC, respectively. These results have an error that is less than 1% respect to the efficiency predicted from the STF, reported in table 5.2. This means that the model is quite accurate and that the expected irradiance profile nonuniformity does not affect the 3J electrical efficiency.

Figure 5.5 shows the results of the electrical distributed model simulation. The main result is represented by the electrical efficiency map, which quantify the expected maximum efficiency conversion and also defines the electrical acceptance angles. In section 4.1 the optical acceptance angles were calculated from the map representing the radiative power collected from a 3J cell (top-left map of figure 5.5), which were $\pm 0.85^{\circ}$ for x axis and $+1.05^{\circ}/-1.35^{\circ}$ for y axis. The electrical acceptance angles are instead calculated from the map representing the electrical power generated by a 3J cell (bottom-left map of figure 5.5), which are $\pm 0.80^{\circ}$ for x axis and $\pm 1.00^{\circ}$ for y axis. The latter is also proportional to the electrical efficiency map.

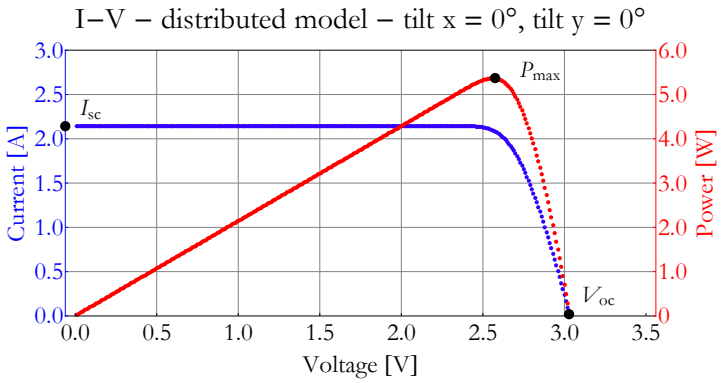

Figure 5.4: I-V curve as a result of the electrical distributed model. The curve represents the expected electrical performance of TwinFocus® system in CSOC if no manufacturing or system errors are introduced. I_{sc}= 2.14A, V_{oc}= 3.03V, P_{max} = 5.37W.

5.3 Outdoor test of TwinFocus® concentrator

The last test presented concerning TwinFocus® system is the outdoor measurement of its electrical performances. In order to accurately perform the measure of the I-V curve a dedicated I-V meter was designed and realized. After that the I-V curve tracer is presented, a comparison between the outdoor measures and the distributed model simulation are discussed.

5.3.1 I-V curve tracer

Most of the I-V curve tracers for photovoltaic applications use a capacitor as a PV load: the capacitor accumulates charges whilst the current and the voltage data are measured and stored. Many solutions to the problem of tracing the I-V curve of a PV module have been presented [82] and the I-V meter realized is a variant of the bipolar power amplifier solution [83] [84]. According to its electrical scheme, presented in figure 5.6, the voltage of the node B is controlled by the input voltage $V_{control}$. More exactly the amplification factor of the operational amplifier X3 is

$$G_{X3} = -\frac{R5}{R11} = -3 \tag{5.6}$$

and the voltage of the node B, said V_B, drives the voltage of node A, said V_A. The latter is also the 3J cell voltage, which is red through the operational amplifier X2. The current generated by the 3J cell flows through the cables R_s that connect it to the I-V curve tracer, then flows through the Shottky diode D9 (MBR340), the resistor R7 (1Ω), the bipolar transistor Q2 (TIP 3055), and is finally absorbed by the negative reference voltage supplier. Resistor R7 is necessary to measure the current intensity, which is done

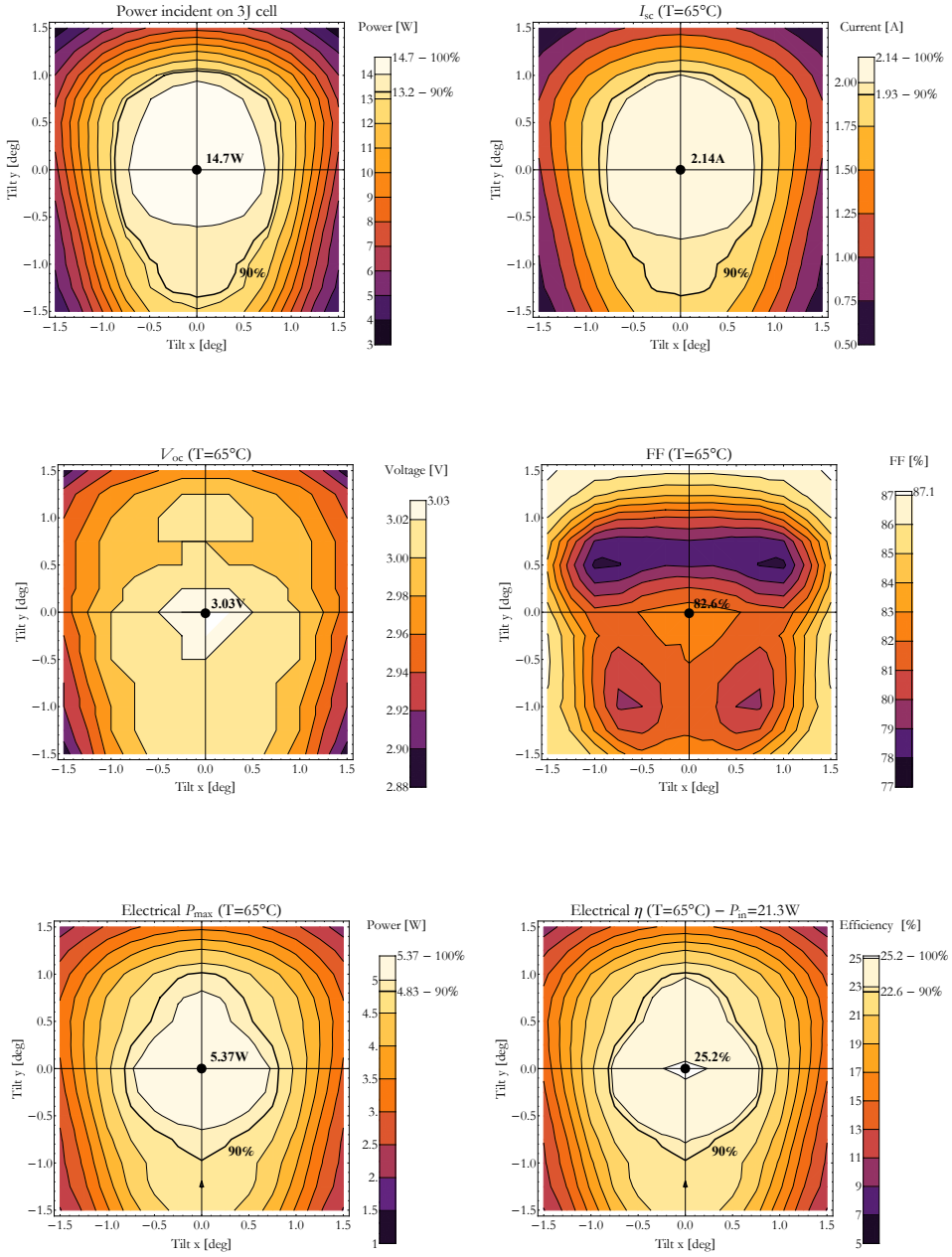

Figure 5.5: Results of the electrical distributed model simulation. The 3J cell electrical performances were simulated in CSOC ($T_{3J} = 65$°C). The top-left map is the same presented in figure 4.1 and represents the radiative power collected by the 3J cell. From this map the optical acceptance angles were calculated. The map in the bottom-right represents the electrical efficiency of the system and defines the electrical acceptance angles.

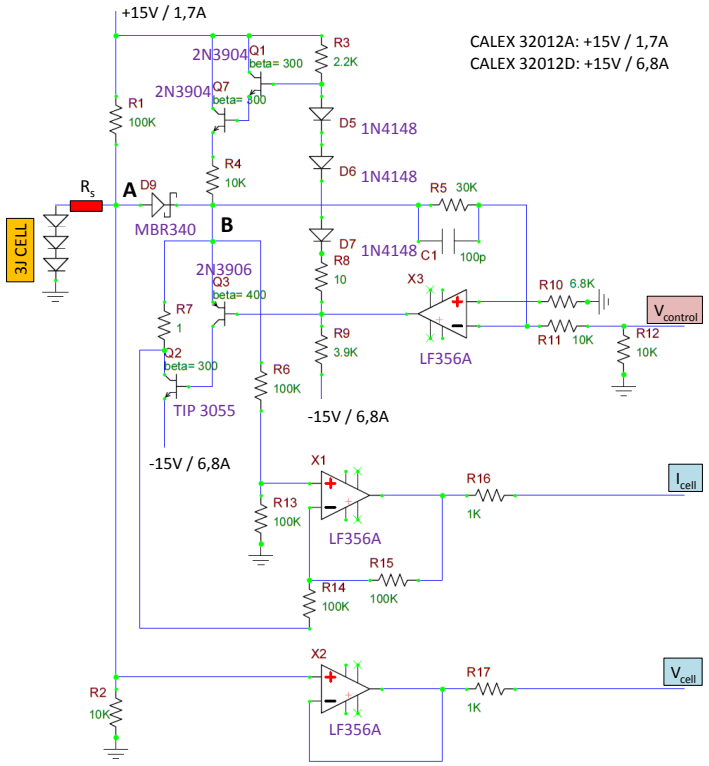

Figure 5.6: I-V curve meter electrical circuit. The input voltage $V_{control}$ drives the 3J cell voltage V_A, while the 3J current flows through R7.

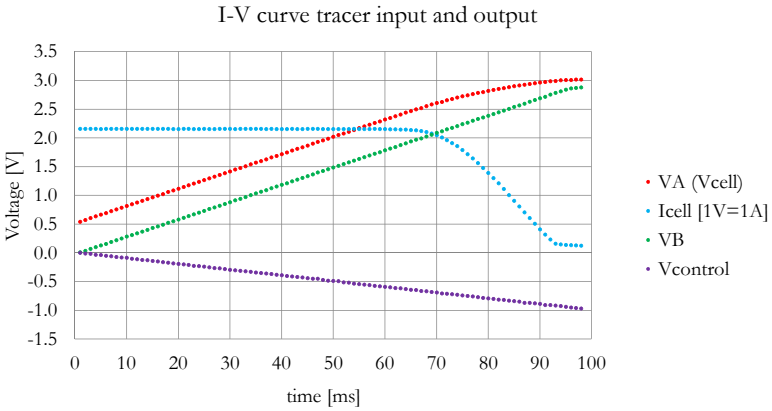

Figure 5.7: Input and output voltages of the I-V curve tracer instrument. Input voltage ($V_{control}$) is represented with violet dots. This input is multiplied by a factor -3 and is measured in point B (V_B, green dots). 3J current and voltage are represented, respectively, with red and blue dots. This I-V curve is made by 100 points acquired at a rate of 1kHz.

	cell_1	cell_2	model
V_{oc}[V]	3.020 ± 0.023	3.020 ± 0.023	3.010
I_{sc}[A]	2.105 ± 0.049	2.085 ± 0.049	2.049
$V_{\max}$[V]	2.522 ± 0.023	2.550 ± 0.023	2.530
$I_{\max}$[A]	2.050 ± 0.049	2.012 ± 0.049	1.999
P_{max}[W]	5.17 ± 0.13	5.13 ± 0.13	5.058
FF[%]	81.5 ± 2.9	81.3 ± 2.9	82.0
$\eta_{\text{electrical}}$[%]	24.2 ± 0.6	24.1 ± 0.6	23.7

Table 5.4: Comparison between the measured and the simulated 3J solar cells in outdoor conditions.

through the operational amplifier X1. Resistor R7 value is exactly 1Ω and is used to convert the measured voltage into the cell current with a gain of 1A/1V. The electrical scheme also highlights in red the parasitic series resistance introduced by the cable that connects the 3J cell to the I-V meter. It's influence in the I-V data must be taken into account due to the high short-circuit current. Parasitic series resistance value is

$$R_s = \rho_{Cu}\frac{l_{cable}}{S_{cable}} = 1.5 \cdot 10^{-8}\Omega\text{m}\frac{5\text{m}}{1.5\text{mm}^2} = 5 \cdot 10^{-2}\Omega \tag{5.7}$$

where ρ_{Cu} is the copper resistivity, l_{cable} and S_{cable} are the cable length and cross section, respectively.
The I-V curve tracer was controlled with a LabVIEW virtual instrument: a NI9263 module regulates the input voltage $\text{V}_{\text{control}}$ while voltages V_{cell}, I_{cell}, and V_{B} were acquired with a NI9215 module. Figure 5.7 shows the control and output voltages acquired from a 3J cell.

5.3.2 Measures and comparison with distributed model

The electrical distributed model and the I-V curve tracer discussed, respectively, in section 5.2 and 5.3.1 are now compared. During the sunny days of 2014 several outdoor measures of TwinFocus® concentrators were performed, but only some of them were in acceptable operating conditions: CSOC require particular irradiance spectrum and intensity, and the air temperature cannot be too distant to the standard value, so the I-V curves here presented concern a concentrator that was measured in conditions close to the CSOC ones. The operating conditions for the presented measures were:

- date and hour: 9^{th} June 2014, 16:45 (daylight saving time);
- place: Legnaro, Padua, Italy (45.3546N, 11.9457E);
- DNI: $900\text{W/m}^2 \pm 1\%$, AirMass 1.50 Direct;
- $T_{air} = 30℃ \pm 1.5℃$.

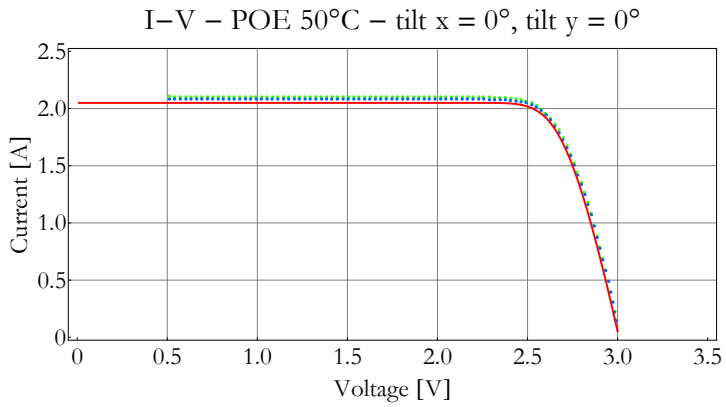

Figure 5.8: Comparison between electrical distributed model and outdoor measures. The red line represents the simulated I-V curve obtained through the POE reconstructed at 50℃ and the 3J cell at 70℃, while the green and blue dots represent the I-V curves of two TwinFocus® semi-concentrators measured in CSOC.

According to the measured air temperature of 30℃ the distributed model assumed that the simulated cell temperature was 70℃ and that the POE temperature was 50℃, so the POE measured through a CMM in this working conditions (section 4.3) was used for the ray tracing simulation. Voltage and current of the 3J cells were both measured with a NI9215 cDAQ module and are affected by several errors, which are now discussed.

- Voltage errors.
    - o Air temperature: the air temperature influences the 3J temperature, so its voltage. The thermocouple used for the measure (J type) has an accuracy of ±1.5℃ which corresponds to ±6.5mV;
    - o Wind speed: this parameter influences the 3J temperature, so its voltage. According to thermal simulations (here not shown), ±5℃ is the expected uncertainty of the 3J cell temperature. This factor corresponds to an error of ±22mV;
    - o DAQ reading error: NI9215 has a 16-bit DAC, so its quantization error in the range -10/+10V is ±0.31mV, which is negligible respect the errors related to the 3J temperature. Gain and offset errors, 0.02% and 0.014% respectively, are also negligible.
- Current errors.
    - o Air temperature: the air temperature influences the 3J temperature, so its current. The thermocouple used for the measure (K type) has an accuracy of ±1.5℃ which corresponds to a negligible error of ±2.0mA;

- Wind speed: this parameter influences the POE temperature, so its shape. According to thermal simulations and to figure 4.6, ±5°C is the expected uncertainty of the POE temperature. This factor corresponds to an error of about ±2% = ±42mA on the power collected by the 3J cell, so on the current produced;
- DNI: this value, measured with a pyroheliometer Kipp&Zonen CHP1, is directly related to the current produced. During the measurements it had a variability of ±1% = ±21mA.
- Assembling: according to section 4.2.2 the assembling imperfections introduce an error on the power collected by the 3J cell of ±0.091W/17.795W = ±0.66% which means ±14mA;
- DAQ reading error: NI9215 has a quantization error of ±0.31mV, which is negligible as well as gain and offset errors.

The conclusion of this error analysis is that the measure presented has errors on the voltage and current values of ±23mV and ±49mA, respectively. The measurements and their comparison with the distributed model are summarized in the table 5.4: the agreement between the simulated and measured values is good.

5.4 TwinFocus® system prototype

The concentrated photovoltaic module was developed in cooperation with four private companies. The companies aim to enter into the solar market with an innovative product, thus they funded part of the research. At the end of this PhD work the result of this cooperation was the realization of five prototypes. For this prototyping action it was decided that a complete module, named TwinFocus®, is made of 12 concentrators (hence 24 3J solar

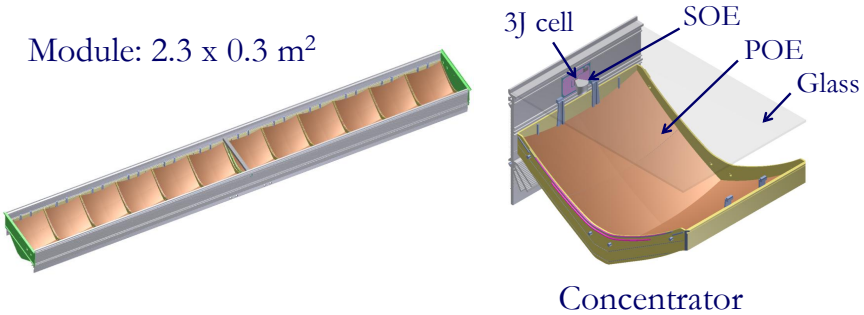

Figure 5.9: Rendering of a TwinFocus® module (left) with a detailed view of the optical components (right). The module shown is made by 12 concentrators and has an active area of approximately 0.57m^2.

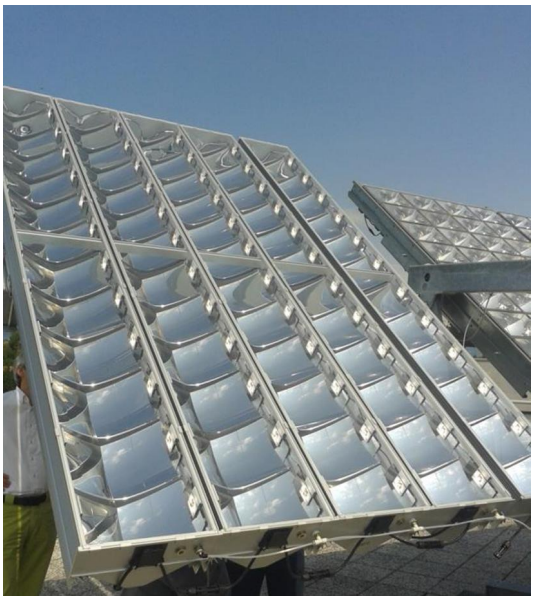

Figure 5.10: Picture of 5 complete modules mounted on a tracking system located in the spin-off *AtemEnergia Srl*® headquarter.

cells) assembled in a row. The module has then the dimension of $2.3 \times 0.3\text{m}^2$ with an active area of 0.57m^2. If no system or process errors are introduced the expected electrical peak power in CSOC is 129W, which is 24 times the power reported in table 5.3. The mechanical study performed on these prototypes resulted in the tolerance analysis discussed in chapter 4.
Figure 5.10 shows 5 complete modules that are currently acquiring data. According to the analysis conducted in section 3.1.2, these prototypes should be affected by a lack of approximately 7% between the expected and the measured electrical peak power, but figure 5.11 and table 5.5 highlight a larger gap. The measurement was performed with an I-V curve tracer that is a variant of the instrument presented in section 5.3.1. The operating conditions for the presented measures were:

- date and hour: 17^{th} June 2014, 17:00 (daylight saving time);
- place: Legnaro, Padua, Italy (45.3546N, 11.9457E);
- DNI: $711\text{W/m}^2 \pm 1\%$, AirMass 1.57 Direct;
- $T_{air} = 30℃ \pm 1.5℃$.

The results of the measurement are summarized in table 5.5. The current values (and in first approximation also the power value) are proportional to the irradiance level: with a simple proportion between the DNI level in CSOC (900W/m^2) and in the measured condition (711W/m^2) the expected

V_{oc}[V]	70.1
I_{sc}[A]	1.55
$V_{\max}$[V]	63.5
$I_{\max}$[A]	1.39
P_{max}[W]	88.3
FF[%]	81.2
$\eta_{\text{electrical}}$[%]	22.5

Table 5.5: On-field electrical characteristics of a TwinFocus® module.

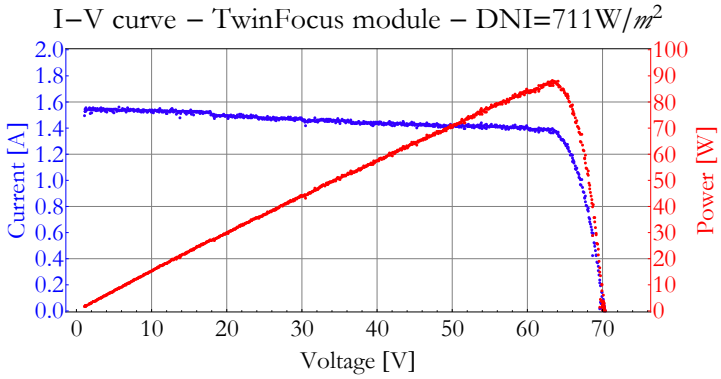

Figure 5.11: I-V curve of a TwinFocus® module with DNI= 711W/m^2. It's electrical efficiency (22.5%) has a lack that is greater than the expected 7% between the nominal value (25.2).

peak power of one of the assembled modules shown in figure 5.10 is approximately 112W. The gap with the expected 129W is larger than 7%. It is not within the scope of this thesis to analyze this difference, but few hypothesis can be made. The I-V curve in figure 5.11 shows a large variability in the current generated by the 3J cells because the current generated in the maximum power condition is less than the short-circuit current. This could be due to system/process errors and unknown factors:

- variability in the aluminum coating reflectivity;
- mechanical assembling errors not considered in the tolerance analysis;
- the module contains a volume of air of about 60 l, so the natural convection inside the module causes a variability in the temperature of the POEs and the 3J cells.

In addition to these uncertainties the weather conditions also influence the module efficiency. It's a bit challenging to measure the system performances in CSOC because spectral conditions, air temperature and wind speed greatly influence the module efficiency.

Chapter 6

Conclusions

In this chapter the activities conducted into this PhD work are summarized, particularly for what concerns the path for designing and manufacturing a cost effective nonimaging optics. The chapter concludes with some hints for the evolution of TwinFocus® optics.

6.1 Summary

The aim of this PhD thesis is to use mature and cost-effective technologies in order to create a marketable CPV system. This thesis is particularly focused on the design of a nonimaging optics for such application. The work started from an analysis of this technology from various points of view: economical, technological, and physical. Moreover a detailed constraints analysis was carried out and a workflow procedure was developed. Its is interesting to note that the same approach adopted for this work can be applied also to the design of any other nonimaging optics device: automotive and general lighting are, in this aspect, the closest sectors to CPV technology. The choice of the injection molding technology for the production of the POE is motivated by the large know-how already understood about this process and also because it is a way to rapidly get a marketable nonimaging optics. Finding an appropriate solution to the "CPV approach" means to look for the correct trade-off between many parameters and constraints: choosing a reflector or a lens is the first step for a CPV optical designer. The choice of a reflective POE involves a lower optical efficiency because this solution requires an additional glass cover, so it can be motivate only boosting the concentration factor to a value that is large enough: reflective-based nonimaging optics solutions are not affected by chromatic aberration like refractive-based ones, so it possible to reduce the balance of system costs increasing the mirror area without the introduction of limiting spectral mismatches. A low optical efficiency means also a low electrical efficiency so a mirror-based optics can be motivated only through an accurate choice of the components using their costs as the heaviest parameter into the system's merit figure. Even though

a mirror-based optics doesn't seems the most natural choice, an electrical conversion efficiency close to 25% and a cost of about 0.64€/W (including the 3J solar cells) make TwinFocus® optics a solution that could reach the market in the near future.

The main goals reached with this PhD work are now outlined.

- Taking advantage of the approach adopted in designing imaging optics, the workflow procedure for the design of a nonimaging optics was developed. Starting from the detailed analysis of the initial constraints a freeform nonimaging doublet was designed through an iterative procedure.

- The manufacturing processes of optical components were accurately studied. An experiment for the realization of the POE was performed and useful information about the injection molding process were obtained. A deeper investigation of the process is mandatory in order to realize POEs that achieve a higher power level on the 3J solar cell.

- The tolerance analysis was faced from several points of view: system and process errors were distinguished. System error analysis showed that the optics is tolerant to system misalignments. Moreover the achieved CAP value is competitive with the state-of-the-art nonimaging optics for CPV, which means that the acceptance angle is large compared to the chosen geometrical concentration factor. System errors concerning the relative position of the optical components showed that the production process adopted for the realization of several prototypes generates an irrelevant dispersion of the power collected by the 3J solar cell. This achievement is fundamental in order to limit balance of system the assembling costs. One last original tolerance analysis concerned the reconstruction of the POE for various operating temperatures. This result highlighted a particular behavior of the POE and showed once more that a deeper comprehension of the POE behavior in various conditions is mandatory.

- A link between the optical and the electrical simulations was established: local variations of the irradiance level over the 3J cell were considered through ray tracing simulations and this data were implemented into an electrical distributed model of the 3J cell. Even though the 3J cell model adopted for the evaluation was the simple the agreement between the simulation and the measures is good.

- Several TwinFocus® prototypes were realized and for their outdoor electrical characterization a dedicated I-V curve tracer was realized. This instrument was used to measure some 3J cells in CSOC in order to compare their I-V curve with the simulated one. The realization of

several prototypes involved a real estimation of the optics cost. This result makes the TwinFocus® optics a marketable solution for CPV technology.

6.2 Opportunities for future work

The presented nonimaging optics solution provides a starting point for the development of a full CPV system. Suggestions and opportunities for the development of the presented work are now highlighted.

- A deeper investigation in the realization of the main optical element, the POE, is mandatory in order to increase the power collected by the 3J solar cell. Also the dependency of the POE shape respect to its temperature must be controlled. These tasks can be done designing an appropriate holding structure to this optical element.

- Even if the achieved irradiance profile uniformity and acceptance angle are satisfactory, an alternative improved optics shape could be designed using the integrability condition as guiding rule, looking for alternative source-target maps.

- The reconstruction of the POE through CMM measures found a good agreement with the on-field performance of the optical system. However the reconstruction of the freeform surfaces can be performed with higher accuracy using more general equations such as thin plate splines (TPS) or non-uniform rotational basis splines (NURBS).

- The simple electrical distributed model developed found a good agreement between the simulated results and the on-field measurements. However it needs a detailed study supported by measures on 3J cells in order to understand it's limits.

- In order to further reduce the optics and system costs, once that the production process of the optical components will be optimized, it will be possible to achieve higher concentration factors with a new optics. This goal can be achieved, for example, reducing the 3J area.

Appendix A

Considerations about the optimum detector quantization and the number of traced rays

In this Appendix is discussed the topic of the statistical errors introduced in choosing the number of simulated rays and the disctretization of the target. Facing the problem of setting up a ray tracing simulation such as the one represented in figure 2.12 consists in handle two important parameters: number of simulated rays and number of detector's pixels.

The situation represented in figure A.1 is now described: a source generates N rays, each one perpendicular to the source, and these rays are

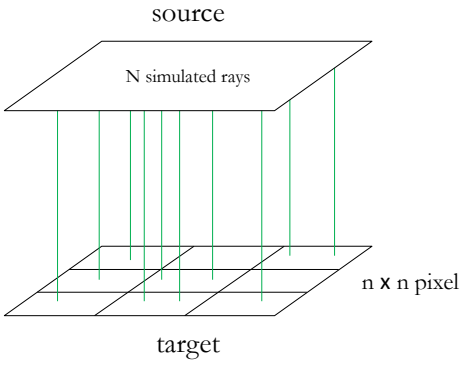

Figure A.1: A source generates N rays, which are collected by a target composed by $n \times n$ pixel. If the rays are generated with equal probability by each source's point, then the number of rays collected by each pixel follows the Bernoulli distribution.

collected by a target made by $n \times n$ pixels. Let's suppose also that the source is uniform, which means that each source's point has the same probability to generate a ray. In this situation the expected number of rays collected by each pixel is the same, so the expected illumination profile of the target is also uniform. The situation just presented is described through the Bernoulli distribution: the probability that, simulating N rays, a certain pixel collects x rays is

$$P(x,N) = \binom{N}{x} p^x q^{N-x} = \frac{N!}{x!(N-x)!} p^x q^{N-x} \tag{A.1}$$

where p is the probability of a pixel to collect a ray and $q = 1 - p$. In the situation of uniform illumination p is the same for all pixels

$$p = \frac{1}{n^2} \tag{A.2}$$

and the expected number of collected rays by each pixel is

$$E(x) = Np = \frac{N}{n^2} \tag{A.3}$$

It is well known that the variance of the Bernoulli distribution is

$$Var(x) = Npq \qquad \text{and} \qquad Var(x) = N\frac{1}{N}\left(1 - \frac{1}{n^2}\right) \approx \frac{N}{n^2} \tag{A.4}$$

This is the variance of the number of the rays collected by a generic pixel uniformly illuminated. The approximation is true when n is large enough. The percentual error of the number of rays collected by a generic pixel is then the ratio between the variance square root and the number of collected rays

$$\text{err}_{\%} = \frac{\sqrt{Var(x)}}{E(x)} 100 = \frac{n}{\sqrt{N}} \sqrt{1 - \frac{1}{n^2}} 100 \approx \frac{n}{\sqrt{N}} 100 \tag{A.5}$$

Using this equation it is possible to calculate the percentage error of the expected number of rays collected by each pixel in the situation of uniform illumination of a detector made by $n \times n$ pixels that is hitted by N rays. Equation (A.5) can also be applied to a situation in which a uniform source, that is larger than the target, generates N rays. Let's consider the situation represented in figure A.2, in which the source is 2×2 times the target. The number of rays collected by the target is then $N/n^2 = N/4$ and its percentage error is described by equation (A.5). In order to test such equation the ray tracing simulation of figure 2.12 is analyzed. A source that is 2×2 times wider than the front glass surface is considered and a number N of 10^6 rays is simulated. The expected number of rays collected by the target is then $2.5 \cdot 10^5$ while the expected incident power is, according to figure 2.12, 14.7W.

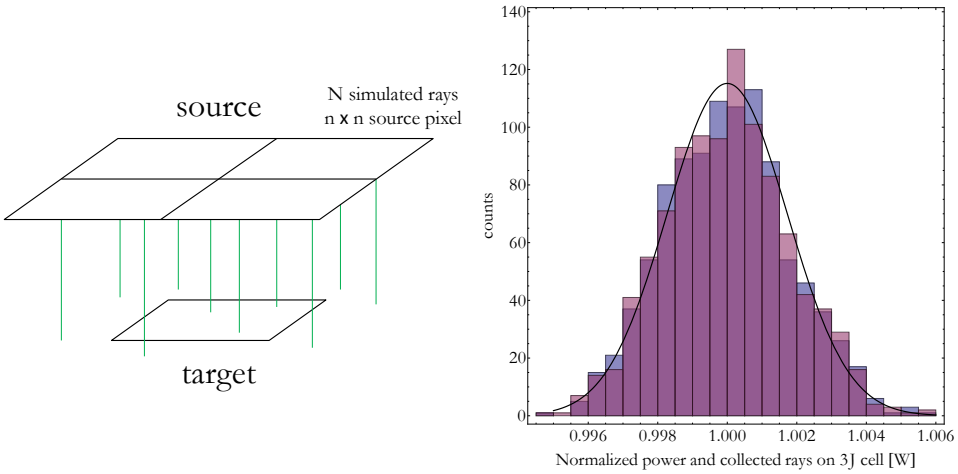

Figure A.2: Left: a uniform source generates N rays. The source is 2×2 times wider respect to the target. Right: the blue histogram represents the number of rays collected by the target while the violet histogram represents the distribution of the power collected by the target. Both histograms are normalized to their average values. Black curve represents the normalized Bernoulli distribution with $N = 10^6$ and $n = 2$.

In this case, due to the small number of soruce's pixels, it is mandatory to use the un-approximated equation, so $\text{err}_{\%} = \frac{2}{\sqrt{10^6}}\sqrt{1 - \frac{1}{2^2}}100 = 0.173\%$. The figure A.2 represents the distribution of the number of rays collected by the target (blue histogram) and the distribution of the power collected by the target (violet histogram). Both histograms are normalized to their average value and their standard deviations are both 0.178%. Figure A.2 shows also the comparison of the simulated histograms with the Bernoulli distribution, which variance is 0.173%. The agreement between the standard deviations is good, so it has been proved that equation (A.5) is correct for the number of collected rays as well as the power collected by the target.

Appendix B

Optical elements drawings

This appendix contains some additional data about the mechanical dimensions of the primary and secondary optical elements.

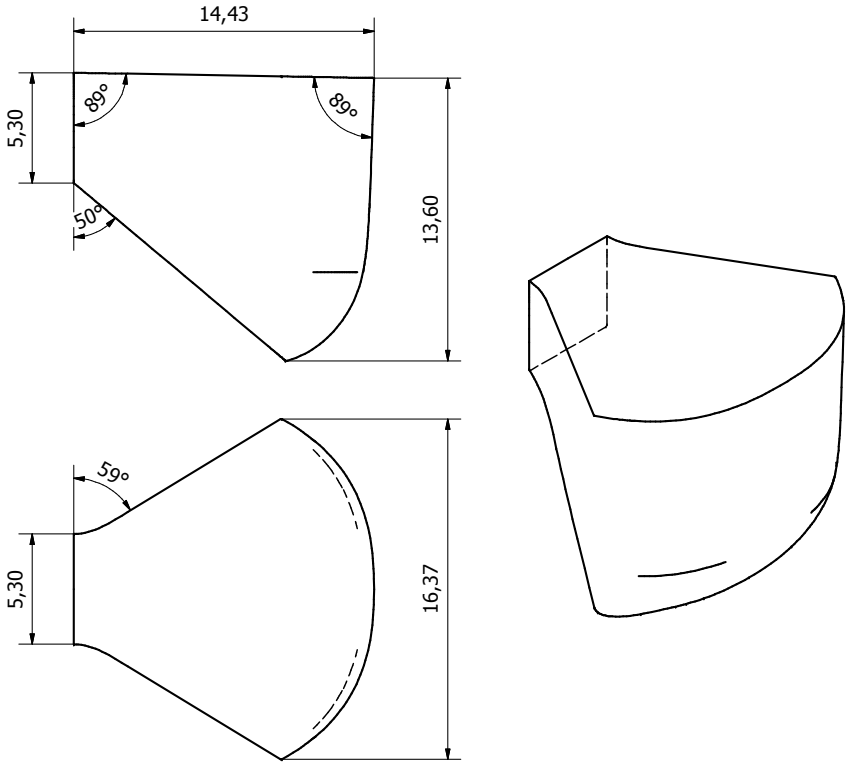

Figure B.1: SOE drawing.

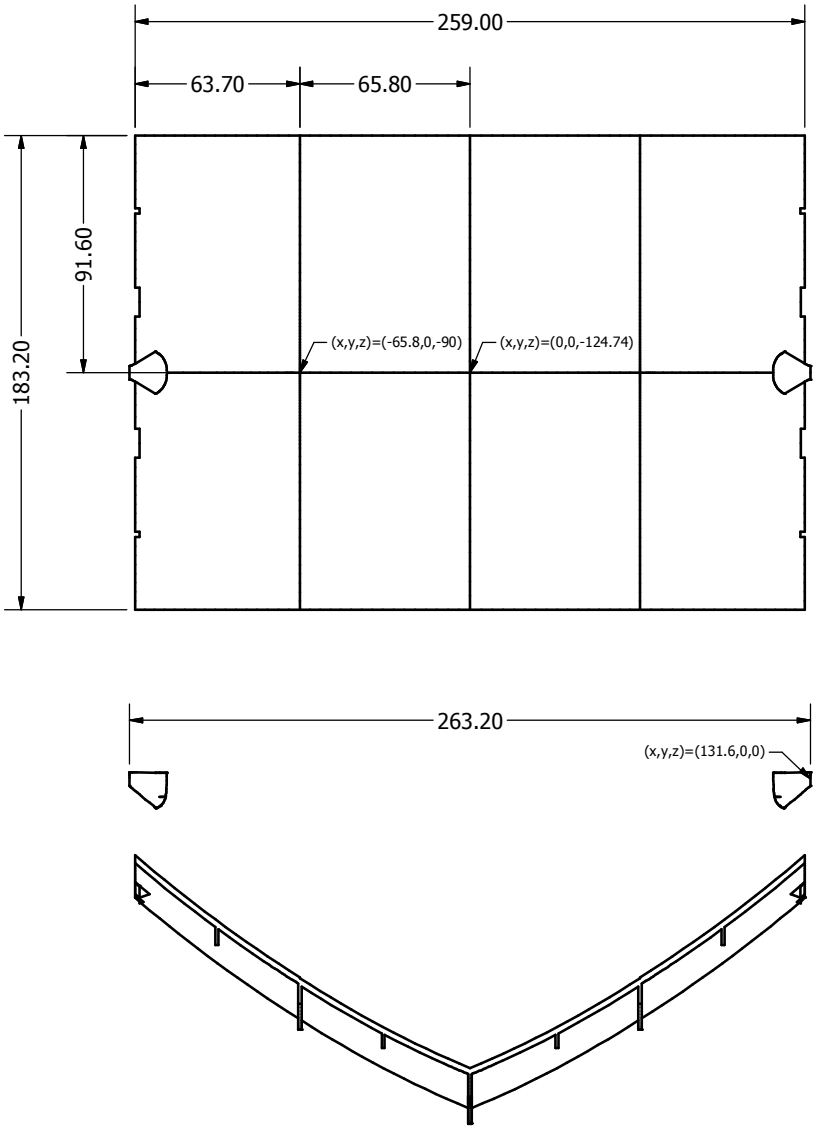

Figure B.2: POE drawing.

Appendix C

3J electrical distributed model

This appendix gives some additional information about the 3J electrical distributed model presented in section 5.2.

C.1 Distributed model

The main equation that governs the 3J solar cell electrical behavior is

$$I = I_{ph} - I_0 \left[e^{\frac{V+IR_s}{nk_bT/q}} - 1 \right] - \frac{V + IR_s}{R_{sh}} \tag{C.1}$$

where I is the current that flows into a load connected to the cell, I_{ph} is the photovoltaic current, I_0 is the reverse saturation current, V is the load voltage, R_s is the parasitic series resistance, n is the diode ideality factor, k_b is the Boltzmann constant, T is the cell temperature, q is the elementary charge, and R_{sh} is the parasitic shunt resistance. The first assumption made was that for this 3J cell model the last term is negligible, which means that the parasitic shunt resistance is large enough to drop the last term. The simulation of the electrical distributed model was performed with Matlab® and Simulink®. The latter tool is in particular a software which already contains several pre-defined electrical solar cell models. The model adopted for the simulation of the distributed 3J cell requires the definition of the following parameters

- standard irradiance (Irr_0): 900W/m^2 [74];
- I_{sc} std. irrad. (I_{ph_0}): 2.08A [75];
- V_{oc} std. irrad.: $V_{oc}^{TOP} = 1.59$V, $V_{oc}^{MID} = 1.20$V, $V_{oc}^{BOT} = 0.42$V [38];
- standard cell temperature (T_{ref}): 25℃ [74];

- energy-gap at 25℃: $E_g^{TOP} = 1.79\text{eV}$, $E_g^{MID} = 1.39\text{eV}$, $E_g^{BOT} = 0.68\text{eV}$ [85].

Equation (C.1) depends also by the following equations. The short-circuit current has a linear dependency respect to the input irradiance Irr

$$I_{ph} = I_{ph_0} \frac{Irr}{Irr_0} \tag{C.2}$$

and it also depends by the cell temperature T

$$I_{ph}(T) = I_{ph} \left[1 + \frac{\alpha_{I_{ph}} A}{I_{ph}} (T - T_{ref}) \right] \tag{C.3}$$

where $\alpha_{I_{ph}} = 4.7\text{mA/cm}^2 I_{ph}$ [75] and $A = 30.25\text{mm}^2$ is the 3J area. The inverse saturation current depends by the temperature

$$I_0(T) = I_0 \left(\frac{T}{T_{ref}} \right)^{\frac{\alpha_{I_0}}{n}} e^{E_g \left(\frac{T}{T_{ref}} - 1 \right) / nk_B T/q} \tag{C.4}$$

where $\alpha_{I_0} = 3 + \gamma/2$ ($\gamma = 7$) [85], and n is the diode ideality factor. The latter parameter also depends by the concentration factor [86], and according to Ref. [87] table C.1 summarizes the chosen values.

conc	n_{InGaP}^{TOP}	n_{InGaAs}^{MID}	n_{Ge}^{BOT}
1	2.00	2.00	1.00
10	1.75	1.50	1.00
50	1.20	1.40	1.00
100	1.20	1.20	1.00
500	1.00	1.00	1.00

Table C.1: Ideality factor values for various concentration factors ($1sun = 0.09\text{W/cm}^2$). The intermediate n values were obtained through a linear interpolation.

Starting from these equations and assumptions the model was tested in the hypothesis that the illumination profile was uniform. The distributed model was then tested assuming that all the TOP (as well as $MIDDLE$ and $BOTTOM$) sub-junctions received the same radiative flux. The model was tested for various concentration factors and for various cell temperature in order to simulate CSTC (25℃) and CSOC (65℃). The results are summarized in figure C.2 and their comparison with measurements reported in literature [75] [86] makes the model acceptable. With this model the maximum efficiency in CSTC is 39% and is expected for a concentration factor close to $200 - 300\times$.

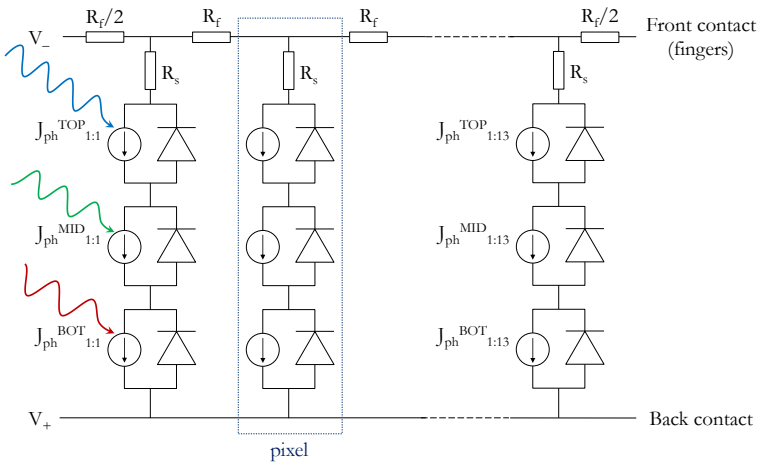

Figure C.1: Equivalent electrical circuit of the 3J cell that has been modeled with 13×13 pixels. The figure shows a row of pixels along one finger.

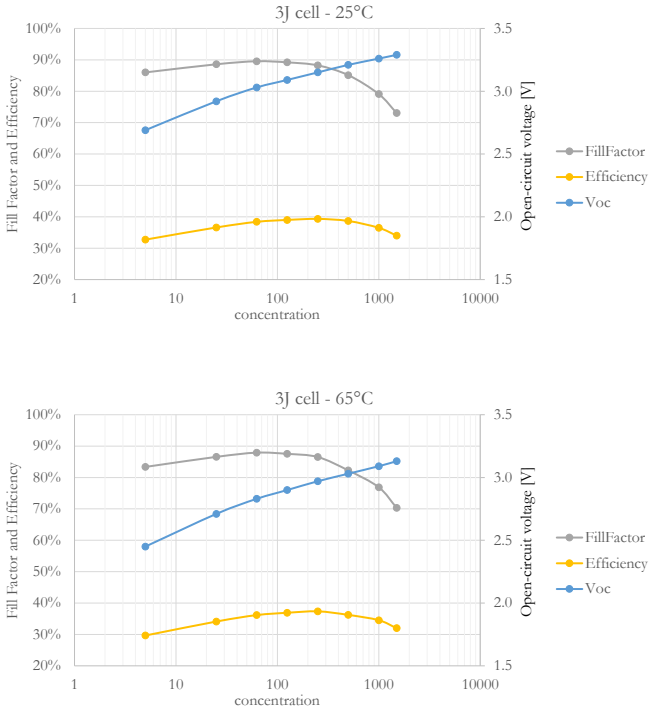

Figure C.2: The graphs summarize the results of the 3J electrical distributed model for constant irradiance profiles. The simulations were performed for various cell temperatures (25℃ and 65℃) and for various concentrations factors.

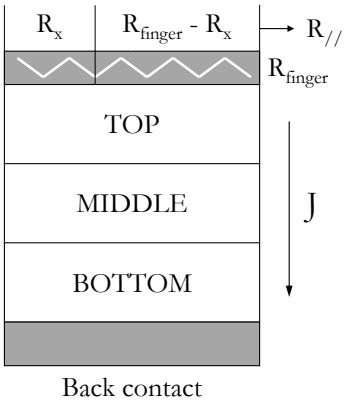

Figure C.3: Cross section of a 3J cell that highlights in particular the front metal grid electrical contacts

C.2 Equivalent series resistance

Let's consider the electrical circuit shown in figure C.3. A 3J cell generates the current density J and has front and back electrical contacts. These contacts introduce series resistances that must be included in equation 5.3. In this configuration the back electrical contact has a negligible series resistance and only the finger parasitic resistance is considered. Let's suppose that the finger grid has resistance R_{finger} and is in contact with the *TOP* p-n junction for all it's length L. The series resistance is then the average value of all the parallel resistances $R_{//}$

$$R_{//} = \left(\frac{1}{R_x} + \frac{1}{R_{\text{finger}} - R_x} \right)^{-1} \tag{C.5}$$

where R_x is represented in figure C.3. The equivalent series resistance is then

$$\begin{aligned} R_{eq} &= \frac{1}{L} \int_0^L R_{//}\, dx = \frac{1}{L} \int_0^L \frac{R_x \left(R_{\text{finger}} - R_x \right)}{R_{\text{finger}}}\, dx = \\ &= \frac{1}{L} \int_0^L \frac{\rho x \left(\rho L - \rho x \right)}{\rho L}\, dx = \frac{R_{\text{finger}}}{6} \end{aligned} \tag{C.6}$$

where ρ is the linear resistivity, $R_x = \rho x$ and $R_{\text{finger}} = \rho L$. In addition to equations (C.1)-(C.4) R_{eq} is temperature dependent according to this equation

$$R_{eq}(T) = R_{eq} \left[1 + \alpha_{R_{eq}} \left(T - T_{ref} \right) \right] \tag{C.7}$$

where $\alpha_{R_{eq}} = 4.29 \cdot 10^{-3} ^{\circ}\text{C}^{-1}$ [88] is the temperature coefficient of aluminum resistivity.

Bibliography

[1] A. K. Gupta and C. A. Hall, "A review of the past and current state of EROEI data," *Sustainability*, vol. 3, no. 10, pp. 1796–1809, 2011.

[2] M. Raugei, P. Fullana-i Palmer, and V. Fthenakis, "The energy return on energy investment (EROEI) of photovoltaics: Methodology and comparisons with fossil fuel life cycles," *Energy Policy*, vol. 45, pp. 576–582, 2012.

[3] G. F. Nemet, "Beyond the learning curve: factors influencing cost reductions in photovoltaics," *Energy policy*, vol. 34, no. 17, pp. 3218–3232, 2006.

[4] A. Luque, G. Sala, and I. Luque-Heredia, "Photovoltaic concentration at the onset of its commercial deployment," *Progress in Photovoltaics: Research and Applications*, vol. 14, no. 5, pp. 413–428, 2006.

[5] M. Bosi and C. Pelosi, "The potential of III-V semiconductors as terrestrial photovoltaic devices," *Progress in Photovoltaics: Research and Applications*, vol. 15, no. 1, pp. 51–68, 2007.

[6] G. S. Kinsey, R. A. Sherif, P. Pien, P. Hebert, R. R. King, and D. Aldrich, "Towards commercialization of concentrator multijunction photovoltaic modules," in *Photovoltaic Specialists Conference, 2008. PVSC'08. 33rd IEEE.* IEEE, 2008, pp. 1–3.

[7] M. Yamaguchi and A. Luque, "High efficiency and high concentration in photovoltaics," *Electron Devices, IEEE Transactions on*, vol. 46, no. 10, pp. 2139–2144, 1999.

[8] R. M. Swanson, "The promise of concentrators," *Progress in Photovoltaics Research and Applications*, vol. 8, no. 1, pp. 93–111, 2000.

[9] "http://optics.org/news/4/8/23," August 2013.

[10] "http://semprius.com/wordpress2/wp-content/uploads/semprius-35-5-percent-efficiency-sets-new-record-for-commercially-available-solar-modules.pdf," September 2013.

[11] "http://www.ise.fraunhofer.de/en/press-and-media/press-releases/press-releases-2014/new-world-record-for-concentrator-photovoltaics?set_language=en," July 2014.

[12] K. Garrard, T. Bruegge, J. Hoffman, T. Dow, and A. Sohn, "Design tools for freeform optics," in *Optics & Photonics 2005*. International Society for Optics and Photonics, 2005, pp. 58 740A–58 740A.

[13] J. Jiang, C. Cheung, S. To, K. Cheng, K. Wang, and W. Lee, "Design and fabrication of freeform reflector for automotive headlamp," in *Power Electronics Systems and Applications, 2006. ICPESA'06. 2nd International Conference on*. IEEE, 2006, pp. 220–224.

[14] S. Lee, "Optimum design and selection of heat sinks," in *Semiconductor Thermal Measurement and Management Symposium, 1995. SEMI-THERM XI., Eleventh Annual IEEE*. IEEE, 1995, pp. 48–54.

[15] H. Ye, "Thermal management of solid state lighting module," Ph.D. dissertation, TU Delft, Delft University of Technology, 2014.

[16] D. H. McClelland, "Investigation of solar concentrating photovoltaic power generators," DTIC Document, Tech. Rep., 1961.

[17] W. Beckman, P. Schoffer, W. Hartman Jr, and G. Löf, "Design considerations for a 50-watt photovoltaic power system using concentrated solar energy," *Solar Energy*, vol. 10, no. 3, pp. 132–136, 1966.

[18] A. A. Salim and N. N. Eugenio, "A comprehensive report on the performance of the longest operating 350 kW concentrator photovoltaic power system," *Solar Cells*, vol. 29, no. 1, pp. 1–24, 1990.

[19] M. O'Neill and A. McDanal, "Fourth-generation concentrator system: From the lab to the factory to the field," in *Photovoltaic Energy Conversion, 1994., Conference Record of the Twenty Fourth. IEEE Photovoltaic Specialists Conference-1994, 1994 IEEE First World Conference on*, vol. 1. IEEE, 1994, pp. 816–819.

[20] G. Sala and A. Luque, "Past experiences and new challenges of PV concentrators," *Concentrator Photovoltaics(Springer Series in Optical Sciences Volume 130)*, vol. 130, pp. 1–23, 2007.

[21] R. Sinton, Y. Kwark, J. Gan, and R. M. Swanson, "27.5-percent silicon concentrator solar cells," *Electron Device Letters, IEEE*, vol. 7, no. 10, pp. 567–569, 1986.

[22] S. Bedair, M. Lamorte, and J. Hauser, "A two-junction cascade solar-cell structure," *Applied Physics Letters*, vol. 34, no. 1, pp. 38–39, 1979.

[23] J. Olson, S. Kurtz, A. Kibbler, and P. Faine, "A 27.3% efficient $Ga_{0.5}In_{0.5}P/GaAs$ tandem solar cell," *Applied physics letters*, vol. 56, no. 7, pp. 623–625, 1990.

[24] N. H. Karam, R. R. King, M. Haddad, J. H. Ermer, H. Yoon, H. L. Cotal, R. Sudharsanan, J. W. Eldredge, K. Edmondson, D. E. Joslin *et al.*, "Recent developments in high-efficiency $Ga_{0.5}In_{0.5}P/GaAs/Ge$ dual-and triple-junction solar cells: steps to next-generation PV cells," *Solar energy materials and solar cells*, vol. 66, no. 1, pp. 453–466, 2001.

[25] R. King, D. Law, K. Edmondson, C. Fetzer, G. Kinsey, H. Yoon, R. Sherif, and N. Karam, "40% efficient metamorphic $GaInP/GaInAs/Ge$ multijunction solar cells," *Applied physics letters*, vol. 90, no. 18, pp. 183 516–183 516, 2007.

[26] F. Dimroth, M. Grave, P. Beutel, U. Fiedeler, C. Karcher, T. N. Tibbits, E. Oliva, G. Siefer, M. Schachtner, A. Wekkeli *et al.*, "Wafer bonded four-junction $GaInP/GaAs//GaInAsP/GaInAs$ concentrator solar cells with 44.7% efficiency," *Progress in Photovoltaics: Research and Applications*, vol. 22, no. 3, pp. 277–282, 2014.

[27] P. Chiu, D. Law, R. Woo, S. Singer, D. Bhusari, W. Hong, A. Zakaria, J. Boisvert, S. Mesropian, R. King *et al.*, "Direct semiconductor bonded 5J cell for space and terrestrial applications," *IEEE Journal of Photovoltaics*, vol. 4, no. 1, 2013.

[28] A. Luque, "Will we exceed 50% efficiency in photovoltaics?" *Journal of Applied Physics*, vol. 110, no. 3, p. 031301, 2011.

[29] W. Shockley and H. J. Queisser, "Detailed balance limit of efficiency of p-n junction solar cells," *Journal of applied physics*, vol. 32, no. 3, pp. 510–519, 1961.

[30] "http://www.azurspace.com."

[31] A. W. Bett, F. Dimroth, and G. Siefer, *Multijunction concentrator solar cells*. Springer, 2007, vol. 130, ch. 4, pp. 67–87.

[32] L. Zhao, "High efficiency mechanically stacked multijunction solar cells for concentrator photovoltaics," Ph.D. dissertation, University of Ku Leuven, 2011.

[33] K. Emery, D. Myers, and S. Kurtz, "What is the appropriate reference spectrum for characterizing concentrator cells?" in *Photovoltaic Specialists Conference, 2002. Conference Record of the Twenty-Ninth IEEE*. IEEE, 2002, pp. 840–843.

[34] C. Gueymard, D. Myers, and K. Emery, "Proposed reference irradiance spectra for solar energy systems testing," *Solar energy*, vol. 73, no. 6, pp. 443–467, 2002.

[35] R. King, A. Boca, W. Hong, X. Liu, D. Bhusari, D. Larrabee, K. Edmondson, D. Law, C. Fetzer, S. Mesropian *et al.*, "Band-gap-engineered architectures for high-efficiency multijunction concentrator solar cells," in *24th European Photovoltaic Solar Energy Conference and Exhibition, Hamburg, Germany*, vol. 21, 2009.

[36] J. Ermer, R. Jones, P. Hebert, P. Pien, R. King, D. Bhusari, R. Brandt, O. Al-Taher, C. Fetzer, G. Kinsey *et al.*, "Status of C3MJ+ and C4MJ production concentrator solar cells at spectrolab," *Photovoltaics, IEEE Journal of*, vol. 2, no. 2, pp. 209–213, 2012.

[37] G. S. Kinsey, P. Hebert, K. E. Barbour, D. D. Krut, H. L. Cotal, and R. A. Sherif, "Concentrator multijunction solar cell characteristics under variable intensity and temperature," *Progress in Photovoltaics: Research and Applications*, vol. 16, no. 6, pp. 503–508, 2008.

[38] C. Karcher, H. Helmers, M. Schachtner, F. Dimroth, and A. W. Bett, "Temperature-dependent electroluminescence and voltages of multijunction solar cells," *Progress in Photovoltaics: Research and Applications*, 2013.

[39] K. P. Thompson and J. P. Rolland, "Freeform optical surfaces: a revolution in imaging optical design," *Optics and Photonics News*, vol. 23, no. 6, pp. 30–35, 2012.

[40] J. P. Rolland and K. P. Thompson, "Freeform optics: Evolution? No, revolution!" *SPIE Newsroom*, 2012.

[41] I. Livshits, D. Mouromtsev, and V. Vasiliev, *Modern Information Systems. Ontology Approach in Lens Design.* InTech, 2012, ch. 2, pp. 23–40.

[42] G. W. Forbes and A. E. Jones, "Towards global optimization with adaptive simulated annealing," in *1990 Intl Lens Design Conf.* International Society for Optics and Photonics, 1991, pp. 144–153.

[43] T. G. Kuper and T. I. Harris, "Global optimization for lens design: an emerging technology," in *Optical Systems Design'92.* International Society for Optics and Photonics, 1993, pp. 14–28.

[44] F. Bociort, *Encyclopedia of optical engineering.* CRC press, 2003, vol. 2, ch. Optical System Optimization.

[45] R. J. Koshel, *Illumination Engineering: design with nonimaging optics*. John Wiley & Sons, 2012.

[46] R. Winston, J. C. Miñano, and P. Benitez, *Nonimaging optics*. Academic Press, 2005.

[47] J. Chaves, *Introduction to nonimaging optics*. CRC Press, 2008.

[48] J. C. Miñano and P. Benítez, *Concentrator optics for the next-generation photovoltaics*, ser. Series in Optics and Optoelectronics. Taylor & Francis, 2004, ch. 13, pp. 285–325.

[49] A. Cvetković, "Free-form Optical Systems for Nonimaging Applications," Ph.D. dissertation, Escuela Técnica Superior de Ingenieros de Telecomunicación, Universidad Politécnica de Madrid, 2009.

[50] D. C. Miller, M. D. Kempe, C. E. Kennedy, and S. R. Kurtz, "Analysis of transmitted optical spectrum enabling accelerated testing of cpv designs," in *SPIE Solar Energy+ Technology*. International Society for Optics and Photonics, 2009, pp. 74 070G–74 070G.

[51] D. C. Miller and S. R. Kurtz, "Durability of fresnel lenses: a review specific to the concentrating photovoltaic application," *Solar Energy Materials and Solar Cells*, vol. 95, no. 8, pp. 2037–2068, 2011.

[52] R. Leutz and A. Suzuki, *Nonimaging Fresnel lenses: design and performance of solar concentrators*. Springer, 2001, vol. 83.

[53] T. Levi-Civita, "Complementi al teorema di Malus-Dupin. Nota I," *Rend. Sedute R. Accad. Dei Lincei IX (1)*, pp. 185–189, 1900.

[54] P. Benı, J. C. Min, O. Dross, M. Herna, W. Falicoff *et al.*, "Simultaneous multiple surface optical design method in three dimensions," *Optical Engineering*, vol. 43, no. 7, pp. 1489–1502, 2004.

[55] F. Duerr, P. Benítez, J. C. Miñano, Y. Meuret, and H. Thienpont, "Analytic design method for optimal imaging: coupling three ray sets using two free-form lens profiles," *Optics express*, vol. 20, no. 5, pp. 5576–5585, 2012.

[56] H. Ries and J. A. Muschaweck, "Tailoring freeform lenses for illumination," in *International Symposium on Optical Science and Technology*. International Society for Optics and Photonics, 2001, pp. 43–50.

[57] V. Oliker, "Optical design of freeform two-mirror beam-shaping systems," *JOSA A*, vol. 24, no. 12, pp. 3741–3752, 2007.

[58] S. A. Kochengin and V. I. Oliker, "Determination of reflector surfaces from near-field scattering data II. Numerical solution," *Numerische Mathematik*, vol. 79, no. 4, pp. 553–568, 1998.

[59] D. Michaelis, S. Kudaev, R. Steinkopf, A. Gebhardt, P. Schreiber, and A. Bräuer, "Incoherent beam shaping with freeform mirror," in *Optical Engineering+ Applications*. International Society for Optics and Photonics, 2008, pp. 705 905–705 905.

[60] F. Fournier, "Freeform reflector design with Extended Sources," Ph.D. dissertation, College of Optics and Photonics, University of Central Florida, 2010.

[61] W. B. Elmer, *The optical design of reflectors*, ser. Wiley series in pure and applied optics. Wiley, 1980.

[62] F. R. Fournier, W. J. Cassarly, and J. P. Rolland, "Fast freeform reflector generation using source-target maps," *Optics express*, vol. 18, no. 5, pp. 5295–5304, 2010.

[63] S. A. Kochengin and V. I. Oliker, "On the numerical solution of the problem of reflector design with given far-field scattering data," *Contemporary Mathematics*, vol. 226, pp. 13–32, 1999.

[64] L. Wang, K. Qian, and Y. Luo, "Discontinuous free-form lens design for prescribed irradiance," *Applied optics*, vol. 46, no. 18, pp. 3716–3723, 2007.

[65] P. Benitez and J. C. Minano, "Three-dimensional simultaneous multiple-surface method and free-form illumination-optics designed therefrom," Aug. 24 2006, WO Patent App. PCT/US2004/024,330.

[66] M. Montecchi, "Deeper investigation of Dow Corning 3145 and Bayer Silicones rtv 615 glue," ENEA, Tech. Rep., 2000.

[67] R. Herrero, M. Victoria, C. Domínguez, S. Askins, I. Antón, and G. Sala, "Concentration photovoltaic optical system irradiance distribution measurements and its effect on multi-junction solar cells," *Progress in Photovoltaics: Research and Applications*, vol. 20, no. 4, pp. 423–430, 2012.

[68] D. V. Rosato, D. V. Rosato, and M. G. Rosato, *Injection Molding Handbook*. Kluwer Academic Publishers, 2000.

[69] D. C. Mongomery, *Design and analysis of experiments*. John Wiley & Sons, 2008.

[70] W. C. Sinke, C. Ballif, A. Bett, B. Dimmler, D. Dimova-Malinovska, P. Fath, N. Mason, F. Ferrazza, H. Gabler, M. Hall *et al.*, "A Strategic Research Agenda for Photovoltaic Solar Energy Technology," Working Group 3: Science, Technology and Applications, Tech. Rep., 2011.

[71] P. Benítez, J. C. Miñano, P. Zamora, R. Mohedano, A. Cvetkovic, M. Buljan, J. Chaves, and M. Hernández, "High performance Fresnel-based photovoltaic concentrator," *Optics express*, vol. 18, no. 101, pp. A25–A40, 2010.

[72] J. C. Miñano, P. Benítez, P. Zamora, M. Buljan, R. Mohedano, and A. Santamaría, "Free-form optics for Fresnel-lens-based photovoltaic concentrators," *Optics express*, vol. 21, no. 103, pp. A494–A502, 2013.

[73] S. R. Kurtz, M. Muller, B. Marion, K. Emery, R. McConnell, S. Surendran, and A. Kimber, "Considerations for how to rate CPV," in *CPV 6 conference*, 2011.

[74] "Standard iec 62670-1, Concentrator Photovoltaic (CPV) Performance Testing Part 1," 2013.

[75] "$http://www.spectrolab.com/DataSheets/PV/CPV/C3MJ_PLUS_2011.pdf$," 2011.

[76] J. Maroto and G. Araújo, "Three-dimensional circuit analysis applied to solar cell modelling," in *Proceedings of the 13th European Photovoltaic Solar Energy Conference*, vol. 1246, 1995.

[77] A. Antonini, M. Stefancich, D. Vincenzi, C. Malagu, F. Bizzi, A. Ronzoni, and G. Martinelli, "Contact grid optimization methodology for front contact concentration solar cells," *Solar energy materials and solar cells*, vol. 80, no. 2, pp. 155–166, 2003.

[78] K. Araki and M. Yamaguchi, "Extended distributed model for analysis of non-ideal concentration operation," *Solar energy materials and solar cells*, vol. 75, no. 3, pp. 467–473, 2003.

[79] B. Galiana, C. Algora, I. Rey-Stolle, and I. G. Vara, "A 3-D model for concentrator solar cells based on distributed circuit units," *Electron Devices, IEEE Transactions on*, vol. 52, no. 12, pp. 2552–2558, 2005.

[80] K. Nishioka, T. Takamoto, T. Agui, M. Kaneiwa, Y. Uraoka, and T. Fuyuki, "Evaluation of InGaP/InGaAs/Ge triple-junction solar cell and optimization of solar cell's structure focusing on series resistance for high-efficiency concentrator photovoltaic systems," *Solar Energy Materials and Solar Cells*, vol. 90, no. 9, pp. 1308–1321, 2006.

[81] Y. Martin, P. D. Kirchner, T. van Kessel, B. Wacaser, R. Sandstrom, D. Patel, B. Kim, A. Badahdah, H. Khonkar, R. Leutz *et al.*, "High-concentration photovoltaics. effect of inhomogeneous spectral irradiation," *IEEE Journal of Photovoltaics*, vol. 5, no. 1, pp. 454–460, 2014.

[82] E. Durán, M. Piliougine, M. Sidrach-de Cardona, J. Galán, and J. Andújar, "Different methods to obtain the I–V curve of PV modules: a review," in *Photovoltaic Specialists Conference, 2008. PVSC'08. 33rd IEEE.* IEEE, 2008, pp. 1–6.

[83] M. Guvench, C. Gurcan, K. Durgin, and D. MacDonald, "Solar simulator and iv measurement system for large area solar cell testing," in *Proceedings of the 2004 american society for engineering education annual conference & exposition*, 2004.

[84] F. Recart, H. Mackel, A. Cuevas, and R. Sinton, "Simple data acquisition of the current-voltage and illumination-voltage curves of solar cells," in *Photovoltaic Energy Conversion, Conference Record of the 2006 IEEE 4th World Conference on*, vol. 1. IEEE, 2006, pp. 1215–1218.

[85] G. Segev, G. Mittelman, and A. Kribus, "Equivalent circuit models for triple-junction concentrator solar cells," *Solar Energy Materials and Solar Cells*, vol. 98, pp. 57–65, 2012.

[86] R. King, D. Bhusari, A. Boca, D. Larrabee, X.-Q. Liu, W. Hong, C. Fetzer, D. Law, and N. Karam, "Band gap-voltage offset and energy production in next-generation multijunction solar cells," *Progress in Photovoltaics: Research and Applications*, vol. 19, no. 7, pp. 797–812, 2011.

[87] R. King, D. Law, K. Edmondson, C. Fetzer, R. Sherif, G. Kinsey, D. Krut, H. Cotal, and N. Karam, "Metamorphic and lattice-matched solar cells under concentration," in *Photovoltaic Energy Conversion, Conference Record of the 2006 IEEE 4th World Conference on*, vol. 1. IEEE, 2006, pp. 760–763.

[88] D. C. Giancoli and J. J. Boyle, *Physics: principles with applications*. Pearson Education, 2005.

Acknowledgments

In conclusion of this PhD dissertation, I would spend some words in acknowledging who had a relevant influence during my PhD studies.
First of all I would like to thank the funders of my activities, Polo Fotovoltaico Veneto, Centro Studi e Ricerche E.Fermi of Rome, and the Doctoral School of Industrial Engineering, who provided a 3-year scholarship, funded the laboratory equipments and the participation to conferences.
The activities presented were conducted in collaboration with *AtemEnergia Srl*®, a spin-off of the University of Padua. I'm very grateful to the colleagues of the spin-off Prof. Sandro Centro, Dr. Piergiorgio Antonini and Dott. Stelvio Golfetto, that collaborated with me almost daily during the last years. I'm really happy to have found them on my path because I learnt something useful from each one. I am very grateful to prof. Sandro Centro, my mentor during my route in the CPV world, for the mutual esteem and the confidence that he gave me. I'm also grateful to Piergiorgio, who helped and supported me in many situations since my master thesis. I thank him particularly for the presenting skills that he taught me and for his constant availability. Stelvio has been one of the most influencing person during my last studies: I would thank him for the infinite useful discussions, for the way he spent his efforts, and for the friendship.
I would also thank Prof. Luisa Rossetto, for letting me introduce in the Doctoral School of Industrial Engineering.
All the measures with the Coordinate Measuring Machine would not have been possible without the support of the Department of Physics. I'm particularly grateful to Razvan Dima, Emil Udup, and Alessandro Prevedello for their infinite courtesy and availability. The Department of Physics was also fundamental during the assembling step of the I-V curve tracer, so I would thank Alessandro Griggio and Marino Nicoletto.
All the activities discussed are included into a larger project concerning the development of a CPV system. This project is carried on not only by *AtemEnergia Srl*® but also with the endorsement of industrial partners that operate in the injection molding business. For this reason I'm grateful to the companies Unitek, Unica, and Piazzarosa for the continuous support during the development of TwinFocus® system.
In conclusion I would thank my funder since ever, my family, for always holding me up and for the continuous confidence in my choices.